MULTISCALE MODELING OF BIOMASS THERMOCHEMICAL CONVERSION

A Dissertation

Presented to the Faculty of the Graduate School

of Cornell University

in Partial Fulfillment of the Requirements for the Degree of

Doctor of Philosophy

by

Himanshu Goyal

August 2018

MULTISCALE MODELING OF BIOMASS THERMOCHEMICAL CONVERSION

Himanshu Goyal, Ph.D.

Cornell University 2018

Biomass is a sustainable and renewable energy source with a huge potential to provide different types of gaseous and liquid biofuels as well as other specialty chemicals. Among several existing techniques to convert biomass into biofuels or chemicals, biomass thermochemical conversion is particularly promising for non-food sources of biomass, such as wood, agricultural residue or energy crops. This conversion process results from a strong coupling among several chemical and physical processes over a wide range of spatial and temporal scales, making it difficult to comprehend. The design and scale-up of the reactors for biomass thermochemical conversion, typically fluidized bed reactors, are mostly based on empirical correlations, relying heavily on expensive and lengthy pilot-scale reactor studies. The recent advances made in high performance computing (HPC) and computational fluid dynamics (CFD), show a great potential in using CFD tools for the design and optimization of these conversion reactors. However, at present, the usage of these tools is severely limited.

This work improves the current state-of-the-art modeling and simulation tools for biomass thermochemical conversion by focusing on some of their most limiting aspects. To this end, we focus on the modeling of chemical kinetics and particle-scale processes of biomass thermochemical conversion, and explore the effect of multiphase flow (gas-solid flow) on the particle-scale processes in the

conversion reactor. In the first part of the work, a compact chemical kinetic model is developed for the reactions of the biomass conversion and is shown to be computationally affordable to use with CFD tools. The second contribution includes the modeling of particle-scale processes of biomass conversion under large uncertainties in the model parameters, allowing for a rigorous validation study of the model against detailed experimental measurements. Apart from developing models for different processes of biomass conversion, the influence of multiphase dynamics on the particle-scale processes is also evaluated by performing several three-dimensional detailed CFD simulations of a laboratory-scale conversion reactor. As these detailed CFD simulations would be prohibitively expensive to perform for large-scale reactors, a reduced-order model, in the form of a differential equation, is developed to predict the performance of the reactor. The modeling and simulation tools developed in this work allow probing biomass thermochemical conversion process in great detail.

BIOGRAPHICAL SKETCH

Himanshu Goyal was born and grew up in Sirsa, Haryana, India. After graduating from Maharaja Agrasain School in 2007, he joined Indian Institute of Technology (IIT) Guwahati to pursue Bachelor of Technology (BTech) in Chemical Engineering. During his undergraduate studies at IIT Guwahati, Himanshu got an opportunity to do research with Dr. Dipankar Bandyopadhyay on the stability analysis of liquid bilayers. After graduating from IIT Guwahati in 2011, he joined Reliance Industries Limited's (RIL) Jamnagar Petroleum Refinery as a Process Engineer to see Chemical Engineering in "action". After working at RIL for a year, he moved back to academia and joined the Department of Chemical Engineering at Indian Institute of Science (IISc) Bangalore as a Project Assistant to work with Dr. K. Ganapathy Ayappa. At IISc, he spent a year performing experiments to create supported lipid bilayers for the study of protein diffusion in cell membranes. In 2013, Himanshu moved to USA to pursue Ph.D. at the School of Chemical and Biomolecular Engineering at Cornell University in Ithaca, New York. At Cornell, he joined the research group of Dr. Perrine Pepiot, where during his stay of almost 5 years, he developed several modeling and simulation tools to explore the thermochemical conversion of biomass into biofuels.

ACKNOWLEDGEMENTS

Completing this big endeavor wouldn't have been possible without the help and support of many people. I will start by thanking my advisor Prof. Perrine Pepiot, whose guidance helped me to navigate the long journey of PhD. I am immensely grateful for her constant support and encouragement for not only research but also for my personal growth. I would also like to thank my committee members Prof. Donald Koch and Prof. Peter Diamessis for their invaluable insights into my research.

I would like to especially thanks Prof. Olivier Desjardins with whom I had several long and deep discussions on fluid mechanics and CFD. I am thankful to Prof. Jesse Capecelatro at University of Michigan for a fruitful collaboration. I learned a lot from our collaboration. Sincere thanks to Prof. Elizabeth Fisher for providing her time and expertise in biomass experiments.

I would like to thank my labmates: Lara, Ashish, Pushan, Youwen, Krithika, for making the lab a fun place to work and making all the conferences memorable. I will always remember our discussions on numerous topics over coffee. I would like to thank Prashant for being a constant support and a confidant. I am very thankful to Snehahsih, Akanksha, Adithya, Ritesh, Pooja, Prajwal, Rohit, Sheng, John, Jinglin, Thomas, Charlilie, Chris, Rahul, Anubhab, and many more for making my stay at Cornell more enjoyable. Their company kept my soul warm in the winters of Ithaca.

I would like to thank Prof. Fengqi You for making my experience as a Teaching Assistant for Computational Optimization valuable.

Special thanks to Prof. Dipankar Bandopadhyay at IIT Guwahati who showed me how research can be fun and encouraged me to pursue PhD. His enthusiasm for work has always motivated me.

Finally, I would like to acknowledge the sacrifice and support of my family that helped me to reach where I am today. Special thanks to my wife, Jinna, who provided constant love and support through thick and thin and made my PhD experience more enjoyable. A big thanks to my niece, Mola, a little bundle of joy, who always fills my heart with love.

TABLE OF CONTENTS

LIST OF TABLES

LIST OF FIGURES

CHAPTER 1

INTRODUCTION

1.1 Motivation and background

Society's growing energy needs and the imminent dangers of global warming caused by the excessive usage of fossil fuels demand development and deployment of renewable and sustainable sources of energy. Several renewable energy sources are currently being utilized, such as biomass, wind, solar, geothermal, and hydropower. Among all the renewable energy sources, only biomass can provide a liquid fuel, and therefore can help in reducing the dependence of transportation sector on crude oil, which provides more than 97% of the transportation fuel [157]. Biomass is a term for all organic matter derived from plants, such as wood, crops, and agricultural waste, and any fuel derived from biomass is known as biofuel [48]. It is a general consensus that biomass will play a major role in the deployment of renewable energies in the near future [159]. In 2013, biomass provided approximately 10 percent of the global energy supply [174]. The widespread availability of biomass has the potential to supply much larger amounts of useful energy with fewer environmental impacts than fossil fuels [103]. Recognizing the potential of biomass as a renewable energy source, many countries and regions have set aggressive goals for near-term deployment of biofuels. In 2013, biofuel blend mandates were identified at the national level in 27 countries, and regulatory policies promoting the use of biofuels existed in more than 49 countries [154].

Past developments in producing fuels from biomass have primarily focused on first-generation biofuels, i.e., fuels that are derived from food crops based

feedstock, such as corn, sugarcane, soybean, and rapeseed. At present, ethanol is the largest biofuel produced in the world, with the US and Brazil alone contributing 58% and 26%, respectively to the global production of biomass derived ethanol [7]. Corn is the primary feedstock for ethanol production in the US, while sugarcane is in Brazil, and the conversion of corn and sugarcane into ethanol is mainly achieved by fermentation. Biodiesel is another major biofuel and is derived from oils, such as rapeseed and soybean oils, using transesterification. The fact that both ethanol and biodiesel utilize food crops as feedstock has raised concerns about the supply and prices of these food crops.

The concerns about the food-based first-generation biofuels have led to significant research efforts in developing fuels from non-food sources of biomass, known as second-generation biofuels. In this regard, lignocellulosic biomass, which is made up of three primary biomolecules: cellulose, hemicellulose, and lignin, with small amounts of several other compounds, is seen as a potential feedstock. Examples of lignocellulosic biomass include agricultural byproducts (e.g., corn stover, sugarcane bagasse, and straw), forestry residue, and energy crops, such as switch grass. A number of conversion pathways, such as biochemical and thermochemical, are under development to convert lignocellulosic biomass into biofuels or chemicals, or directly produce energy from it. Biochemical conversion involves use of enzymes, bacteria or other microorganisms to convert biomass into liquid fuels. This conversion route, however, does not utilize the lignin fraction of biomass. Thermochemical conversion techniques, on the other hand, can utilize lignin along with the other components of lignocellulosic biomass in the conversion process. In thermochemical conversion, heat and catalysts are used to convert biomass into an intermediate gas or liquid, followed by an additional conversion step to upgrade that intermediate

into a biofuel, such as transportation fuel, or other chemicals. This conversion technique is described in more detail in the following section.

1.2 Biomass thermochemical conversion

Biofuels derived from thermochemical conversion of biomass show great promise for being economically competitive with conventional petroleum derived gasoline and diesel [40, 183, 55]. Moreover, the ability of thermochemical conversion techniques to process a wide variety of feedstocks and provide various types of fuels show a great potential to contribute to the development of second generation biofuels [138].

Two major classes of biomass thermochemical conversion techniques can be identified: fast pyrolysis and gasification. Fast pyrolysis is the rapid heating $O(10^3$ K/s) of biomass in the absence of oxygen at relatively low temperatures (773–873 K), maximizing the yield of a highly oxygenated liquid product, which requires significant upgrading before it can be used as a transportation fuel [142]. On the other hand, gasification is the heating of biomass at higher temperatures (>1073 K), in the presence of limited oxygen, maximizing the yield of gaseous products, such as CO, H_2, and CO_2, known as synthetic gas, and producing small amounts of char, ash, and tar (a mixture of condensible hydrocarbons). Synthetic gas, produced during biomass gasification, can be used as a building block to produce numerous types of chemicals and fuels via well established Fischer-Tropsch process. For both fast pyrolysis and gasification of biomass, bubbling fluidized bed (BFB) and circulating fluidized bed (CFB) reactors are commonly used, as these reactors provide high heat and mass transfer

rates, ensure homogeneity in the bed, and are capable of being scaled up to large scales.

1.2.1 Major challenges

Considerable progress has been made in biomass thermochemical conversion at various fronts. For instance, several experimental studies have identified the factors that maximize the yield of liquid product during fast pyrolysis of biomass. Still, a comprehensive understanding of both pyrolysis and gasification of biomass is far from the reality, and several technical challenges, related to the reliability, cost, and efficiency of the conversion process, need to be addressed to achieve the widespread industrial deployment of these conversion techniques [48, 113, 142].

At present, a major challenge in biomass thermochemical conversion techniques is obtaining a product with consistent properties from the conversion reactors. The yield, composition, and properties of the pyrolysis and gasification products are highly dependent on biomass feedstock and the operating conditions of the reactor, such as temperature, pressure, and heating rate [48], making it extremely difficult to control the composition of the product from the conversion reactor. The lack of the ability to control the performance of these reactors is a big hindrance to their industrial applications. For instance, hydrogen (H_2) to carbon monoxide (CO) ratio in the product gas of a biomass gasifier is a critical parameter for the subsequent liquid fuel synthesis, still variations of nearly an order of magnitude are observed in its reported values for several biomass gasifiers [51, 77, 78, 56, 181, 105] as shown in Fig. 1.1.

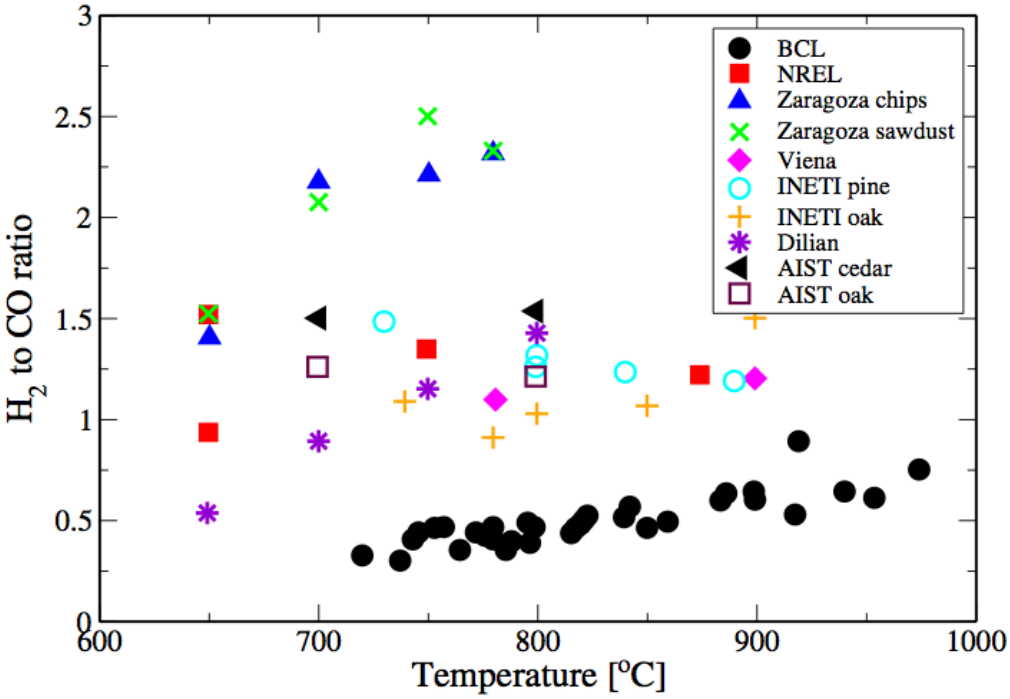

Figure 1.1: Reported hydrogen to carbon monoxide ratios from existing fluidized bed gasifiers reproduced from [138].

For gasification, one of the biggest problems is the undesirable production of tar, a complex mixture of condensable hydrocarbons, during the conversion process [170, 143, 67]. Different tar species exhibit different properties, for example, heterocyclic compounds (e.g., phenol) exhibit high water solubility, whereas polycyclic aromatic hydrocarbons (PAH) can condense at relatively high temperatures. On the basis of its composition, tar can produce hazardous tar–water mixtures or condense in downstream equipment, causing fouling or plugging as shown in Fig. 1.2, and therefore it needs to be removed. At present, tar reduction is mainly achieved by using catalysts in the reactor itself [170] or in the downstream equipments [143]. Removal of tar is associated with high maintenance cost and reduction in the operating time of the reactor, leading to an increase in the operating costs [198]. At present, a fundamental understanding of tar

formation is still lacking, and therefore it remains difficult to develop efficient strategies to eliminate or minimize tar production during biomass gasification.

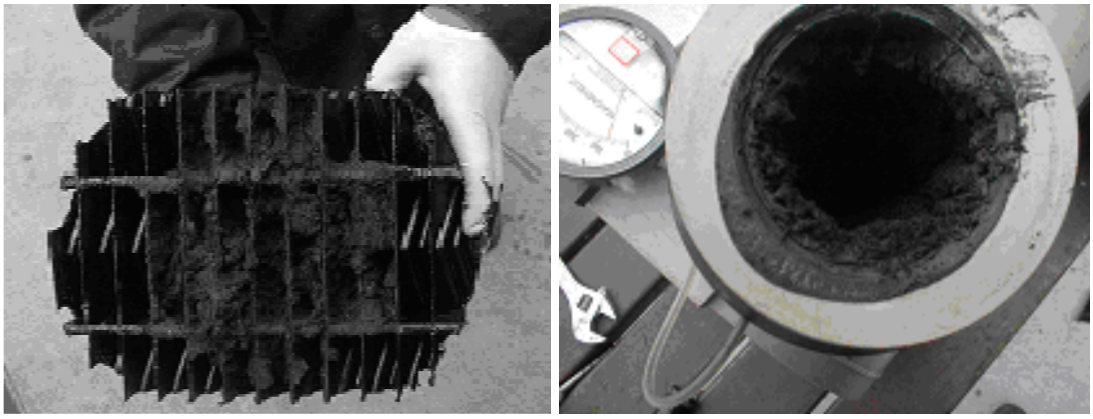

Figure 1.2: Fouling of equipment and plugging of piping from tar [198].

Dealing with the technical challenges, as described above, associated with biomass thermochemical conversion in fluidized bed reactors (FBR) requires the various underlying physical and chemical processes to be fully understood and characterized, however, their current understanding is limited. For this reason, design and scale-up of these reactors are mostly based on empirical correlations, relying heavily on expensive and lengthy pilot scale reactor studies. However, these experimental studies of the reactors often fail to provide the local and detailed information, such as the instantaneous concentration of a chemical species, due to the highly unsteady and opaque solid phase, and the harsh operating conditions, such as high temperature, inside these reactors [21].

Experimental studies can be complement by detailed modeling and simulation tools and supplement our current understanding of biomass conversion in FBRs. For example, modeling and simulation tools can not only predict the flow behavior inside the reactors, but also provide the local and detailed infor-

mation, which can be difficult to obtain from the experiments. In recent years, computational fluid dynamics (CFD) has emerged as a promising tool in several areas, such as turbulent combustion and multiphase flows. The recent advances in CFD techniques and high performance computing (HPC) provide a great opportunity to develop predictive simulation tools to explore and understand biomass thermochemical conversion in FBRs. These tools can remove the dependence on empirical design strategies and help in the optimization and the scale-up of the conversion reactors [48]. The following section describes the current status of modeling and simulation tools for biomass thermochemical conversion and the associated challenges.

1.3 Modeling of biomass thermochemical conversion

Biomass thermochemical conversion in FBRs results from a strong interaction among several chemical and physical processes over a wide range of spatial and temporal scales. In these reactors, thermochemical conversion process starts with the injection of biomass particles into a high temperature bed of thermally inert material, such as sand, where biomass is rapidly heated and releases its moisture content at around 373 K. In the temperature range of 473–873 K, devolatilization of biomass takes place, in which biomass gets converted into permanent gases, condensible volatiles (primary tar), and residual solid (char). Primary tar, produced during biomass devolatilization, undergoes further pyrolytic reactions both inside the biomass particle and in the gas phase. The yield and composition of the permanent gases, tar, and solid char strongly depend on the coupling among the chemistry, biomass intra-particle processes, mesoscale structures of the multiphase flow, such as bubbles and clusters, and the reac-

tor scale processes. Therefore, predictive simulation tools for biomass thermochemical conversion require accurate models for all these underlying processes, integrated into a unified framework [128]. However, a lack of understanding of the processes happening at different scales and the computational cost of resolving the smallest scales, such as those associated with chemistry, in reactor simulations have hindered the development of detailed simulation tools. The following subsections describe in detail the challenges associated with different scales of biomass thermochemical conversion.

1.3.1 Molecular scale

From the chemical point of view, biomass is a mixture of several biopolymers: cellulose, hemicellulose, lignin and extractives, whose composition varies widely with feedstock. Ash (inorganic matter) is also a part of biomass, with a content ranging from less than 1% in wood to 25% in some agricultural residues. Metals, such as potassium, calcium, sodium, phosphorus and magnesium, are the main ash constituents [48]. Modeling of biomass thermochemical conversion at the molecular scale requires the mathematical description of the chemical reactions responsible for the conversion of biomass constituents into various product species. Although modeling of the chemical kinetics of this conversion process has come a long way, starting with the usage of a single global reaction [161] to a recently developed model for cellulose pyrolysis using quantum calculations [178, 197], a comprehensive understanding of the thermochemical reactions is still lacking. Several processes of biomass thermochemical conversion requires the knowledge of accurate chemistry, such as devolatilization of biomass, secondary gas-phase reactions of primary tar, heterogenous reactions

of char with steam/air, and catalytic reactions of primary tar upgrading. These processes involve a large number of chemical species and reactions, making the accurate knowledge of those species and reactions extremely difficult to obtain if not impossible [38]. This is further exacerbated by the fact that biomass composition varies widely depending on the feedstock [48]. These difficulties have hindered the development of detailed kinetic models for biomass thermochemical conversion chemistry. In their review paper, Gomez-Barea et al. [67] recognize a strong need for modeling efforts in biomass devolatilization and tar chemistry.

The kinetic model developed by the CRECK modeling group for biomass devolatilization reactions [152, 151, 153] is one of the most detailed kinetic model available in the literature [3]. This kinetic scheme represents biomass devolatilization chemistry through 29 reactions and involves 14 solid species and 20 gaseous products. The initial composition of biomass is represented by a few reference compounds, such as cellulose and lignin. The CRECK modeling group has been updating the reaction rate parameters for this kinetic model for more than a decade by fitting the model predictions to a wide and growing range of experimental measurements. Though this kinetic model provides satisfactory predictions for different experimental conditions, a detailed description of the devolatilization chemistry is still lacking.

A detailed description of the gas-phase reactions of tar formation and destruction is not available, and therefore the mechanisms developed in the combustion literature for combustion and pyrolysis of various hydrocarbon species have been employed for this purpose [38, 123]. These detailed mechanisms consist of a large number of chemical species $\sim O(10^3)$ and reactions $\sim O(10^4)$. Includ-

ing a single chemical species in a CFD simulation requires a separate partial differential equation (PDE) to be solved for its conservation. Therefore, detailed mechanisms with a large number of chemical species are computationally unaffordable to use in CFD simulations and are limited to zero-dimensional configurations neglecting the transport processes. In the absence of a computationally affordable chemical mechanism, most of the existing CFD studies of biomass thermochemical conversion either neglect the gas-phase reactions [22, 19, 87] or use very simple kinetic models [111, 53, 185, 188, 193, 191, 107, 125, 126, 130, 131, 86]. These kinetic models describe biomass devolatilization and evolution of gas-phase primary tar using a few model compounds and global reactions, whose rates are fitted using available experimental data. While these global models can be fitted *a priori* to provide trends in terms of the major controlling parameters, such as reactor operating temperature, they are not appropriate whenever more quantitative or detailed information is sought from CFD calculations. An intermediate level of kinetic model is required, which balances between the chemical detail and the associated computational cost in CFD simulations.

1.3.2 Particle scale

Biomass is a porous material with a highly anisotropic internal structure due to its fibrous nature, with the thermal conductivity in the longitudinal direction (parallel to the fibers) about 2-3 times greater than the conductivity in the transverse direction (perpendicular to the fibers) [61]. Particle scale models for biomass thermochemical conversion mathematically represent the chemical kinetics of the conversion process coupled with various intra-particle trans-

port processes that accompany the conversion process, such as the transport of gaseous species through the pores of a biomass particle. However, most of the particle scale models either neglect all the intra-particle processes or assume a one-dimensional representation of the particle [133, 33, 3, 4], though very recently, a three-dimensional model has been developed [61].

Several challenges hinder the development of accurate particle scale models for biomass devolatilization, a major one being the poor knowledge of the complex microscale morphological changes, such as shrinkage and changing internal particle structure, that take place inside a biomass particle during the devolatilization process [88]. These morphological changes significantly affect biomass properties, such as thermal conductivity and heat capacity. Detailed particle level modeling of biomass devolatilization, therefore, requires models that can accurately capture the dependence of the biomass properties on the internal morphological changes [109]. However, such models do not yet exist because of the inherent complexity of the problem [189].

Due to the reasons described above, the validation of these particle scale models remain elusive. The scarcity of detailed data for biomass properties, such as thermal conductivity and heat capacity, has prompted the usage of widely varying values for these properties in the literature [182]. Many times the biomass properties are tuned in an *ad-hoc* manner during the validation process [33]. This problem has been recognized in the literature; in the list of "top ten" challenges of biomass pyrolysis by Mettler et al. [109], the validation of biomass pyrolysis models has been identified as one of the fundamental challenge. For a rigorous validation of the particle scale models, the effect of the uncertainties in the values of biomass properties needs to be quantified on the

model predictions for a meaningful comparison between the model predictions and the experimental measurements, and to identify the potential areas for further improvements in the model.

1.3.3 Reactor scale

As mentioned earlier, bubbling fluidized beds (BFB) and circulating fluidized beds (CFB) are the two major reactor types used for biomass thermochemical conversion. In these reactors, gas-solid flow is strongly coupled with chemical reactions and particle scale processes, such that the smallest scales can affect the overall reactor performance. In BFB, bubble dynamics and bypassing of gas can significantly impact the conversion of biomass into primary products and the subsequent homogeneous and heterogeneous reactions. Though these phenomena are well-known in the literature, their fundamental understanding is still limited [9]. In the case of CFB risers, the high gas flow rates cause the flow to become unsteady with large fluctuations in particle concentration. Local regions of densely packed particles, referred to as clusters, develop in the flow and fall near the walls of the reactor, while dilute suspensions of particles rise in the central region [124]. Clusters have been observed to reduce mixing and interaction of particles with the gas [160, 27], potentially lowering operating efficiencies significantly. Meanwhile, detailed studies demonstrating the quantitative impact of particle clustering on chemical processes occurring in such flows remain elusive. Deen et al. [39] and Van der Hoef et al. [175] have reviewed the different modeling strategies used for gas-solid flows in fluidized beds. Among them, Two-Fluid Model (TFM) and Discrete Element Model (DEM) are most commonly used in the biomass thermochemical conversion literature.

TFM, an Euler-Euler approach, represents both the gas and solid phases as inter-penetrating continua on a common Eulerian grid, greatly reducing the computational cost, as individual particles do not need to be tracked. However, TFM requires complex closure relations for the interfacial processes, such as drag, heat and mass transfer, granular stresses, and surface and bulk reaction rates. These closures are evaluated using the kinetic theory of granular flow (KTGF) or empirical correlations [9, 128]. Within the last 15 years, the application of TFM to biomass pyrolysis and gasification has primarily focused on modeling dense two-dimensional BFB reactors [90, 62, 193, 191, 192, 186, 196, 136, 15]. Only recently, Lee et al. [93] performed TFM simulations of biomass pyrolysis in a three-dimensional configuration to investigate the effect of bed geometry on biomass pyrolysis.

DEM is an Euler-Lagrange strategy, where individual particles are tracked using Newton's laws of motion but the boundaries of individual particles are not resolved, and therefore models are required for interphase drag, and heat and mass transfer. However, particle collisions are explicitly treated using hard-sphere [24] or soft-sphere collision models [35]. Particle residence time, temperature, composition, and other useful particle scale properties can be calculated, which makes it possible to study their effect on the overall process. Compared to TFM, a more accurate description of heat, mass, and momentum exchange between continuum and dispersed phases can be incorporated [125]. Though computationally expensive, DEM can provide insight into the detailed physics of reactive gas-solid flows and can help in developing better closures for larger scale simulations [22]. Due to the added computational expense of tracking individual particles, most DEM studies to date consider two-dimensional flows in small geometries with a relatively small number of

particles [54, 129, 125, 149, 69], and only recently, DEM coupled with a kinetic model has been used in three dimensions [20, 100, 27]. For example, Capecelatro et al. [27] performed three-dimensional DEM simulations of catalytic particles in a periodic pipe flow and showed that the presence of clusters delayed the conversion process by up to 85% compared to a corresponding homogeneous flow. However, those simulations did not account for spatial variations in the vertical direction that are known to have a large effect on biomass fast pyrolysis [173].

A comparison of both TFM and DEM approaches show that TFM has the advantage of being computationally less demanding and thus can be used to solve reactors with a large number of particles, however, it is limited in terms of the detailed particle scale information. For instance, Desjardin et al. [42] showed that TFM is unable to correctly capture particle trajectory crossing and particle segregation is artificially over predicted for dilute flows. On the other hand, DEM offers a much more accurate description of the particle motion, chemical reactions, and heat and mass transfer between the particles and the gas phase [125]. The advantage of particle scale detail in DEM comes at the cost of additional computational expense. Therefore, DEM is more appropriate for detailed simulations of small size reactors, while TFM can be used to simulate larger reactors.

Simulations of biomass thermochemical conversion in FBRs, using TFM or DEM approach, require the inclusion of chemistry and particle scale models into a CFD code. This introduces several additional partial differential equations (PDEs), for chemical kinetics and particle scale model, into a CFD code and brings large disparity in the length and time scales. The small scales introduced because of the reactive nature of the gas-solid flow restrict the time-step and grid

sizes compared to a purely hydrodynamic problem, and make the simulations prohibitively expensive. Therefore, most of the detailed CFD studies of biomass thermochemical conversion in FBRs have been limited to small lab scale reactors with global kinetic schemes involving only a few species and reactions [9, 138]. In fact, one of the most detailed 3D simulation for biomass pyrolysis in the literature has been performed for a lab scale reactor with a diameter of 3.8 cm and height of 46 cm using DEM, neglecting the gas-phase reactions and representing biomass devolatilization using a homogenous particle model (neglecting intra-particle processes) with a few global reactions. The simulation was performed on the UK national supercomputer HECToR Phase 2a, and required 80,000 CPU hours for 5 s real time of pure sand fluidization and 320,000 CPU hours for 5 s real time of biomass pyrolysis [20].

1.3.4 Industrial scale

At the industrial scale, the conversion reactor with ~O(10 m) size will be connected to several other process equipments, consequently performing detailed CFD simulations at those scales is a fantastic task. Still, chemical industries need modeling tools to predict the outcome of several interconnected process equipments at various operating conditions. For this purpose, instead of detailed simulations, various engineering models based on a simplified description of the main processes are used. For instance, models based on equilibrium relations [97], combinations of ideal reactors, such as continuous stirred tank reactors (CSTR) and plug flow reactors (PFR) [166], and two-phase theory of fluidization [155] as well as commercial process simulation softwares, such as Aspen Plus [145] are commonly utilized in research community [97, 166, 155].

The engineering models are an integral part of chemical industries, however, they are highly simplified and may not be valid outside the narrow range of experimental conditions used for their validation [138]. In this regard, the knowledge gained from detailed CFD simulations of small scale reactors can be used to build computationally inexpensive models for the industrial scale systems. However, it remains a challenge as the nature of flow, such as turbulence, in an industrial reactor can be very different from that of a small scale reactor, and thus can have a significantly different performance. One way to approach this problem is to perform the detailed simulations of a small portion of the industrial reactor focusing on a specific physical and chemical phenomenon [85, 76].

1.4 Contributions

The aforementioned modeling challenges make the development of accurate modeling and simulations tools for biomass thermochemical conversion very difficult. A lot of work is required, not only to build accurate models at different scales but also to combine them to develop a computational framework for the optimization and scale-up of the reactors. The work presented in this dissertation aims at addressing some of these challenges. The approach used here is to proceed hierarchically from small scales involving only a few processes to large scales with multiple processes. The main contributions of this work are described below:

- A major modeling challenge identified in the literature is the absence of a computationally affordable kinetic model that can be used to study the formation of different tar species during biomass gasification. As a re-

sult, only global kinetic models have been used in CFD studies. To address this problem, a compact kinetic model is developed starting from a detailed kinetic model for the secondary gas-phase reactions involving formation and destruction of tar at gasification conditions (1073–1273 K), and validated against several experimental measurements. The developed compact kinetic model is a significant step towards improving the ability of current state-of-the-art CFD tools to study tar formation in FBRs. To show the affordability of the compact kinetic model in CFD simulations, it is integrated with our in-house CFD code NGA [41] and used to simulate biomass fast pyrolysis in a lab scale droptube reactor and a BFB. The compact kinetic model now makes it possible to study the impact of bed hydrodynamics and other operating parameters, such as temperature and reactor geometry, on the formation and consumption of different classes of tar in a computationally affordable manner.

- A second modeling problem identified in the literature is the usage of widely varying values of biomass properties in particle scale models of biomass pyrolysis, and as a result, a quantitative comparison of the model predictions with experiments becomes difficult. For this purpose, a one-dimensional particle scale biomass pyrolysis model is developed and the uncertainty in the model parameters of transport processes is propagated through the model predictions. This allows a rigorous analysis of the model validity by comparing the model predictions including uncertainty with detailed experiments. This work identifies some of the experimental measurements that can be a focus area for further developments in the chemical kinetics of biomass devolatilization.
- The strong coupling between the multiphase flow and the particle scale

processes is well-known in the literature, though only a few studies have explored this problem using detailed CFD simulations. In this dissertation, for the first time, three-dimensional CFD-DEM simulations of catalytic upgrading of biomass pyrolysis vapors in a CFB riser are performed to quantitatively evaluate the impact of the particle clustering on the catalytic conversion process. Moreover, a reduced-order model in the form of a one-dimensional scalar transport equation is also developed to predict the performance of the reactor in a computationally inexpensive manner. This work shows that particle clustering can significantly reduce the catalytic conversion rate of biomass pyrolysis vapors.

1.5 Outline

This dissertation is organized into five chapters. Chapter 2–4 are the manuscripts that have been published or are in preparation for submission to the leading journals in biomass thermochemical conversion field. A brief description of the various chapters is as follows:

- Chapter 2 [70] describes the development of a computationally affordable compact chemical kinetic model for the secondary gas-phase reactions at biomass gasification conditions. The developed kinetic model is integrated with a CFD code to simulate two lab scale reactors.
- In Chapter 3, the uncertainty in the parameters of a particle scale biomass pyrolysis model is quantified and propagated through the model predictions, which are compared against several detailed experimental measurements, providing a rigorous validation process for the particle scale

model.

- In Chapter 4 [68], three-dimensional CFD-DEM simulations of a CFB riser are performed to quantitatively evaluate the impact of bed hydrodynamics on the catalytic conversion of biomass pyrolysis vapors. A reduced-order model is also developed in the form of one-dimensional differential equation to predict the reactor performance.
- Chapter 5 provides major conclusions from this dissertation.

Relevant background information and existing literature are included in the beginning of each chapter.

CHAPTER 2

A COMPACT KINETIC MODEL FOR BIOMASS PYROLYSIS AT GASIFICATION CONDITIONS

2.1 Abstract

Computational Fluid Dynamics (CFD) tools are increasingly gaining importance to obtain detailed insight into biomass gasification. A major shortcoming of the current CFD tools to study biomass gasification is the lack of computationally affordable chemical kinetic models, which allows detailed predictions of the yield and composition of various gas and tar species in complex reactor configurations. In this work, a detailed mechanism is assembled from the literature and reduced to a compact model describing the gas phase reactions of biomass gasification in the absence of oxygen. The reduction procedure uses a graph-based method for unimportant kinetic pathways elimination and quasi-steady-state species selection. The resulting reduced model contains 39 gas species and 118 reactions, and is validated against the detailed model and two experimental configurations: the pyrolysis of volatile species, such as levoglucosan (LVG), in a tubular reactor, and the fast pyrolysis of biomass particles in a droptube reactor. The reduced model predicts the evolution of major gas products (e.g. CO, CO2, CH4, H2) and various classes of tar (e.g. single-ring aromatics, oxygenated aromatics, PAHs) produced during biomass gasification. The

capability of the reduced model to adequately capture the chemical process in a complex reactor geometry at an acceptable computational cost is demonstrated by employing it in a simulation of a pseudo two-dimensional laboratory-scale fluidized bed reactor (FBR).

2.2 Introduction

Biomass (e.g. wood, energy crops, agricultural residue, municipal waste etc.) is recognized as an essential renewable source of energy that can help in reducing the current dependence on fossil fuels. Thermochemical conversion in fluidized bed reactors (FBR) is a promising technology to convert low-value lignocellulosic biomass into high energy density gaseous or liquid fuel. This process utilizes heat and/or physical catalysts to convert biomass to an intermediate gas or liquid, followed by an additional conversion step to transform that gas or liquid into a biofuel. It has the ability to robustly handle a wide range of feedstock and to produce both liquid and gaseous fuels.

Thermochemical conversion of biomass can be divided into two major classes: pyrolysis and gasification. Pyrolysis is performed at relatively low temperatures (773 K - 873 K) maximizing the yield of liquid fuel, whereas gasification is performed at higher temperatures (1073 K - 1273 K) maximizing the yield of gaseous fuel. In this work, we focus on the latter, namely biomass gasification. One of the major challenges in making biomass gasification an economically viable technology is the reduction or elimination of tars, which are complex mixtures of condensable hydrocarbons [127, 176]. Different tar species exhibit different properties, for example, heterocyclic compounds (e.g. phenol)

exhibit high water solubility, whereas polycyclic aromatic compounds (PAH) can condense at relatively high temperatures [176]. Based on its composition, tar can condense in downstream equipment causing fouling or plugging, and can also produce hazardous tar-water mixtures [176], and therefore needs to be removed. At present, design and scale-up of FBR for biomass gasification are mostly empirically-based, relying heavily on expensive and lengthy pilot-scale reactor studies. Yet, measurements in these reactors are unlikely to be detailed enough to improve our understanding of tar formation processes for various operating conditions and feedstocks, necessary to efficiently optimize the conversion process [175]. Mathematical modeling and simulation tools provide a much more flexible and affordable framework to investigate the controlling chemical and physical processes, with the potential to play a determining role in the development and deployment of the technology.

While the field has seen recent major advances, further improvements are still required, especially in the description of chemical processes, before numerical tools can be utilized to their full potential. Gomez-Barea et al. [67], in their review paper, recognize a strong need for modeling efforts in biomass devolatilization and tar chemistry. But the chemistry of this conversion process is extremely complicated to model due to the high variability of the feedstock, the complex structure of biomass particles, as well as the interaction between chemistry and the multi-phase flow dynamics typically found in gasification reactors [38]. These difficulties have hindered the development of detailed kinetic models for biomass thermochemical conversion chemistry, and have entailed the use of detailed mechanisms for combustion and pyrolysis of various hydrocarbon species, developed in the combustion literature, to represent biomass gasification. For instance, Debiagi et al. [38] and Norinaga

et al. [123] have developed detailed kinetic models for thermochemical conversion of biomass starting from the kinetic models for various hydrocarbons available in the combustion literature. However, the resulting detailed mechanisms consist of a large number of elementary and non-elementary reactions ($O(10^4)$) and chemical species ($O(10^3)$), making them computationally unaffordable to use in CFD simulations. These detailed mechanisms are thus more suitable for zero-dimensional configurations neglecting the transport processes. In the absence of a computationally affordable chemical mechanism, most of the existing modeling studies of biomass thermochemical conversion either neglect the gas phase reactions [22, 19, 87] or use very simple kinetic models [111, 53, 185, 188, 193, 191, 107, 125, 126, 130, 131, 86]. These kinetic models describe biomass devolatilization and evolution of gas-phase primary products using a few model compounds and global reactions, whose rates are fitted using available experimental data, such as Thermo Gravimetric Analysis (TGA). While these global models can be fitted *a priori* to provide trends in terms of the major controlling parameters, such as reactor operating temperature, they are not appropriate whenever more quantitative or detailed information is sought from CFD calculations. For instance, these models can not be used to understand how tertiary tars are created in highly unsteady multiphase flows. An intermediate level of chemical detail is then desirable that can provide refined predictions in simulations, while remaining computationally affordable. The goal of this paper is to develop such a model for biomass gasification. Note that we will focus on the initial volatile release and subsequent gas phase evolution in the absence of oxygen, the resulting model requiring to be complemented by a kinetic model to fully describe the long-term heterogeneous reactions of gasification.

Several automated kinetic reduction techniques have been developed in the combustion community. In general, these reduction techniques analyze a detailed mechanism for a given set of conditions to predict the redundant species and reactions and remove them from the chemical mechanism. Recently, Løvås et al. [101] used a combined reaction flow and sensitivity analysis to develop a compact mechanism for gas phase reactions of biomass combustion. This mechanism was developed in a homogenous reactor configuration for a fixed inlet gas composition and variable temperature.

In this work, we focus on the secondary gas-phase reactions occurring at gasification conditions, and compile a detailed mechanism from the literature describing those reactions. We then use the DRGEP (Direct Relation Graph with Error Propagation) technique [141] to extract a reduced model from the detailed one. The reduction procedure accounts for the variability in the primary products expected to be found in gasification reactors by using a statistical Partially Stirred Reactor (PaSR) configuration. Coupled with an appropriate biomass devolatilization model (here, the work of Corbetta et al. [33], as described below), the resulting reduced model describes the secondary gas phase reactions of biomass devolatilization products in a pure nitrogen environment at temperatures relevant for gasification (1073 K-1273 K). Note that partial oxidation or steam reforming are not included in this study.

The remainder of this paper is organized as follows: Section 2.3 describes how the reference chemical kinetic model for the gas phase chemistry and biomass devolatilization chemistry are assembled from the literature. In Section 2.4, the automatic reduction procedure used to generate a compact model that accurately reproduces the dynamics of the detailed model is presented. Val-

idation is detailed in Section 2.5. Finally, in Section 2.6, the applicability of the reduced model in complex CFD configurations is demonstrated by simulating a pseudo two-dimensional laboratory-scale FBR.

2.3 Reference detailed chemical kinetic model

A description of the reference detailed chemical models for the solid biomass devolatilization and the subsequent secondary gas-phase reactions of the primary devolatilization products is first provided.

2.3.1 Biomass devolatilization model

The high variability of feedstock and the structural complexity of biomass particles prevent the development of detailed kinetic models for describing the transition of the solid biomass into gas and char during devolatilization. In the absence of a more detailed description of the biomass devolatilization, the lumped chemical model developed by the CRECK modeling group [33] is used here to describe the first step of biomass gasification, i.e., devolatilization. This model consists of 24 reactions involving 12 solid species, 7 trapped gases slowly releasing from the solid matrix, and 20 gas phase products. The initial composition of biomass is represented by a combination of cellulose, hemicellulose, and 3 types of lignin. The rates of the lumped reactions are fitted to match a series of thermogravimetric weight loss experiments. It is worth noting that these reactions are irreversible, implying that the gas composition surrounding the particle does not affect the chemistry going on at the particle level. This model has

been validated against a series of experiments for various operating conditions and feedstock [152, 23, 33].

2.3.2 Primary product decomposition and tar formation

The biomass devolatilization model creates a variety of gas phase species, called primary products, whose evolution in the gas phase at gasification temperature must be modeled. These molecules usually are high molecular weight heterogeneous species, such as levoglucosan or phenolic compounds. Some of these molecules, often found in combustion systems (e.g. phenol), have been extensively studied, and accurate mechanisms for their decomposition to small hydrocarbons are available. Recently, we have developed and extensively validated a kinetic model for hydrocarbon pyrolysis and oxidation for combustion applications, the latest version containing a large selection of alkanes up to dodecane and aromatic species, such as phenol, toluene, benzene, xylene, two-ringed aromatics (e.g. α-methylnaphthalene) [12, 116, 118, 119, 120, 117]. In the combustion process, ethylene is placed at the center of molecular growth and we assume that the same holds true for the tars growth in biomass pyrolysis and gasification. To assemble the detailed model, we combine several chemical modules independent from one another, namely, a biomass devolatilization model to form primary products from solid biomass, a primary product decomposition model, and a detailed scheme for polycyclic aromatic hydrocarbon formation. A few of the primary gas phase species produced by devolatilizing biomass are quite specific to the biomass constitutive components, and have not received the same amount of characterization as typical combustion molecules. To describe their decomposition, the lumped chemical reac-

tions available from Calonaci et al. [23] are used. To describe their decomposition, the lumped chemical reactions available from Calonaci *et al* [23] are used. They include levoglucosan, 5-hydroxymethyl furfural, hydroxyacetaldehyde, xylose, coumaryl, and their direct decomposition products. In the pyrolysis conditions of relevance here, the uni-molecular decomposition reactions of those compounds are controlling their overall decomposition rates, as they are responsible for creating the initial radical pool. The chemical mechanism on which those reactions are added being different from the one they have been developed for, especially in terms of the small radicals chemistry, we found that it was necessary to adjust slightly the uni-molecular decomposition rates for levoglucosan, 5-hydroxymethyl furfural, and hydroxyacetaldehyde to properly capture the rates experimentally measured by Shin et al. [163]. In those cases, the rates proposed by Shin et al. [163] were in general adopted, staying as close to the branching ratios of Calonaci et al. [23] as possible whenever competing reactions were involved. One exception is for hydroxyacetaldehyde, for which Calonaci et al. and Shin et al. [163] decomposition pathways were combined and manually adjusted to reflect the added pathways.

The detailed model consists of 396 molecular species and 3210 elementary reaction steps, and is validated against the experiments by Shin et al. [163] in Fig. 2.1, and Norinaga et al. [123] in Fig. 2.2. Shin et al. [163] studied the pyrolysis of levoglucosan (LVG), 5-hydroxymethyl furfural (HMF), and hydroxyacetaldehyde (HAA) in a flow tube reactor for temperatures ranging from 773 K to 1023 K. Norinaga et al. [123] studied the secondary pyrolysis of nascent volatiles generated from the fast pyrolysis of cellulose in a tubular reactor in the temperature range of 973 K to 1073 K. Assuming that there is no significant axial mixing in the tubular reactors of both experiments, these reactors are modeled

as zero-dimensional isobar homogeneous systems. As can be seen from Figs. 2.1 and 2.2, simulation results show very good agreement with the experiments, especially considering the high uncertainty on initial conditions that sometimes exist in the pyrolysis experiments.

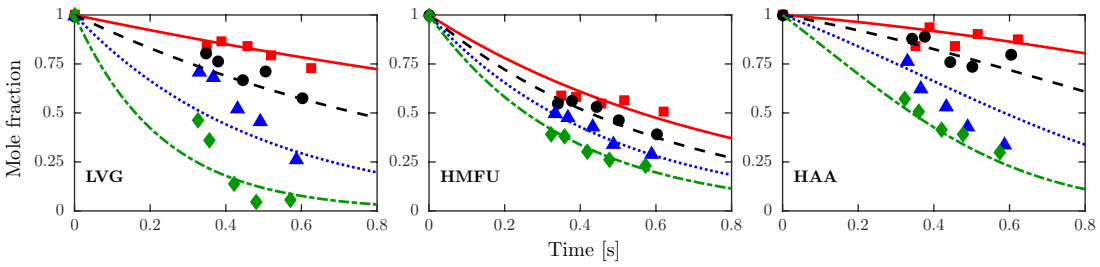

Figure 2.1: Pyrolytic decomposition of levoglucosan (LVG), hydroxyacetaldehyde (HAA), and 5-hydroxymethyl furfural (HMF): Comparison between simulation results using the reference chemical model (lines) and experiments (Shin et al. [163], symbols). Different symbols indicate different temperatures (square: 898 K, circle: 923 K, triangle: 948 K, and diamond: 973 K).

2.4 Reduced chemical model development

The reference kinetic model for the gas phase reactions described in the previous section is too complex to be used even in simple CFD configurations. Therefore, the objective is to identify the most important chemical reaction pathways for gasification. This section describes how this objective is achieved by extracting a compact model with 39 species and 118 reactions from the reference model with 396 species and 3210 reactions. Note that the reduction process does not affect the solid-to-gas devolatilization model [33] in any way.

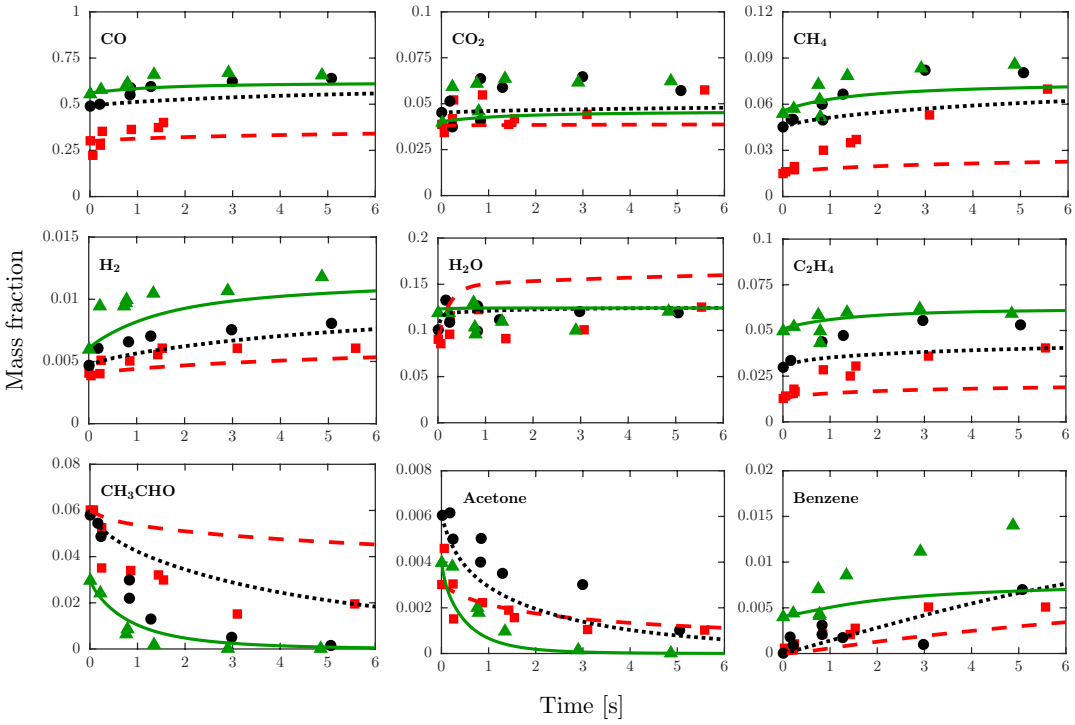

Figure 2.2: Pyrolytic decomposition of major cellulose devolatilization products: Comparison between simulation results using the reference chemical model (lines) and experiments (Norinaga et al. [123], symbols). Different symbols indicate different temperatures (square: 973 K, circle: 1023 K, and triangle: 1073 K).

2.4.1 Relevant gasification conditions

As all reactions are not important at all conditions, the very first task is to identify the conditions at which gasification will most likely take place in an actual gasifier, in particular, the heating rate to which biomass will be subjected. This step will help refine the range of conditions over which the reduced chemical kinetic model should be valid, and focus the reduction procedure on the relevant kinetics. Table 2.1 shows the parameters used to represent the devolatilization of biomass particles in a FBR. The size of biomass particles varies between 300

μm to 1 mm to represent the general size range found in many laboratory gasification studies. Gas phase properties, such as density, specific heat capacity, conductivity, and viscosity, are computed assuming pure nitrogen at the temperatures and pressure stated in Table 2.1. To estimate typical heating rates, the Nusselt correlation from Gunn [72] is used along with the parameters from Table 2.1. For these parameters Biot numbers for the biomass particles vary between 0.34 to 0.58, implying that thermal gradients will be present in the biomass particles. However, the purpose of Table 1 is to establish relevant conditions in order to apply our chemistry reduction algorithms. For this, an assumption of constant internal temperature suffices. Simulations of biomass devolatilization using the Corbetta et al. model [33], and neglecting secondary gas phase reactions, show that most primary gases are released from the biomass between 773 K and 873 K. With this assumption, Fig. 2.3 indicates that particles of size between 300 μm and 1 mm experience a heating rate of $O(10^3)$ K/s during devolatilization. Therefore, a value of 1000 K/s is chosen as representative of the heating rate for the reduction procedure.

Table 2.1: Parameters used to estimate relevant biomass particle heating rates for the chemistry reduction procedure.

Parameter	Value
Gas temperature	1073 K - 1273 K
Particle temperature during devolatilization	773 K - 873 K
Pressure	1 atm
Solid heat capacity	2300 J/kg.K
Biomass bulk density	650 kg/m^3
Biomass particle diameters	300 μm - 1 mm

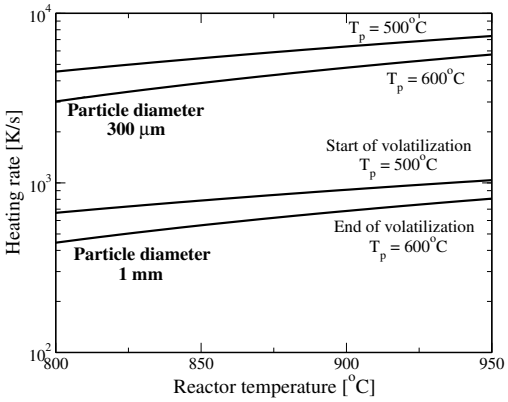

Figure 2.3: Typical heating rates experienced by the biomass during gasification at the conditions described in Table 2.1.

2.4.2 Simulation configuration

The relative importance of chemical reaction pathways as estimated by the DRGEP reduction methodology depends on the chemical compositions and sample kinetic trajectories on which it is applied. As the reference model is too complex to be used in a realistic reactor configuration, we choose a statistical treatment to sample as broadly as possible the chemical states and trajectories occurring in a gasification reactor. For this purpose, the computationally inexpensive and idealized Partially Stirred Reactor (PaSR) is used. Inside a PaSR, the composition and properties of the fluid are represented by an ensemble of notional particles each carrying its own species composition and temperature. The properties of each notional particle evolve due to mixing, reaction, and inflow/outflow events such that the mean thermochemical properties of the represented fluid are statistically spatially homogeneous, but the fluid itself is imperfectly mixed at the molecular level. The use of a PaSR as sampling tool forces the reduction to be quite conservative, thereby preventing important pathways to be removed from the reduced kinetic model. It must also be noted that because a PaSR is not a mathematical representation of a physical system,

simulation results cannot not be directly compared to, or interpreted in light of, experimental data.

The fluid is assumed to be an ideal gas-phase mixture that evolves in the PaSR at a constant pressure, so that the full thermochemical state or composition of the mixture Φ is completely characterized by the species mass fractions $\mathbf{Y}$ and the mixture enthalpy $\mathcal{H} : \Phi \equiv \{\mathbf{Y}, \mathcal{H}\}$. The PaSR is continuously fed by a user-specified number n_{str} of inflow streams of prescribed compositions Φ_{str}; it will be described later for the biomass system under consideration. At any time t, the reactor contains a constant, even number n_p of notional particles, the i^{th} particle having composition $\Phi^{(i)}(t)$. These compositions evolve in time due to mixing, reaction, and inflow and outflow events. These processes are described in more detail.

Inflow and outflow events occur at discrete times and change the particle composition Φ in a discontinuous manner. In the inflow/outflow event, n_{in} particles are selected at random with equal probability, and their compositions are replaced by the inflow streams' compositions. The integer number n_{in} (= $n_p \times \Delta t/\tau_{res}$) is chosen according to the specified mean residence time τ_{res} and time step Δt. Between these discrete times, the composition evolves by a mixing fractional step and a reaction fractional step. In the mixing fractional step, particles are paired and ordered so that particles i and i+1 are partners for odd i ($1 \leq i < n_p$), and the ordinary differential equations,

$$\frac{d\Phi^{(i),m}}{dt} = -\frac{\left(\Phi^{(i)}(t) - \Phi^{(i+1)}(t)\right)}{\tau_{mix}} \tag{2.1}$$

$$\frac{d\Phi^{(i+1),m}}{dt} = -\frac{\left(\Phi^{(i+1)}(t) - \Phi^{(i)}(t)\right)}{\tau_{mix}} \tag{2.2}$$

are solved for each pair of particles over time interval Δt. In this equation, τ_{mix}

is the specified pairwise mixing time scale. At each time step, n_{pair} particles are selected randomly with equal probability and shuffled to change partners. The integer number n_{pair} ($= n_p \times \Delta t/\tau_{pair}$) is chosen according to the specified pairing time τ_{pair}, typically taken equal to τ_{mix}. The compositions after mixing evolve under isobaric, adiabatic conditions over a time Δt according to

$$\frac{d\Phi^{(i),m}(t)}{dt} = \mathbf{S}\left(\Phi^{(i),m}(t)\right) \tag{2.3}$$

where $\mathbf{S}$ is the chemical source term defined by the user-provided reaction mechanism. This reaction fractional step finally yields the particle compositions at $t + \Delta t$: $\Phi^{(i)}(t + \Delta t)$.

The PaSR simulation setup described here will be used to provide relevant compositions of biomass devolatilization products expected to be found in real gasification reactors and to compare the reduced model developed in this section with the reference model.

2.4.3 Reduction using DRGEP

The automatic chemical mechanism reduction technique DRGEP [141] is used to extract a reduced model from the reference, detailed, model. The reduction procedure follows the steps outlined in Pepiot et al. [141] for species and reaction elimination, and is performed using the YARC reduction tool [137], a Perl/C implementation of DRGEP and associated reduction techniques.

- **Reduction targets selection** The first step in the reduced model development is to identify a set of targets $\mathcal{T}$, most often specific species, that the reduced model must reproduce accurately. In biomass gasification, it is

desirable to predict the yield of gaseous products and tar species. Therefore, 5 major gas products: CO, CO_2, H_2, CH_4, and C_2H_4, water (H_2O), and 3 major tar species: benzene (C_6H_6, a single-ring aromatic), naphthalene ($C_{10}H_8$, a polycyclic aromatic), and phenol (C_6H_6O, an oxygenated aromatic) are selected as targets. Moreover, 13 primary devolatilization products described by the reference devolatilization model, such as HAA, HMFU, LVG, are also incorporated into the targets list.

- **Sample Composition Database** To evaluate the relative importance of species and reactions for the given set of targets, DRGEP requires an ensemble of sample compositions representative of the simulations in which the reduced model will eventually be used. For this purpose, we use a PaSR configuration, and assume that the particles in the PaSR simulation will follow trajectories in composition space that are representative of those they would encounter in an actual reactor. The simulation parameters are chosen based on previous experience and best practices [98] to ensure a broad range of compositions relevant for our application, and the residence time is adjusted to match the characteristic timescale of the overall pyrolysis chemistry process.

  Two inflow streams are continuously fed to the PaSR to represent the release of the primary products from the devolatilizing biomass into the hot nitrogen environment. The first inflow stream consists of nitrogen gas at temperatures varying between 1073 K to 1273 K, while the second inflow stream consists of the primary products released during biomass devolatilization. The second stream needs to account for the fact that a gasification reactor contains biomass particles at different stages of devolatilization, acting as variable sources of primary products. To include this vari-

ability, the biomass devolatilization process is represented stochastically by sampling from the probability distribution function (PDF) of the extent of biomass devolatilization. This PDF is constructed by simulating biomass devolatilization *a priori* using the reference chemical model.

The parameters used for these simulations are summarized in Table 2.2. The PaSR simulations are performed for three nitrogen temperatures: 1073K, 1173K, and 1273K. A database of 18,000 distinct chemical compositions is created by randomly sampling the compositions encountered in the PaSR simulations.

Table 2.2: PaSR simulation parameters

Parameter	Value
Number of notional gas particles in PaSR	96
Gas residence time	3 s
Mixing time	0.3 s
Biomass particle heating rate	1000 K/s
Temperature of raw biomass	300 K
Temperature of pure nitrogen stream	1073 K to 1273 K
Normalized mass flow rates of nitrogen stream	0.9
Normalized mass flow rates of biomass stream	0.1

- **Automatic reduction and error estimation** The automatic reduction procedure proceeds through two distinct steps. In the first step, DRGEP analyzes the composition database and quantifies the coupling between species and reactions in the chemical mechanism for the chosen target species in the form of importance coefficients also known as DRGEP coefficients. Species and reactions with the lowest value of DRGEP coefficients

are removed from the mechanism in an iterative manner providing a list of kinetic models of decreasing complexity. More details about the implementation of DRGEP technique can be found for example in [106].

In the second step, the PaSR test configuration (parameters provided in Table 2.2) is simulated using each of the reduced models generated in the first stage, and *a posteriori* errors on the targets are computed, defined for any target $\mathcal{T}$ as

$$\varepsilon_{\mathcal{T}} = \frac{\int_0^{t_{end}} |\langle \mathcal{T} \rangle^D (t) - \langle \mathcal{T} \rangle^R (t)| dt}{\int_0^{t_{end}} |\langle \mathcal{T} \rangle^D (t)| dt} \tag{2.4}$$

In this equation, $\langle \mathcal{T} \rangle (t)$ designates the average of quantity $\mathcal{T}$ at time t over all particles contained in the PaSR, and t_{end} is taken here as 15 PaSR residence times. *A posteriori* errors as a function of the number of species, n_S for a few targets are shown in Fig. 2.4. The reduction process provides several mechanisms with decreasing number of species and reactions; we choose the smallest possible mechanism for which the error is less than 10% for most of the species, and at most a factor of 2 for a few groups of species. The mechanism with 60 chemical species and 486 reactions is found to be the smallest acceptable model generated automatically by the DRGEP procedure and is shown by a dotted line in Fig. 2.4.

2.4.4 Additional reduction

In the DRGEP technique, a species or a reaction is removed from the chemical mechanism only when it is identified as unimportant for every single composition in the database, which imposes a stringent criterion on species and reaction removal. A species or a reaction can be important for the local dynamics of

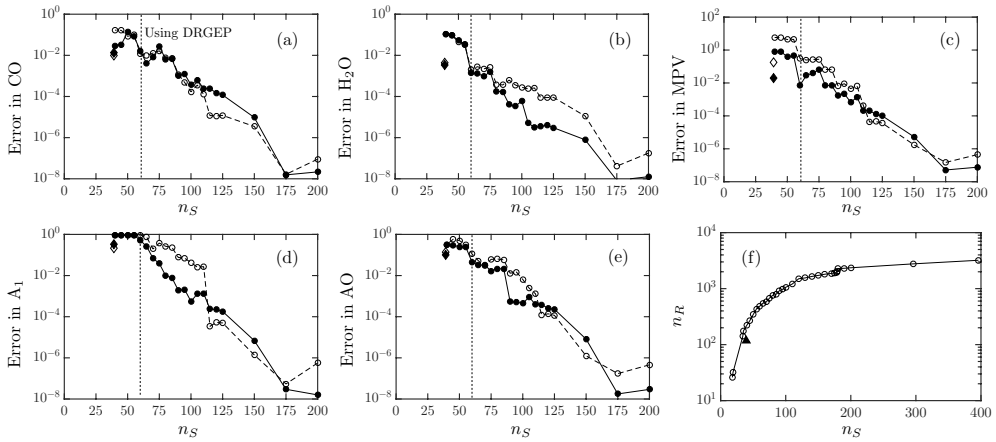

Figure 2.4: Error in the PaSR predictions as a function of the number of species n_S retained in the skeletal model during the reduction process: (a) CO, (b) H_2O, (c) MPV, (d) A_1, (e) AO, and (f) number of reactions n_R retained in the model. Filled symbols: PaSR nitrogen stream temperature is 1073K; open symbols: PaSR nitrogen stream temperature is 1273K. Circles: automatic reduction; diamonds: semiautomatic reduction with quasi-steady state assumption.

a target, but may not impact its global statistical behavior. Several techniques have been developed in recent years to identify those additional species and reactions, for example, the DRGEP with Sensitivity Analysis method [121]. In this work, we use an *ad-hoc* semi-automatic technique that quantifies the impact of species and reactions on the global statistical behavior of the targets. This technique utilizes the global production/consumption rates of each species for every reaction obtained from the simulations of the PaSR test configuration using the intermediate mechanism. The coupling between species and reactions on the targets is quantified in a manner similar to the DRGEP technique, but using the global production and consumption rates of species instead. Potential species and reactions that may have a minimal impact on the prediction of global statistics of the targets are removed from the mechanism, and the resulting model is simulated in the PaSR test configuration to calculate *a posteriori*

errors on the targets using Eqn. 2.4. A 44 species and 118 reactions mechanism is found to be the smallest acceptable model after this step, and is shown by diamond symbols in Fig. 2.4.

2.4.5 Quasi-steady state approximations

Once the above-mentioned strategies have removed as many species and reactions as possible, quasi-steady state (QSS) approximations are introduced that replace the differential equation for a given species by an algebraic expression much faster to solve. All suitable QSS species are computed using algebraic expressions consisting of non-QSS species. To keep the calculation of QSS species simple and fast, it is made sure that all of the algebraic expression are linear [140]. With this constraint, 5 QSS species are identified: C_2H_5, CH_2OH, CH_2CHO, C_7H_7, and CH_2CO.

The final reduced kinetic model has 39 non-QSS species (including N2), 118 reactions (including both forward and backward reactions), and 5 QSS species.

2.5 Validation of the reduced model

In this section, the accuracy of the reduced model (39 species and 118 reactions) developed in Section 2.4 is assessed for a number of configurations. Three different test cases are performed: 1) The PaSR test configuration is simulated using both the reduced and the reference model, and major product and tar species are compared; 2) The reduced model is used in a zero-dimensional reactor configuration to simulate the pyrolysis experiments of Shin et al. [163]; 3) The reduced

model is integrated with the CFD solver NGA [46] to simulate biomass gasification in the laboratory-scale Drop Tube Reactor (DTR) of Chen et al. [29]. These validation cases are discussed in the following subsections.

2.5.1 Comparison in a partially stirred reactor

The PaSR configuration used to create composition database in Section 2.4 is used again here to compare the reduced model to the reference model for the temperatures ranging from 1073 K to 1273 K. The parameters used for these simulations are shown in Table 2.2. After a statistically steady state is reached, the mass fractions of gaseous products and tar species are averaged over 10 residence times to get mean steady state mass fractions. Since the reaction pathways are significantly altered due to the high reduction ratio, the mass fraction of a few species are not compared individually. Instead, these species are divided into different groups based on their molecular weights, and the sum of their mass fractions is compared.

Figure 2.5 compares the mean steady state mass fractions of relevant individual species and groups of species obtained from the reduced and reference model. Predictions of the reduced and reference model for major product gases: CO, CO_2, CH_4, H_2, and C_2 (species with 2 carbon atoms), water (H_2O), and three classes of tars: single-ring aromatics (A_1), poly-aromatic hydrocarbons (PAH), and oxygenated aromatics (AO) are in good agreement. In addition, the reduced model is also able to predict light (LPV), medium (MPV), and heavy (HPV) weight primary devolatilization products, and small radicals pool (RAD). Those acronyms and their definitions are summarized in Table. 2.3.

Table 2.3: List of species and group of species, and their acronyms.

Acronyms	Name
A_1	Single ring aromatics (e.g. Benzene)
AO	Oxygenated aromatics (e.g. Phenol)
C_2	Gases containing two carbon atoms (e.g. Ethylene)
HAA	Hydroxyacetaldehyde
HMF	Hydroxymethyl Furfural
HPV	Heavy weight Primary vapors (7+ carbon atoms, e.g. p-Coumaryl)
MPV	Medium weight Primary vapors (4-6 carbon atoms, e.g. Levoglucosan)
LPV	Light weight Primary vapors (2-3 carbon atoms, e.g. Glyoxal)
LVG	Levoglucosan
PAH	Polyaromatic hydrocarbons (e.g. Naphthalene)
RAD	Small radicals pool (e.g. H, OH)

The PaSR simulations are carried out on a Beowulf cluster with Nehalem X series processors. The time per iteration per processor for using the reduced model is $O(10^{-3}s)$ and for the reference model it is $O(10^{-1}s)$, corresponding to a reduction in the CPU time by ~99% by the reduced model. It must be noted that in the PaSR simulations the majority of the time is spent on the integration of the chemical source terms, therefore, the saving in the CPU time is dominated by this term. Reduction in computational expense is expected to be even higher in CFD simulations as additional scalar transport equations need to be solved for each species at every grid point in the computational domain.

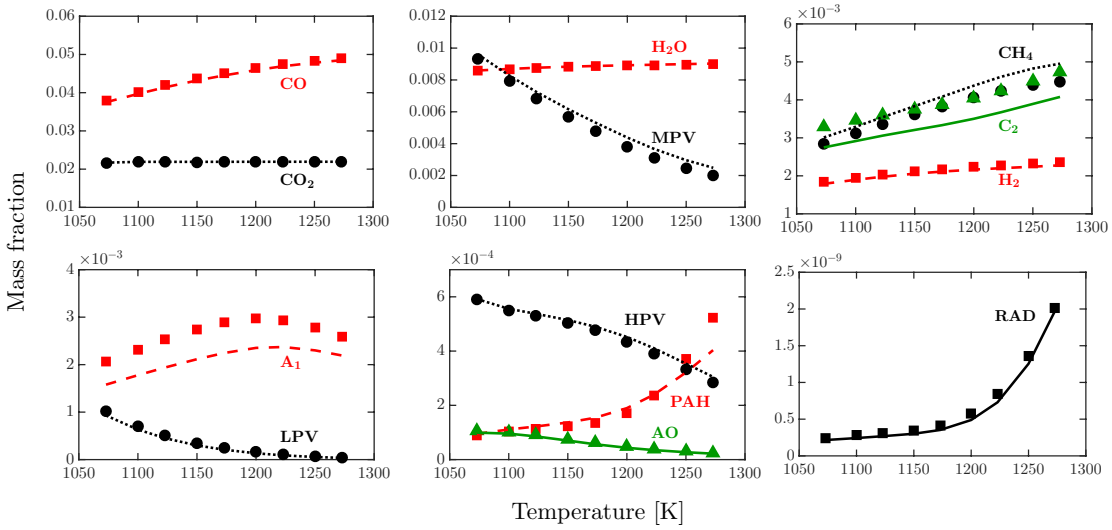

Figure 2.5: Statistically steady state mass fractions of various light gases, tar species, devolatilization products, and small radical pool: Comparison between the reduced model (symbols) and the reference chemical model (lines) in a Partially Stirred Reactor (PaSR) configuration for the temperature ranging from 1073 K to 1273 K. Expanded species names are provided in section 2.5.1.

2.5.2 Pyrolysis in a tubular reactor

The reduced model is used to simulate the tubular reactor experiments of Shin et al. [163] described in Section 2.3.2. Simulation results are compared with the experimental measurements in Fig. 2.6, and show overall a good agreement. When compared to the simulations performed with the detailed, reference mechanism (Fig. 2.1), we see that the prediction of hydroxymethyl furfural decomposition is virtually unchanged by the reduction process, but more significant changes are observed for levoglucosan and hydroxyacetaldehyde, for which the decomposition rate has been reduced. While agreement with the experimental data is still satisfactory, those results indicate a larger sensitivity of

those molecules to the underlying small radical chemistry.

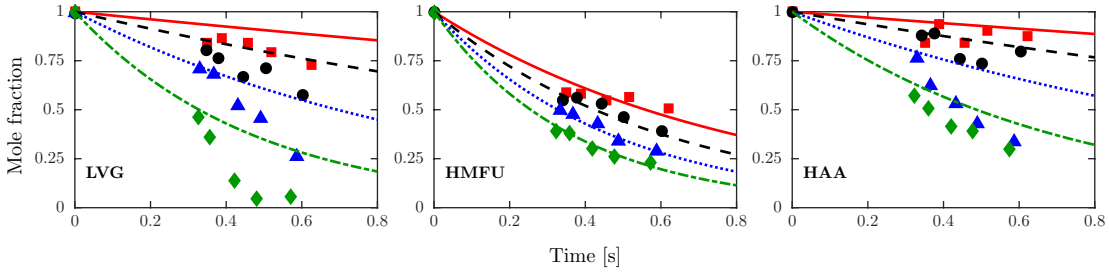

Figure 2.6: Pyrolytic decomposition of Levoglucosan (LVG), Hydroxyacetaldehyde (HAA), and Hydroxymethyl Furfural (HMFU): Comparison between simulation results using the reduced kinetic model (lines) and experiments (symbols, Shin et al. [163]). Different symbols indicate different temperatures (square: 898 K, circle: 923 K, triangle: 948 K, and diamond: 973 K).

2.5.3 Fast pyrolysis of biomass in a drop tube reactor

Numerical simulations of the one-dimensional DTR of Chen et al. [29] are conducted and compared to the experimental results. A schematic of the experimental DTR can be seen in Fig. 2.7. Chen et al. [29] studied gasification of millimetric sized biomass particles (beech wood) in the DTR at 1073 K and 1223 K. In the experiments, particles are flake-like and are characterized by their equivalent spherical diameters. Biomass particles and nitrogen stream are continuously injected from the top of the reactor, while the exhaust gas is sampled at the bottom. A portion of this exhaust gas is then examined by several gas analyzers. The distance between the locations of biomass injection and gas collection is varied to get four residence lengths: 0.3 m, 0.5 m, 0.7 m, and 0.9 m. The total amount of gas, tar, and char produced is measured at these residence lengths. Moreover, yields of major gas phase components are also provided.

The DTR presents a multiphase and multiphysics system, therefore, simulations of this reactor require a reactive multiphase flow solver. For this purpose, the reduced model and the biomass devolatilization model are integrated with the reactive multiphase CFD solver NGA [46], with a Euler-Lagrange strategy [25] to model gas-solid flows. NGA has been extensively validated and used for various DNS and LES multiphase reactive flow systems [44, 180, 81, 43, 45, 82, 139, 177]. Simulations were conducted for biomass particles with the equivalent spherical diameter (d_p) of 520 μm and two gas temperatures: T = 1073 K (simulation $\mathcal{S}1$) and 1223 K (simulation $\mathcal{S}2$). Parameters used for $\mathcal{S}1$ and $\mathcal{S}2$ are provided in Table 2.4. In the DTR simulations, two modeling issues are encountered related to: 1) the reference devolatilization kinetics model and 2) the shape of the particles. These are discussed in the following two subsections before the results of the DTR simulations are presented.

Biomass devolatilization model. In the DTR simulations, the biomass devolatilization chemistry is modeled by the reference devolatilization model discussed in Section 2.3.1. Preliminary DTR simulations could not accurately predict the experimental yields of CH_4, C_2H_4, and solid residue. This difference is attributed to the fact that a significant portion of these two gases remains trapped in the solid matrix in the chemisorbed state. For simulation $\mathcal{S}1$, Fig. 2.8(a) shows the evolution of the trapped species ($\mathcal{T}_{sp}$ $\equiv$ CO, CO_2, and CH_3OH) that are completely released from the biomass particle during the devolatilization, whereas Fig. 2.8(b) shows that a few trapped species ($\mathcal{T}^*_{sp}$ $\equiv$ COH_2, CH_4, C_2H_4, and H_2) remain inside the biomass particle even after the complete devolatilization. Figure 2.8(c) shows that even long after the completion of biomass devolatilization, the amount of solid residue is much higher than that of char; this difference is also attributed to the trapped species $\mathcal{T}^*_{sp}$.

Table 2.4: Parameters for the drop tube reactor simulation.

Parameter	Value
Domain length ($L_x \times L_y \times L_z$)	0.9 m × 0.02 m × 0.02 m
Number of cells ($n_x \times n_y \times n_z$)	900 × 1 × 1
Inlet nitrogen velocity	0.279 m/s
Temperature of inlet nitrogen stream	1073 K ($\mathcal{S}1$) and 1223 K ($\mathcal{S}2$)
Injection rate of biomass particles	7.545×10^{-7} Kg/s
Biomass density	710 Kg/m^3
Biomass particle size	520 μm
Biomass composition (wt%)	
Cellulose	43.91
Hemicellulose	23.85
C-rich lignin	3.24
H-rich lignin	14.99
O-rich lignin	6.71
Ash	0.4
Moisture	6.9

This is corroborated by the fact that the predicted value of char, Y_{char}=0.10 is close to the solid residue measured in the experiments, SR_{exp}=0.08 ± 20%.

Similar discrepancies have been very recently investigated by Anca-Couce et al. [5], who performed biomass pyrolysis experiments and used the reference devolatilization model to predict the experimental yields of various species. They introduced several modifications in the devolatilization mechanism to significantly improve the agreement between the modeled results and their exper-

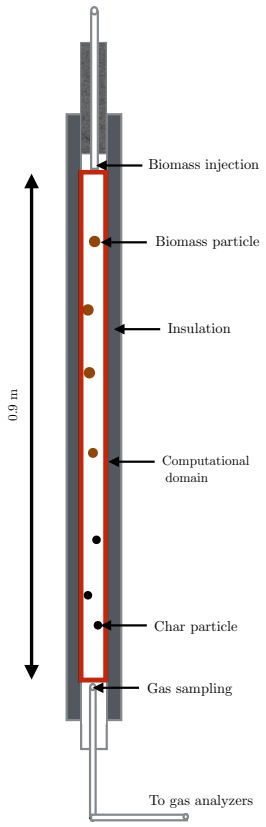

Figure 2.7: Schematic of the experimental Drop Tube Reactor [29], the computational domain considered in this study is indicated in red

imental database, mainly for the yields of light hydrocarbons and the yield and composition of char. The focus of the present paper being the secondary gas-phase reactions, we introduce here a simple *ad hoc* modification of the Corbetta et al. model [33] considering only the current experiment at hand, as described below, and refer the reader to the study of Anca-Couce et al. [5] for a more comprehensive treatment of this issue. To improve the predictions of CH_4, C_2H_4, and solid residue, we adjust the parameters of the reactions, present in the reference devolatilization model, governing the release of $\mathcal{T}^*_{sp}$. In the reference devolatilization model, activation energies (E_{act}) for the release of $\mathcal{T}^*_{sp}$ are much higher compared to E_{act} for the release of $\mathcal{T}_{sp}$. To make the release of $\mathcal{T}^*_{sp}$ faster,

we replace the E_{act} for the release of $\mathcal{T}^*_{sp}$ by the E_{act} for the release of trapped CO. Simulation $\mathcal{S}1$ is repeated with the modified values of the E_{act}; the resulting evolution profiles of $\mathcal{T}_{sp}$ and $\mathcal{T}^*_{sp}$ are shown in Fig. 2.8(d) and Fig. 2.8(e), respectively, and the evolution of char and solid residue is shown in Fig. 2.8(f). These figures show that as the devolatilization proceeds all the trapped species get released from the biomass particles and the amount of solid residue, SR_{sim}=0.1 is close to the experimental value, SR_{exp}=0.08 ± 20%. Therefore, the reference devolatilization model with the modified value of E_{act} for $\mathcal{T}^*_{sp}$ is used in the DTR simulations.

Shape of the particles Biomass particles used in the experiments have flake-like shape. The shape of the particle affects the drag force from the surrounding gas and the heat transfer rate experienced by the particle. In the simulations particles are treated as spheres, therefore, a correction must be made to include the effect of the proper particle shape while calculating drag force and heat transfer rate. Chen [28] experimentally measured the slip velocity of the biomass particles and estimates a correction factor of **1.5** that can be multiplied with the drag correlation for a spherical particle to estimate the drag on a flake-like particle. In the DTR simulations, this correction factor is used in the drag calculation for the biomass particles. Although drag is corrected for the flake-shaped particles, any correction for heat transfer rate is not provided in the experimental study. Therefore, we calculate correction factors to estimate the convective and radiative heat transfer rates of the flake-shaped particles based on the calculation for spherical particles.

Convective heat transfer rate for a particle can be expressed as

$$q_{conv} = hA\Delta T \tag{2.5}$$

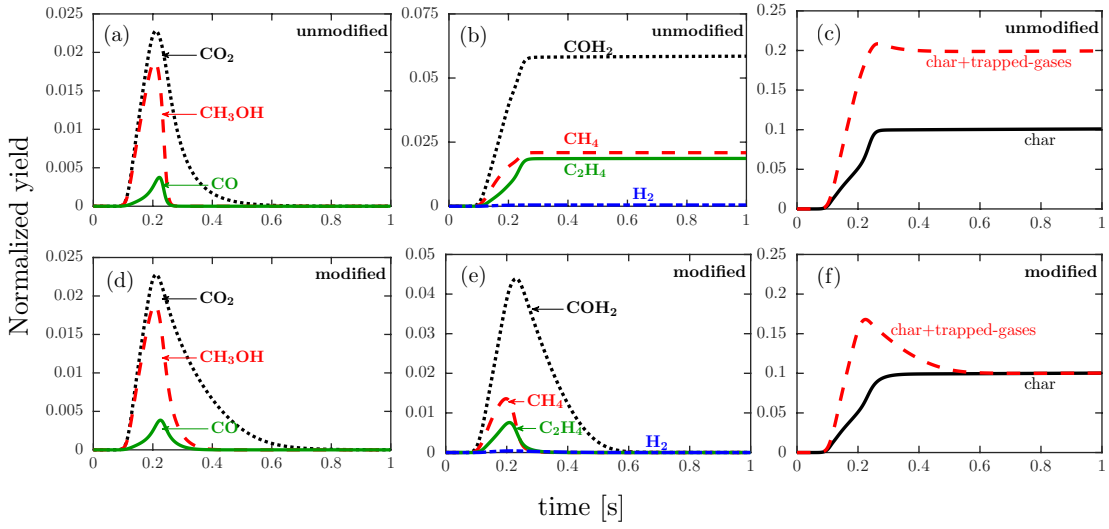

Figure 2.8: Evolution of trapped species, char, and solid residue during biomass devolatilization in DTR simulation $\mathcal{S}1$ using the unmodified reference devolatilization model described in section 2.3.1 (first row) and the modified model described in section 2.5.3 (second row). (a) and (d) show the evolution of trapped species that are completely released from the biomass using the unmodified and modified devolatilization model, respectively. (b) and (c) show that for the original devolatilization model some trapped species are not released from the biomass, while those trapped species are released after the modification as shown in (e) and (f). Yields are normalized with the initial mass of biomass particle.

where A is the surface area of the particle, ΔT is the temperature difference between the particle surface and the surrounding gas, and h is the convective heat transfer coefficient. h can be calculated from the Nusselt number, Nu, as $h = \frac{Nu\lambda_f}{l}$, where λ_f is thermal conductivity of the gas surrounding the particle and l is the characteristic length, which is equal to the diameter (d_p) for a sphere and the thickness (t_p) for a flake-shaped particle. The Nusselt number is calculated using Gunn's correlation [72]. Average area of the flake-shaped particles is calculated based on the experimental measurements [28] of particle dimensions. The

ratio of the average area of the flake-shaped particles (A^*) to that of an equivalent spherical particle (A) is calculated to be **1.33**. Using the thickness, t_p, as the characteristic length in the expression for h, the convective heat transfer rate for the flake-shaped particles becomes

$$q^*_{conv} = \left(\frac{d_p}{t_p}h\right)\left(\frac{A^*}{A}A\right)\Delta T \tag{2.6}$$

For a biomass particle of equivalent diameter d_p = 520 μm, the experimentally measured average particle thickness (t_p) is 250 μm. Substituting these values in Eq. 2.6, we get

$$q^*_{conv} = \left(\frac{520}{250}h\right)(1.33A)\,\Delta T \sim 2.8hA\Delta T = 2.8q_{conv} \tag{2.7}$$

Equation 2.7 implies that the convective heat transfer rate for the flake-shaped particles (corresponding to an equivalent spherical diameter of 520 μm) is about 2.8 times faster than that for the equivalent spherical particles.

The radiative heat transfer rate from the reactor walls to the biomass particle is modeled by

$$q_{rad} = A\omega_p\sigma(T^4_{wall} - T^4_p) \tag{2.8}$$

where, ω_p is the particles emissivity, σ is the Stefan-Boltzmann constant (= 5.6704×10^{-8} Wm^2K^{-4}), T_{wall} is the reactor wall temperature, and T_p is the particle surface temperature. ω_p is calculated as a linear combination of wood (ω_w=0.7) and char emissivity (ω_c=0.92) [133]. For a flake-shaped particle, A is replaced by A^*, and we get

$$q^*_{rad} = \left(\frac{A^*}{A}\right)A\omega_p\sigma(T^4_{wall} - T^4_p) = 1.33q_{rad} \tag{2.9}$$

Equation 2.9 implies that the radiative heat transfer rate for the flake-shaped particles (corresponding to an equivalent spherical diameter of 520 μm) will be about 1.33 times faster than that of the equivalent spherical particles.

To evaluate the effect of these corrections for convective and radiative heat transfer rates on biomass devolatilization, $\mathcal{S}1$ is performed with the corrected rates (q^*_{conv} and q^*_{rad}) and the uncorrected rates (q_{conv} and q_{rad}). Fig. 2.9 shows that using the corrected heat transfer rates significantly improves the prediction of the shrinkage rate of the particles. Therefore, in the DTR simulations, convective and radiative heat transfer rates for the spherical particles are multiplied with 2.8 and 1.33, respectively, to make correction for the shape of the particles.

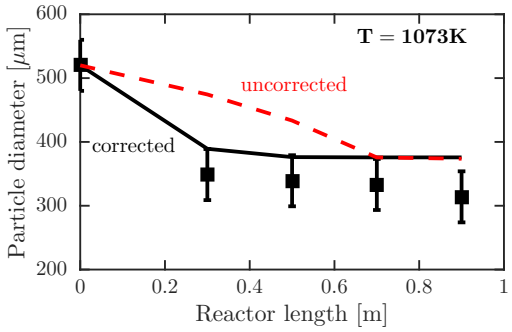

Figure 2.9: Biomass diameter (for simulation $\mathcal{S}1$) at various reactor lengths: Comparison between experimental measurements (symbols), and simulation predictions with corrected heat transfer rate (solid line) and uncorrected heat transfer rate (dashed line).

Comparison with experimental data. After incorporating the modifications in the reference devolatilization model and the heat transfer rates, simulations $\mathcal{S}1$ and $\mathcal{S}2$ are run until steady state is reached. Figure 2.10 compares the simulation predictions of the mass fraction of major gas products and particle diameters at various reactor lengths to the experimental values. Agreement between the simulation predictions and experimental measurements is very good considering the possibility of the high degree of variability in various parameters and physical properties. These simulations are performed on a single core of a MacBook laptop and required O(1 hour) to reach steady state, which shows the

affordability of the current reduced model to simulate laboratory-scale reactors.

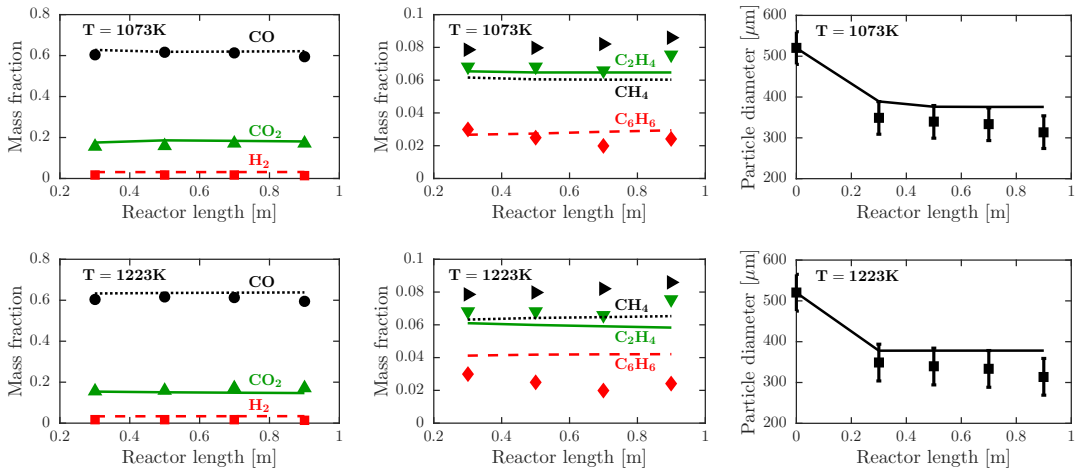

Figure 2.10: Steady state mass fraction (dry basis) of various gas species and particle diameter at different reactor lengths: Comparison between simulation results (lines) and experimental measurements (symbols) for particle diameter, d_p=520 μm, and two gas temperatures: 1073 K and 1223 K.

2.6 Application to a fluidized bed reactor

The reduced gas-phase chemistry model, coupled with the biomass devolatilization model of Corbetta et al. [33], is used to simulate a pseudo-2D configuration (rectangular geometry) of an experimental FBR [80] using NGA [46]. Parameters used in this simulation are reported in Table 2.5. Initially, the sand bed is fluidized without biomass particles by injecting the nitrogen gas from the bottom of the reactor. Once a fluidized sand bed is achieved, biomass particles are injected into the reactor at a constant mass flow rate. Simulation is run long enough to reach a statistically steady state. Figure 2.11 shows the in-

stantaneous values of the mass fraction of various classes of tar normalized by their maxima at statistically steady state. The location of the mass fraction maximum of oxygenated aromatics (AO) is very different from that of single-ring (A_1) and multiple-ring (PAH) aromatics. It indicates that different tar species can have different length and time scales associated with their formation and consumption. The mass fraction of the major gas and tar species at different reactor lengths are shown in Fig. 2.12. As expected, CO is the major gas product followed by CO_2, CH_4, C_2, and H_2. Among tars, single-ring aromatics are the major species followed by oxygenated aromatics, and Polycyclic Aromatic Hydrocarbons (PAH). Another important observation made from Fig. 2.12 is that the mass fraction of all the light gases, and A_1 and PAH increase along the reactor height, while it decreases for AO.

The simulation was performed on 96 cores on the cluster mentioned in Section 2.5.1, and required 3000 CPU hours and 9000 CPU hours per flow-through time (0.75 s) for pure sand fluidization case and the reacting case with biomass injection, respectively. This simulation shows the ability of the reduced model to be used with a CFD solver to simulate laboratory-scale FBR in an affordable manner. The present reduced model combined with a CFD solver provides the capability to track the evolution of major gas and tar species for different operating conditions.

2.7 Conclusion

An adequate description of the chemical kinetics in the CFD tools is imperative for the detailed simulations of biomass gasification, however, the large size

Table 2.5: Parameters for the FBR simulation.

Parameter	Value
Domain length ($L_x \times L_y \times L_z$)	0.15 m × 0.02 m × 0.0015 m
Number of cells ($n_x \times n_y \times n_z$)	300 × 40 × 3
Inlet nitrogen velocity	0.2 m/s ($6u_{mf}$)
Inlet nitrogen temperature	1073 K
Number of sand particles	10^5
Size of sand particles	200 μm
Density of sand particles	2650 Kg/m^3
Injection rate of biomass particles	5×10^{-6} Kg/s
Size of biomass particles	200 μm
Density of biomass particles	907 Kg/m^3

Biomass composition (wt%)	
CELL	47.24
HCELL	31.49
LIGC	2.78
LIGH	6.48
LIGO	4.63
Ash	0.37
Moisture	7.0

of detailed mechanisms make their use prohibitive in the CFD simulations. In this work, we assemble a detailed chemical model (396 species, 3210 reactions) for the secondary gas-phase reactions of biomass gasification and reduce it to a compact model (39 species, 5 quasi-steady state species, and a total of 118

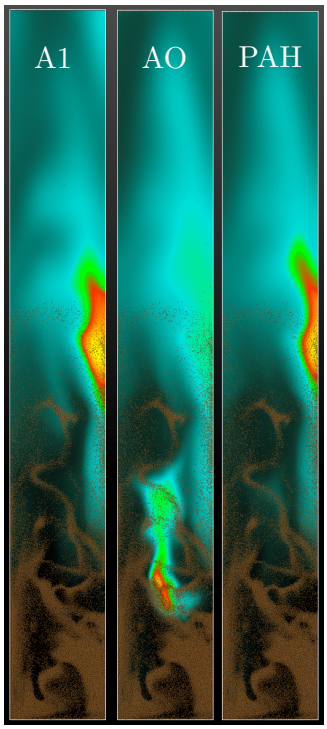

Figure 2.11: Instantaneous mass fraction of different classes of tar: A_1 (single-ring aromatics), AO (Oxygenated aromatics), and PAH (Poly Aromatic Hydrocarbons), scaled by their individual maxima in the pseudo two-dimensional FBR simulation.

reactions) using automated strategies. The reduced model shows very good reproducibility of the statistical yields of various species of interest at a fraction of computational cost compared to the detailed model. The savings in computational time are expected to be higher in CFD simulations where a set of extra Partially Differential Equations (PDEs) need to be solved for the scalar transport equations. The reduced model, integrated with the CFD solver NGA, is used to simulate a laboratory-scale Drop Tube Reactor (DTR) experiment showing good agreement with the experiments. By simulating a pseudo two-dimensional FBR with the reduced model, it is shown that an adequate description of the gas phase reactions can be used with CFD tools in a computationally affordable manner. The reduced model developed here is small enough to be integrated

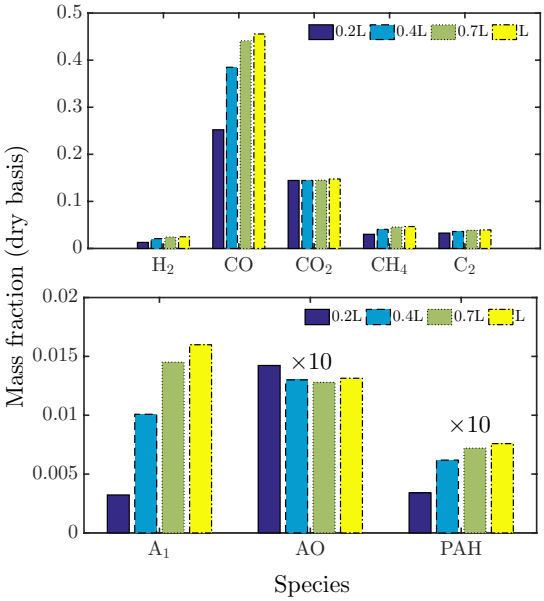

Figure 2.12: Steady state mass fraction of major gas and tar species at different reactor lengths in the pseudo two-dimensional FBR simulation. Mass fractions of AO and PAH are multiplied by 10 to compare their behavior with A_1.

with a CFD solver to study the secondary gas phase reactions of biomass gasification in laboratory-scale reactors.

CHAPTER 3

ON THE VALIDATION OF A ONE-DIMENSIONAL BIOMASS PYROLYSIS MODEL USING UNCERTAINTY QUANTIFICATION

Reproduced with permission from Goyal, H.; Pepiot, P. On the validation of a one-dimensional biomass pyrolysis model using uncertainty quantification. ACS Sustainable Chemistry & Engineering 2018, DOI 10.1021/acssuschemeng.8b02493.

3.1 Abstract

Predictive modeling tools have the potential to accelerate the development and deployment of biomass thermochemical conversion. Considerable progress has been made in the modeling of biomass pyrolysis at the particle level, where chemical kinetics and transport processes are coupled. However, rigorous validation of the corresponding models is challenging because of the considerable uncertainty in the values of several biomass properties. Towards this end, we use the principles of uncertainty quantification (UQ) for a rigorous analysis of the validity of a commonly used one-dimensional wood pyrolysis model. Uncertainty in the modeling parameters of the transport processes is propagated to the simulation results of the pyrolysis model. The model predictions are compared with several detailed experimental measurements for pyrolysis of wood particles. The results show that the uncertainty in the model predictions account for some of the discrepancies with the experimental measurements, especially for the particle temperature profiles and the gas phase species production rates. Experimental targets are identified whose predictions cannot be improved by an accurate knowledge of the transport model parameters and require further

improvements in the chemical kinetics model. The use of a systematic optimization technique is also demonstrated to choose the optimal values of uncertain model parameters.

3.2 Introduction

Modeling and simulation tools provide a flexible and affordable framework to investigate the controlling chemical and physical processes of biomass pyrolysis, with the potential to play a determining role in the development and deployment of this conversion technique. Although modeling of biomass pyrolysis has come a long way, starting from one-component kinetic models [161] to a recently developed mechanistic model for cellulose pyrolysis [178, 197], a comprehensive understanding of biomass pyrolysis is far from reality, and a strong need for modeling efforts has been recognized in the literature [67]. Several challenges hinder the development of accurate models for biomass pyrolysis, a major one being the poor knowledge of the complex microscale morphological changes, such as shrinkage and changing internal particle structure, that take place inside a biomass particle during the pyrolysis process [88]. These morphological changes significantly affect biomass properties, such as thermal conductivity and heat capacity, and thus the transport of heat and mass [31, 134]. Therefore, detailed particle level modeling of biomass pyrolysis requires models that can accurately capture the dependence of the biomass properties on the internal morphological changes [109]. However, such models do not yet exist because of the inherent complexity of the problem [189].

Particle-scale models of biomass pyrolysis mathematically represent the

chemical kinetics of the conversion process coupled with several intra-particle transport processes, such as the transport of mass and energy. The transport sub-model requires biomass properties, such as thermal conductivity and specific heat capacity, as the input parameters. However, the variability in biomass feedstock and the scarcity of detailed data for biomass properties has prompted the usage of widely varying values for these properties in the literature [182]. Many times the biomass properties are tuned in an *ad-hoc* manner while validating the pyrolysis model [33]. A few studies, in the literature, have focused on relating the macroscopic properties of biomass to its microscopic structure. For instance, Eitelberger and Hofstetter [50] estimate the thermal conductivity of biomass close to room temperature using the biomass morphology and the thermal conductivities of its major constituents. However, the input parameters in their study are uncertain parameters and the effect of any morphological change is not included, which becomes important during biomass pyrolysis. For these reasons, the validation of biomass pyrolysis models has been identified as one of the "top ten" fundamental challenges of biomass pyrolysis by Mettler et al. [109]. Considering the large uncertainties in the values of several biomass properties and their influence on biomass pyrolysis, uncertainty quantification (UQ) becomes an integral part of the model validation process. When the uncertainty in the model predictions is known, a meaningful comparison can be made with the experimental measurements, revealing specific parts of the model where further improvements should be sought.

Many sources of uncertainty can exist in a model, such as boundary conditions, modeling assumptions, or model parameters [115]. The quantification of every single source of uncertainty present in a model is impractical, and generally, uncertainty in a few model parameters only is quantified and propagated

to the model predictions [114, 60, 156]. In the case of biomass pyrolysis, although a detailed three-dimensional model has recently been developed [61], a one-dimensional (1D) transport model coupled with a lumped chemical kinetic scheme is most commonly used to simulate particle-scale biomass pyrolysis experiments [133, 33, 3, 4], and different sources of uncertainty can be present in these 1D particle-scale models. In this study, we focus only on the uncertainty in the transport model parameters of woody biomass and neglect the other sources of uncertainty. The goal of this work is to provide an in-depth analysis of the validity of a 1D pyrolysis model against experiments considering the uncertainty in the transport model parameters and to find the optimal values of these uncertain parameters using a systematic optimization technique. To achieve this goal, we develop a 1D particle-scale pyrolysis model, quantify the uncertainty in the transport model parameters and propagate it to the model predictions.

Several UQ studies exist in the literature for different types of problems, such as combustion [114], fluidized bed [60], and coke gasifier [156], yet, in our knowledge, no UQ study has been performed for biomass pyrolysis. For a detailed overview of various UQ methods, readers are referred to the review articles by Najm [115] and Wang and Sheen [179]. In this work, a non-intrusive UQ approach [114, 60, 156] is employed, where ensemble evaluations of the model are performed to propagate the uncertainty through the model. This brute force approach requires thousands of simulations to get the statistics of the output and would become computationally intractable if the original model is used for this purpose. To address this issue, the solution mapping (SM) method of Frenklach [58] is used to construct a response surface to estimate the predictions of the pyrolysis model in a computationally inexpensive manner. The SM method [58] is also used in the systematic optimization of the uncertain model

parameters. It is important to note that while we focus here on transport parameters only, the methodology employed in this work can be applied in the same way to other modeling aspects related to industrially-relevant biomass feedstock, such as shape and size of biomass particles.

The remainder of this paper is organized as follows. The Particle Model Description section describes the governing equations and boundary conditions of the one-dimensional particle-scale model for biomass pyrolysis used in this work. An overview of the methodology employed here to perform the UQ and optimization studies is provided in the Methodology section. The Results and Discussion section first presents two verification cases for the pyrolysis model, and then describes the results of the UQ and optimization studies. A detailed analysis of the results and their possible implications are also provided in this section.

3.3 Particle model description

A spherically symmetric 1D intra-particle model, referred to as $\mathcal{M}_{\mathcal{P}}$, is developed for the simulation of wood pyrolysis based on the work of Park et al. [133]. Here, both solid and gas phases are treated as a mixture of interpenetrating continua within the particle. During pyrolysis, the particle is heated through convection and/or radiation, releasing several gaseous species and gets converted into residual char. $\mathcal{M}_{\mathcal{P}}$ describes the conservation of mass in the gas and solid phases, the total energy of gas and solid phases, and individual gaseous species accompanying the pyrolysis of the particle. The lumped chemical kinetic scheme of the CRECK modeling group [33] is used to model the pyroly-

sis reactions. This kinetic scheme involves n_s=12 solid species, 7 trapped gas species slowly releasing from the solid matrix, and n_g=20 gaseous products. The initial composition of wood is represented by a combination of cellulose, hemicellulose, and three types of lignin. A brief description of the governing equations and the boundary conditions of $\mathcal{M}_{\mathcal{P}}$ are provided below.

The rate of change of mass per unit volume of the i^{th} solid component of the particle is given by

$$\frac{d\rho_{s,i}}{dt} = \omega_{s,i}\,, \tag{3.1}$$

where $\rho_{s,i}$ is the apparent density (including pore volume) and $\omega_{s,i}$ is the reaction source term for the i^{th} solid component. Here, the particle shrinkage is assumed to be negligible [132], making the particle radius constant and equal to the initial radius r_0. Mass conservation for the gas phase is given by

$$\frac{\partial(\varepsilon\rho)}{\partial t} + \frac{1}{r^2}\frac{\partial\left(r^2\rho U\right)}{\partial r} = \sum_{j=1}^{n_g}\omega_j\,, \tag{3.2}$$

where ρ is the gas density, U is the superficial gas velocity, and ω_j is the source term for the j^{th} gas phase species. ε is the porosity, calculated by

$$\varepsilon = 1 - \frac{\rho_s}{\rho_s^0}(1-\varepsilon_0)\,. \tag{3.3}$$

In the equation above, ρ_s and ρ_s^0 are the instantaneous and initial solid masses per unit volume, respectively, and ε_0 is the initial particle porosity. A low Mach number assumption is made to remove the effect of pressure variations due to the gas flow on ρ. Assuming that the ideal gas law applies, ρ is calculated as:

$$\rho = \frac{PM}{RT}\,. \tag{3.4}$$

Here, P is the thermodynamic pressure, M is the molar mass of the gas phase mixture and R is the ideal gas constant. Mass conservation for the j^{th} gas phase

species is given by

$$\frac{\partial(\varepsilon\rho y_j)}{\partial t} + \frac{1}{r^2}\frac{\partial(r^2 U\rho y_j)}{\partial r} = \frac{1}{r^2}\frac{\partial}{\partial r}\left(r^2 D\frac{\partial\rho y_j}{\partial r}\right) + \omega_j\,, \tag{3.5}$$

where y_j is the mass fraction of the j^{th} gas species, and D is the mass diffusivity, assumed to be constant for all species. Assuming a local thermodynamic equilibrium between gas and solid phases, the energy conservation equation can be written as:

$$\left(\sum_{i=1}^{n_s}\rho_{s,i}C_i + \varepsilon\sum_{j=1}^{n_g}\rho_j C_{p,j}\right)\frac{\partial T}{\partial t} + \left(\sum_{j=1}^{n_g}\rho_j C_{p,j}\right)U\frac{\partial T}{\partial r} = \frac{1}{r^2}\frac{\partial}{\partial r}\left(r^2\lambda\frac{\partial T}{\partial r}\right) + \sum_{k=1}^{n_r}\Omega_k\Delta h_k\,, \tag{3.6}$$

where T is the particle temperature, C_i is the specific heat capacity of the i^{th} solid component, and $C_{p,j}$ is the constant pressure specific heat capacity of the j^{th} gas phase species. Specific heat capacity of the gas phase $C_{p,g}$ is calculated as $\sum_{j=1}^{n_g} y_j C_{p,j}$. The last term on the right hand side is the heat source term, where n_r is the total number of reactions, and Ω_k and Δh_k are the reaction rate and heat of reaction, respectively, of the k^{th} reaction. C for char is C_c and C for the rest of the solid components is assumed to be equal to the specific heat capacity of wood, C_w. Thermal conductivity for char is λ_c, and for the rest of the solid components, is assumed to be equal to the thermal conductivity of wood, λ_w. Both λ_w and λ_c are taken as the average value of the three directions (radial, tangential, and grain) of the particle. λ is the effective thermal conductivity, calculated as the weighted sum of the thermal conductivities of wood λ_w, char λ_c, and gases λ_g, and the radiative heat transfer through pores λ_{rad} [133, 47].

$$\lambda = (1-\gamma)\lambda_w + \gamma\lambda_c + \varepsilon\lambda_g + \lambda_{\text{rad}}\,, \tag{3.7}$$

where λ_g is the mixture-averaged thermal conductivity of the gas phase, calculated as [104]:

$$\lambda_g = \frac{1}{2}\left(\sum_{j=1}^{n_g} X_j\lambda_{g,j} + \frac{1}{\sum_{j=1}^{n_g} X_j/\lambda_{g,j}}\right). \tag{3.8}$$

Here, $\lambda_{g,j}$ and X_j are the thermal conductivity and the mole fraction of the j^{th} gaseous species, respectively. λ_{rad} is the contribution to the particle thermal conductivity due to the intra-particle radiation and is modeled following Blasi [47] as:

$$\lambda_{\text{rad}} = \frac{13.5\sigma T^3 d}{e}\,, \tag{3.9}$$

where σ is the Stefan–Boltzmann constant, e is the emissivity, and d is the effective pore size, calculated as:

$$d = (1-\gamma)d_w + \gamma d_c\,, \tag{3.10}$$

with d_w and d_c being the pore sizes of wood and char, respectively. γ is the degree of pyrolysis defined as:

$$\gamma = 1 - \frac{\sum_{i=1}^{n_s}\rho_{s,i} - \rho_c}{\rho_s^0}\,, \tag{3.11}$$

where ρ_c is the density of char.

At the particle boundary surface ($r = r_0$), species gradients are imposed by the external convective mass transfer, and the temperature gradient is imposed by the external convective and radiative heat transfer, such that:

$$D\left.\frac{\partial \rho y_j}{\partial r}\right|_{r=r_0} = \kappa(\rho y_{j,\infty} - \rho y_{j,r=r_0}) \tag{3.12}$$

$$\lambda\left.\frac{\partial T}{\partial r}\right|_{r=r_0} = h(T_\infty - T_{r=r_0}) + \sigma e_s(T_{\text{reac}}^4 - T_{r=r_0}^4), \tag{3.13}$$

where e_s is the surface emissivity, and κ and h are the convective mass and heat transfer coefficients, respectively. $y_{j,r=r_0}$ is the mass fraction of the j^{th} gas phase species at the particle surface, $y_{j,\infty}$ is the ambient mass fraction of the j^{th} gas species, $T_{r=r_0}$ is the particle surface temperature, T_∞ is the ambient gas temperature, and T_{reac} is the wall temperature of the reactor where particle is heated. At the particle center (r=0), a zero-gradient condition is imposed due to symmetry:

$$\left.\frac{\partial T}{\partial r}\right|_{r=0} = 0 \tag{3.14}$$

$$\left.\frac{\partial \rho y_j}{\partial r}\right|_{r=0} = 0\,. \tag{3.15}$$

The resulting set of coupled non-linear partial differential equations (PDEs) is discretized using finite differences: a central difference scheme is used for the diffusion terms, while an upwind scheme is used for the convective terms. A backward Euler implicit scheme is employed to discretize the temporal terms. At each time step, all the discretized equations are solved iteratively until a converged solution is obtained. The verification of $\mathcal{M}_{\mathcal{P}}$ is provided in the Results and Discussion section.

3.4 Methodology

This section describes the methodology utilized to achieve our objectives of propagating the uncertainty in the transport model parameters to the predictions of $\mathcal{M}_{\mathcal{P}}$ and finding the optimal values of the uncertain model parameters.

The first step is to select a set of model parameters that is going to be used in the UQ study. To reduce the computational cost of performing the uncertainty analysis, only the transport model parameters contributing most to the uncertainty are included. To this end, a sensitivity analysis is performed to identify the most sensitive parameters, and the uncertainty in those sensitive parameters is quantified in the form of probability distribution functions (PDFs) using their values employed in the literature.

Since evaluating $\mathcal{M}_{\mathcal{P}}$ for multiple combinations of the uncertain model parameters is computationally expensive, the solution mapping (SM) method [58] is used to map the solution of $\mathcal{M}_{\mathcal{P}}$ to a multi-dimensional polynomial, known

as response surface, allowing for a significant reduction in the cost of obtaining the output of $\mathcal{M}_{\mathcal{P}}$. In the SM method, each model parameter is normalized as

$$x_i = \frac{\ln(\mathcal{P}_i/\mathcal{P}_{i,0})}{\ln f_i}\,, \tag{3.16}$$

where $\mathcal{P}_i$ is the i^{th} uncertain model parameter and $\mathcal{P}_{i,0}$, its nominal value. The normalization bounds x_i between -1 and 1 with its nominal value equal to 0. f_i is the uncertainty factor associated with $\mathcal{P}_i$, such that

$$\mathcal{P}_{i,0}/f_i \leq \mathcal{P}_i \leq \mathcal{P}_{i,0} f_i\,. \tag{3.17}$$

For combustion problems, a 2^{nd} order polynomial is usually adequate to be a response surface [59]. Considering the similarity between combustion and biomass pyrolysis in terms of the underlying physical and chemical processes, a 2^{nd} order polynomial is used here as well, and the response surface $\eta(\mathbf{x})$ is assumed to be of the form:

$$\eta(\mathbf{x}) = \eta_0 + \sum_{i=1}^{N} a_i x_i + \sum_{i=1}^{N}\sum_{j\geq i}^{N} b_{ij} x_i x_j\,, \tag{3.18}$$

where N is the number of uncertain model parameters, and η_0 is the model prediction at the nominal values of the uncertain model parameters. a_i and b_{ij} are the constant polynomial coefficients, and are determined by conducting regression analysis of the output of several simulations of $\mathcal{M}_{\mathcal{P}}$, in which the values of uncertain model parameters are determined using a factorial design [14]. It should be noted that a separate $\eta(\mathbf{x})$ needs to be created for each quantity of interest, such as particle temperature and species mass fraction, referred to as targets in this study.

To propagate the uncertainty in the model parameters to the predictions of $\mathcal{M}_{\mathcal{P}}$, evaluations of the response surface $\eta(\mathbf{x})$ are performed by sampling the

PDFs of the normalized model parameters. Using the outputs of the response surface, a PDF is constructed for the predictions of a target.

The optimal values of the uncertain model parameters, which will be denoted by $\mathbf{x}^*$, are obtained by minimizing the least-squares difference between the experimental measurements η_i^{obs} and the model predictions $\eta_i(\mathbf{x})$ of the n targets of interest. This is done by minimizing the following objective function:

$$\mathbf{\Phi}(\mathbf{x}^*) = \min_{\mathbf{x}} \sum_{i=1}^{n} \left(\frac{\eta_i(\mathbf{x}) - \eta_i^{\text{obs}}}{\eta_i^{\text{obs}}} \right)^2 , \tag{3.19}$$

subject to the constraint that $-1 \leq x_i \leq 1$. In general, the standard deviation σ_i^{obs} in the experimental measurements is preferred to normalize the differences between the measurements and the predictions, as it includes the inherent uncertainty in the experimental measurements and hence, can provide better weighting factors for different targets. In this study, σ_i^{obs} for all the experimental data used is not available, therefore, in Eq. 3.19, the differences between the measurements and the predictions are normalized by η_i^{obs}.

3.5 Results and discussion

The methodology described in the previous section is now employed to quantify the uncertainties in the prediction of model $\mathcal{M}_{\mathcal{P}}$ and provide a more comprehensive and insightful comparison of those predictions with experimental data. As mentioned above, we focus here on the influence of the uncertainty in the values of the transport model parameters only.

The results are presented in three subsections. The first subsection provides two verification cases for $\mathcal{M}_{\mathcal{P}}$ by comparing its predictions with the analytical

solution of the 1D transient heat conduction in a sphere and the results of a similar 1D model implemented in COMSOL Multiphysics [79] by Corbetta et al. [33]. In the second subsection, the results of the UQ study are provided and analyzed in the context of a comparison with experimental data. In the third subsection, optimal values for the uncertain model parameters are evaluated and the predictions of the resulting optimized model $\mathcal{M}_{\mathcal{P}}^{*}$ and unoptimized/base model $\mathcal{M}_{\mathcal{P}}$ are compared.

In this work, two experimental studies are used for the UQ and optimization studies : 1) the pyrolysis of maple wood spheres with diameter d_p=2.54 cm by Park et al. [133] at six reactor temperatures T_{reac}: 638 K, 688 K, 736 K, 783 K, 831 K, and 879 K, which will be referred to as experimental set $\mathscr{E}_{\text{I}}$, and 2) the pyrolysis of poplar wood spheres with d_p=2.54 cm by Bennadji et al. [10] at T_{reac}=641 K, 700 K, and 743 K, referred to as experimental set $\mathscr{E}_{\text{II}}$. As both the experimental studies were performed at low reactor temperatures, secondary gas phase reactions are assumed to be negligible and not considered in the simulations. In $\mathscr{E}_{\text{I}}$, measurements include the evolution of temperature at different locations inside the particle and solid mass fraction, and the final lumped product yields. In $\mathscr{E}_{\text{II}}$, the instantaneous production rates and the yields of CO, CO_2, CH_4, HCHO, HCOOH, and CH_3COOH are measured. Table 3.1 provides the targets selected from $\mathscr{E}_{\text{I}}$ and $\mathscr{E}_{\text{II}}$ for both the UQ and the optimization studies. In this table, t_{dev} is defined as the time at which the rate of change of solid mass fraction becomes very small (a cutoff value of 10^{-4} is used in the simulations). The lumped product yield of gas, $Y_{\text{gas}}^{\text{lump}}$, is defined as the sum of the yields of all the permanent gaseous species, such as CO and CH_4, included in $\mathcal{M}_{\mathcal{P}}$, whereas the lumped product yield of tar, $Y_{\text{tar}}^{\text{lump}}$, is taken as the sum of the yields of all the species that are liquid at room temperature, such as levoglucosan.

Table 3.1: Selected targets from $\mathscr{E}_{\mathrm{I}}$ and $\mathscr{E}_{\mathrm{II}}$ for the UQ and optimization studies.

Targets for $\mathscr{E}_{\mathrm{I}}$	Targets for $\mathscr{E}_{\mathrm{II}}$
1) Peak temperature at the particle center, T_{peak}	1) Peak production rate of species, $\mathscr{P}$
2) Time of peak temperature at the particle center, $t_{T_{\mathrm{peak}}}$	2) Time of peak production rate of species, $t_{\mathscr{P}}$
3) Devolatilization time, t_{dev}	3) Yield of species, $\mathbf{Y}$
4) Lumped product yields, $\mathbf{Y}^{\mathrm{lump}}$: $Y_{\mathrm{gas}}^{\mathrm{lump}}$, $Y_{\mathrm{tar}}^{\mathrm{lump}}$, and Solid residue (SR)	

3.5.1 Verification of the particle model

For the first verification case, the predictions of $\mathcal{M}_{\mathscr{P}}$ are compared with the analytical solution of the 1D transient heat conduction in a sphere with constant properties. For the comparison, a spherical particle with r_0=5 mm, density ρ_p=630 kg/m^3, specific heat capacity C=1800 J/kg·K, initial particle temperature T_0=300 K, and ambient temperature T_∞=773 K is considered. The analytical solution for the temperature evolution inside the sphere is given by [11]

$$\theta = \sum_{i=1}^{\infty} C_i \exp(-\zeta_i^2 Fo) \frac{\sin(\zeta_i r^*)}{\zeta_i r^*} ,$$
$$C_i = \frac{4\left[\sin(\zeta_i) - \zeta_i \cos(\zeta_i)\right]}{2\zeta_i - \sin(2\zeta_i)} , \; 1 - \zeta_i \cot(\zeta_i) = Bi . \tag{3.20}$$

Here, $\theta = \frac{T-T_\infty}{T_0-T_\infty}$ is the non-dimensional temperature, and r^* is the radial location normalized by r_0: $r^* = r/r^0$. Bi is the Biot number, defined as $Bi = hr_0/\lambda$, Fo is the Fourier number, equivalent to a dimensionless time and defined as $\alpha t/l^2$, where t is the time, α is the thermal diffusivity, and l is the characteristic length defined as $r_0/2$. For Fo¿0.2, the series solution in Eq. 3.20 can be approximated by its first term: [11]

$$\theta = C_1 \exp(-\zeta_1^2 Fo)\frac{\sin(\zeta_1 r^*)}{\zeta_1 r^*}\,. \tag{3.21}$$

Using the values of ζ_1 and C_1 taken from Bergman et al. [11], the analytical solution for the temperature evolution at the particle center is fully determined. Figure 3.1 shows the comparison of the analytical solution with the predictions of $\mathcal{M}_\mathcal{P}$ for a wide range of Bi. As expected, the numerical solution of $\mathcal{M}_\mathcal{P}$ is in excellent agreement with the analytical solution.

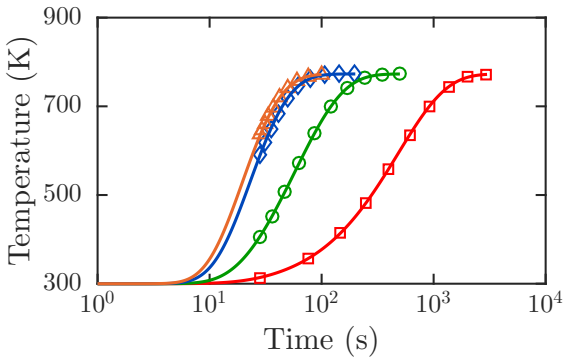

Figure 3.1: Temperature evolution for 1D transient heat conduction in a solid sphere. Comparison between the predictions of $\mathcal{M}_\mathcal{P}$ (lines) and the analytical expression (symbols) for the center temperature. Different symbols indicate different Bi (red square: 10^{-1}, green circle: 10^0, blue diamond: 10^1, orange triangle: 10^2).

In the second verification case, we compare the predictions of $\mathcal{M}_\mathcal{P}$ with those of a similar 1D particle model implemented in COMSOL Multiphysics [79] by Corbetta et al. [33] to simulate the pyrolysis of the maple wood spheres used in

the $\mathscr{E}_{\mathrm{I}}$ experimental set. We use $\mathcal{M}_{\mathcal{P}}$ to simulate the same experiments with the values of model parameters taken from Corbetta et al. [33]. Figure 3.2 shows the comparison between the predictions of $\mathcal{M}_{\mathcal{P}}$ and those of the COMSOL simulation of Corbetta et al. [33], along with the measurements from $\mathscr{E}_{\mathrm{I}}$. The excellent agreement between the predictions of $\mathcal{M}_{\mathcal{P}}$ and the COMSOL simulations [33] further verifies the numerical implementation of $\mathcal{M}_{\mathcal{P}}$.

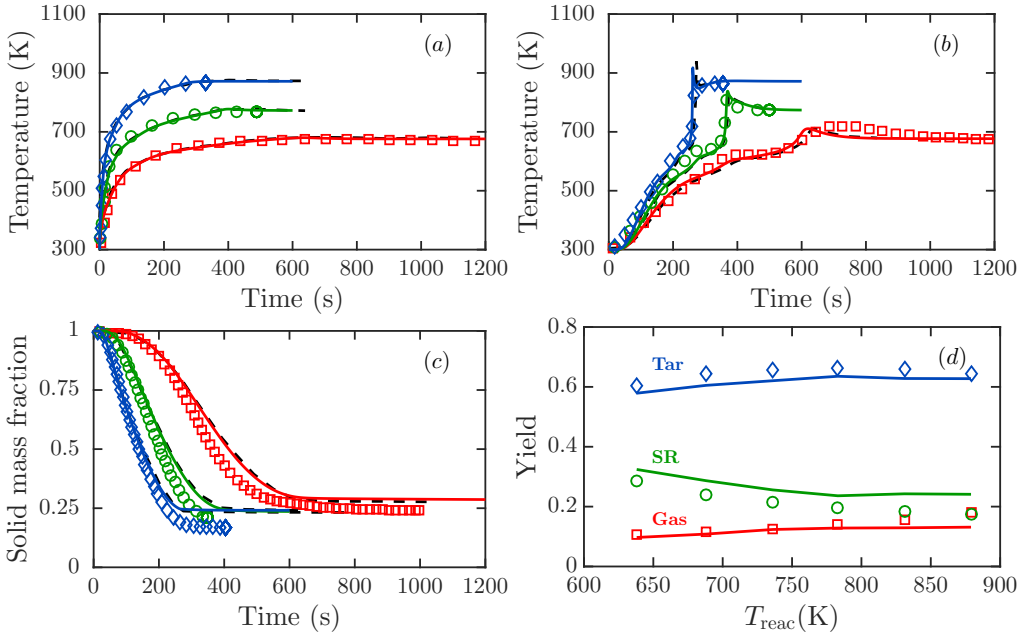

Figure 3.2: Comparison between the predictions of $\mathcal{M}_{\mathcal{P}}$ (solid lines) and COMSOL simulations results (Corbetta et al. [33], dashed lines), along with the measurements from $\mathscr{E}_{\mathrm{I}}$ (symbols). (a), (b), and (c) show the evolution as a function of time of the particle surface temperature, the particle center temperature, and solid mass fraction, respectively. Different symbols indicate different reactor temperatures T_{reac} (red square: 688K, green circle: 783K, and blue diamond: 879K). (d) shows the lumped product yields as a function of T_{reac}.

3.5.2 Uncertainty quantification

Uncertain model parameters

Performing the uncertainty analysis for a large number of model parameters is computationally intractable. For this reason, we only consider those transport model parameters that 1) show large sensitivity to the model predictions, and 2) have large uncertainty in their values. To identify the most sensitive model parameters, a sensitivity analysis of $\mathcal{M}_{\mathcal{P}}$ is performed for the experimental conditions of $\mathscr{E}_{\mathrm{I}}$ at the lowest (T_{reac}=638 K) and the highest (T_{reac}=831 K) reactor temperatures. The sensitivity coefficient associated with the i^{th} model parameter $\mathcal{P}_i$, $\mathcal{S}_{i,j}$, is defined as

$$\mathcal{S}_{i,j} = \frac{\mathcal{P}_{i,0}}{\mathcal{P}_i - \mathcal{P}_{i,0}} \frac{\mathcal{G}_j - \mathcal{G}_{j,0}}{\mathcal{G}_{j,0}}, \tag{3.22}$$

where $\mathcal{P}_{i,0}$ is the nominal value of the model parameter and $\mathcal{P}_i$ is obtained by multiplying $\mathcal{P}_{i,0}$ with a factor χ. $\mathcal{G}_j$ and $\mathcal{G}_{j,0}$ are the model predictions of the j^{th} target corresponding to $\mathcal{P}_i$ and $\mathcal{P}_{i,0}$, respectively. We choose χ=2 to calculate $\mathcal{S}_{i,j}$. Figure 3.3 plots the coefficients $\mathcal{S}_{i,j}$ for the targets: T_{peak}, t_{dev}, and $\mathbf{Y}^{\mathrm{lump}}$. We observe that at T_{reac}=879 K, $\mathcal{M}_{\mathcal{P}}$ is sensitive to a larger number of model parameters and exhibits higher sensitivity compared to T_{reac}=638 K. For the purpose of this study, the model parameters with $\mathcal{S}_{i,j} > 0.05$ at both temperatures for at least one target are selected. Six model parameters are found to satisfy this criterion: λ_w, λ_c, C_w, C_c, λ_g, and $C_{p,g}$. Out of these six sensitive parameters, λ_g and $C_{p,g}$ are known with relatively low uncertainty as the properties of the gas species involved in our case have typically been studied, extensively. The remaining four sensitive model parameters correspond to the thermal properties of biomass. Several sensitivity studies [49, 165] in the literature have also identified the thermal properties to be the most sensitive parameters in a particle-level pyrolysis

model, and these properties also show high variability in their reported values in the literature [49, 165, 73, 74]. Therefore, we choose $\mathcal{H}$: $\{\lambda_w, \lambda_c, C_w, C_c\}$ as the set of uncertain model parameters for the UQ study.

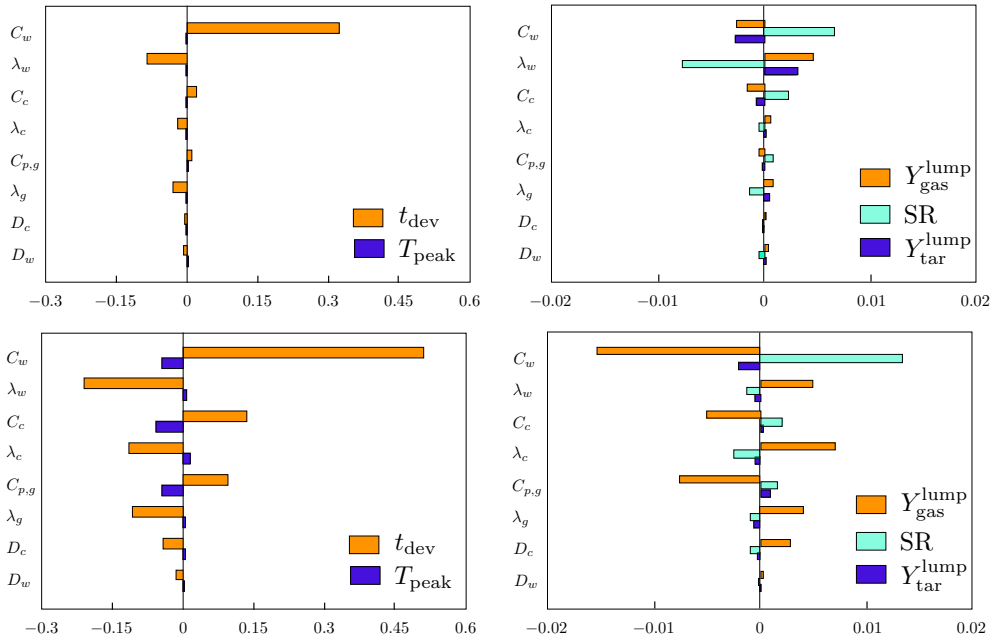

Figure 3.3: Sensitivity analysis of $\mathcal{M}_{\mathcal{P}}$ for $\mathcal{E}_{\text{I}}$. Top row: T_{reac}=638 K and Bottom row: T_{reac}=879 K.

Uncertainty characterization in selected model parameters

In the literature, due to the lack of the detailed measurements of thermal conductivities and heat capacities for various biomass samples, modelers commonly use the values of these properties measured at low temperatures available for other biomass samples [102] or tune these properties to obtain a better match with the experiments [33]. Therefore, we used various expressions and values of λ_w, λ_c, C_w, and C_c reported in the literature (listed in Table 3.2) as a way to estimate the uncertainty in these properties. In Table 3.2, $\lambda_{w,\parallel}$ and $\lambda_{w,\perp}$ are the

wood thermal conductivity parallel and perpendicular to the grain direction, respectively. In the literature, an average value of wood thermal conductivity λ_w is obtained by a linear combination of $\lambda_{w,\parallel}$ and $\lambda_{w,\perp}$ using some empirical weighting coefficients [61]. Since we want to estimate a broad range of values of λ_w used in the literature, $\lambda_{w,\parallel}$ and $\lambda_{w,\perp}$ are simply considered to be the possible values of λ_w. In general, C_w and C_c are expressed as functions of temperature, whereas constant values are used for λ_w and λ_c, even though both λ_w and λ_c are known to increase with temperature [73, 66].

The uncertainty in the value of a model parameter is represented by a probability density function (PDF), with normal and uniform distributions being the two limiting cases [162]. If the values of a parameter are measured a statistically significant number of times such that a meaningful standard deviation can be defined, then the parameter values should be assumed to have a normal distribution. On the other hand, if only a few measurements are available to provide an estimate of lower and upper bounds, then the parameter should be assumed to have a uniform distribution [162]. In this work, the latter is true for the parameters in $\mathcal{H}$, and their values are therefore assumed to be uniformly distributed.

For uniformly distributed model parameter values, $\mathcal{P}_{i,0}$ and f_i can be estimated from Eq. 3.17 using their minima and maxima from Table 3.2:

$$f_i = \sqrt{\frac{\mathcal{P}_{i,\max}}{\mathcal{P}_{i,\min}}} \text{ and } \mathcal{P}_{i,0} = \sqrt{\mathcal{P}_{i,\max}\mathcal{P}_{i,\min}}\,. \tag{3.23}$$

Equation 3.23 provides single values of f_i and $\mathcal{P}_{i,0}$ for λ_w and λ_c, whereas for C_w and C_c, f_i and $\mathcal{P}_{i,0}$ vary with temperature. We found that the nominal values of C_w and C_c can be closely predicted by the expressions of Gupta et al. [73] and Fredlund et al. [57], respectively. We use the maxima of f_i for both C_w and

Table 3.2: Values and expressions used in the literature for C_w, C_c, λ_w, and λ_c.

Specific heat capacity of wood C_w (kJ/kg·K)	
2.3	Ref. [36, 111, 91, 187]
$2.3 - 1.15\exp(-0.0055T)$	Ref. [13]
$-0.0912 + 0.0044T$	Ref. [83]
$1.2 + 2.45 \times 10^{-3}(T - 273)$	Ref. [75]
$0.2316 + 3.69 \times 10^{-3}T$	Ref. [73]
$1.5 + 10^{-3}T$	Ref. [71, 133, 33, 61]
$0.1031 + 3.867 \times 10^{-3}T$	Ref. [150, 164]
$0.112 + 4.85 \times 10^{-3}T$	Ref. [84, 8]
Specific heat capacity of char C_c (kJ/kg·K)	
1.1	Ref. [36, 111, 91, 187]
$1.39 + 3.6 \times 10^{-4}T$	Ref. [167, 150]
$1.430 + 3.55 \times 10^{-4}T - 7.32 \times 10^{4}T^{-2}$	Ref. [57, 89, 13]
$1.0032 + 2.09 \times 10^{-3}(T - 273)$	Ref. [84, 8]
$0.42 + 2.09 \times 10^{-3}T + 6.85 \times 10^{-3}T^2$	Ref. [71]
$-0.79528 + 5.98 \times 10^{-3}T - 3.8 \times 10^{-6}T^2$	Ref. [73]
Thermal conductivity of wood λ_w (W/m·K)	
0.1256	Ref. [148, 111]
0.11	Ref. [92, 102]
$\lambda_{w,\parallel} = 0.73, \lambda_{w,\perp} = 0.52$	Ref. [172, 13]
$0.13 + 3 \times 10^{-4}(T - 273)$	Ref. [84, 8]
$\lambda_{w,\perp} = 0.0986$	Ref. [73]
$\lambda_{w,\parallel} = 0.156 - 0.278, \lambda_{w,rad} = 0.112 - 0.176, \lambda_{w,tan} = 0.074 - 0.133$	Ref. [94]
$\lambda_{w,\parallel} = 0.158 - 0.419, \lambda_{w,\perp} = 0.081 - 0.209$	Ref. [71]
$\lambda_{w,\parallel} = 0.291 - 0.323, \lambda_{w,\perp} = 0.177 - 0.214$	Ref. [168]
$\lambda_{w,\parallel} = 0.2 - 0.4, \lambda_{w,\perp} = 0.1 - 0.25$	Ref. [172]
Thermal conductivity of char λ_c (W/m·K)	
0.052	Ref. [150]
0.0837	Ref. [148, 111]
0.071	Ref. [92, 102]
0.1405	Ref. [33]
$0.08 - 10^{-4}(T - 273)$	Ref. [84, 8]

C_c as their respective uncertainty factors. Figure 3.4 shows the values of C_w and C_c obtained from the various expressions provided in Table 3.2 along with the nominal values, $\mathcal{P}_{i,0}$, and the lower ($\mathcal{P}_{i,0}/f_i$) and upper ($\mathcal{P}_{i,0}f_i$) limits of their

distributions. Table 3.3 provides $\mathcal{P}_{i,0}$ and f_i estimated for all the parameters in $\mathcal{H}$.

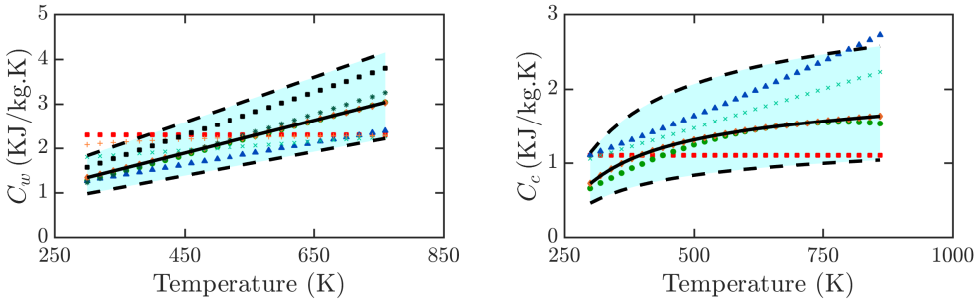

Figure 3.4: C_w and C_c from various sources. Different symbols correspond to expressions for C_w and C_c provided in Table 3.2. The nominal values $\mathcal{P}_{i,0}$ are shown by solid lines, while the minimum $\mathcal{P}_{i,\min}$ and maximum $\mathcal{P}_{i,\max}$ values are shown by dashed lines.

Table 3.3: Uncertain model parameters with their nominal values and uncertainty factors.

Parameter in $\mathcal{H}$	Units	Nominal value, $\mathcal{P}_{i,0}$	Uncertainty factor, f_i
λ_w	W/m·K	0.232	3.1
λ_c	W/m·K	0.085	1.6
C_w	J/kg·K	$231.6 + 3.69T$	1.8
C_c	J/kg·K	$1430 + 0.355T - 7.32\times10^7 T^{-2}$	1.4

Response surface

A response surface $\eta(\mathbf{x})$ is created for each experimental target of $\mathscr{E}_{\mathrm{I}}$ and $\mathscr{E}_{\mathrm{II}}$ using the full 2^N factorial design, requiring $2^N + 2N + 1$ simulations of $\mathcal{M}_{\mathcal{P}}$ [14]. In this work, N=4 (C_w, C_c, λ_w, and λ_c) and thus 25 computational runs of $\mathcal{M}_{\mathcal{P}}$ are required to create the response surfaces for all the targets of an experiment

at a single reactor temperature. To check the adequacy of the created response surfaces, their predictions for each target are compared with those of $\mathcal{M}_{\mathcal{P}}$ by sampling from the PDFs of the parameters in $\mathcal{H}$. Correlation coefficients are calculated between the predictions of $\eta(\mathbf{x})$ and $\mathcal{M}_{\mathcal{P}}$, and are found to be greater than 0.99 for every target, confirming that the response surfaces provide adequate estimates for the predictions of $\mathcal{M}_{\mathcal{P}}$. Figure 3.5 shows the comparison between the predictions of $\eta(\mathbf{x})$ and $\mathcal{M}_{\mathcal{P}}$ for t_{dev}, T_{peak}, $t_{\mathscr{P}_{\text{CO}}}$, and $\mathscr{P}_{\text{CO}}$.

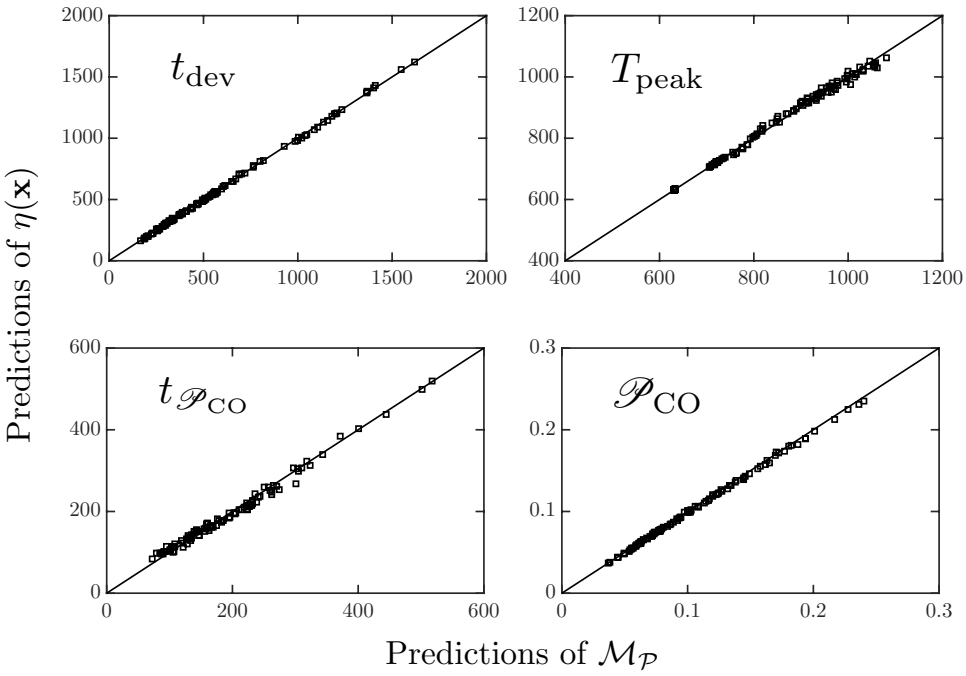

Figure 3.5: Comparison of response surface $\eta(\mathbf{x})$ predictions vs direct calculations using $\mathcal{M}_{\mathcal{P}}$.

Uncertainty in the model predictions

Response surfaces $\eta(\mathbf{x})$ developed in the previous subsection are evaluated for $\mathbf{x}$ sampled from the PDFs of the parameters in $\mathcal{H}$ to propagate the input uncer-

tainty through $\mathcal{M}_{\mathscr{P}}$. For this purpose, 100,000 samples are used for each target, and are found to be sufficient to get converged statistics. The resulting model outputs are used to construct the PDF and cumulative density function (CDF) of each target's predictions. To quantify the uncertainty in the model predictions, we calculate the mean, and the lower l_b and upper u_b bounds of the model predictions of a target containing 95% area of the PDF. Consequently, $F(l_b) = 0.025$ and $F(u_b) = 0.975$, where F is the CDF of the target's predictions. The predictions of $\mathcal{M}_{\mathscr{P}}$ including the uncertainty are compared with the experimental measurements for the targets of $\mathscr{E}_{\mathrm{I}}$ and $\mathscr{E}_{\mathrm{II}}$ as shown in Figs. 3.6–3.9. Figure 3.6 shows the comparison for the targets of $\mathscr{E}_{\mathrm{I}}$: $t_{T_{\mathrm{peak}}}$, T_{peak}, t_{dev}, and $\mathbf{Y}^{\mathrm{lump}}$, whereas Figs. 3.8, 3.7, and 3.9 show the comparison for the targets of $\mathscr{E}_{\mathrm{II}}$: $\mathscr{P}$, $t_{\mathscr{P}}$, and $\mathbf{Y}$, respectively. The error bars for the experimental measurements are added to the figures whenever available.

Figures 3.6–3.9 show that significant uncertainty exists in the model predictions of all the targets except for $\mathbf{Y}^{\mathrm{lump}}$ and $\mathbf{Y}$. This is expected, since the sensitivity analysis predicted small sensitivity of the product yields toward the transport model parameters (Fig. 3.3). We also observe that the uncertainty bounds are proportional to the mean values for most of the targets, however, a non-linear dependence is observed for T_{peak} and $t_{\mathscr{P}}$ as shown in Fig. 3.6(b) and Fig. 3.8, respectively. This observation emphasizes the fact that the model output can have a non-linear dependence on the model parameters, which may not be captured by a simple sensitivity analysis.

Figure 3.6 shows that most of the discrepancy between the experimental measurements and the model predictions of $t_{T_{\mathrm{peak}}}$ and t_{dev} can be attributed to the uncertainty in the model predictions, whereas the same is true for T_{peak} only

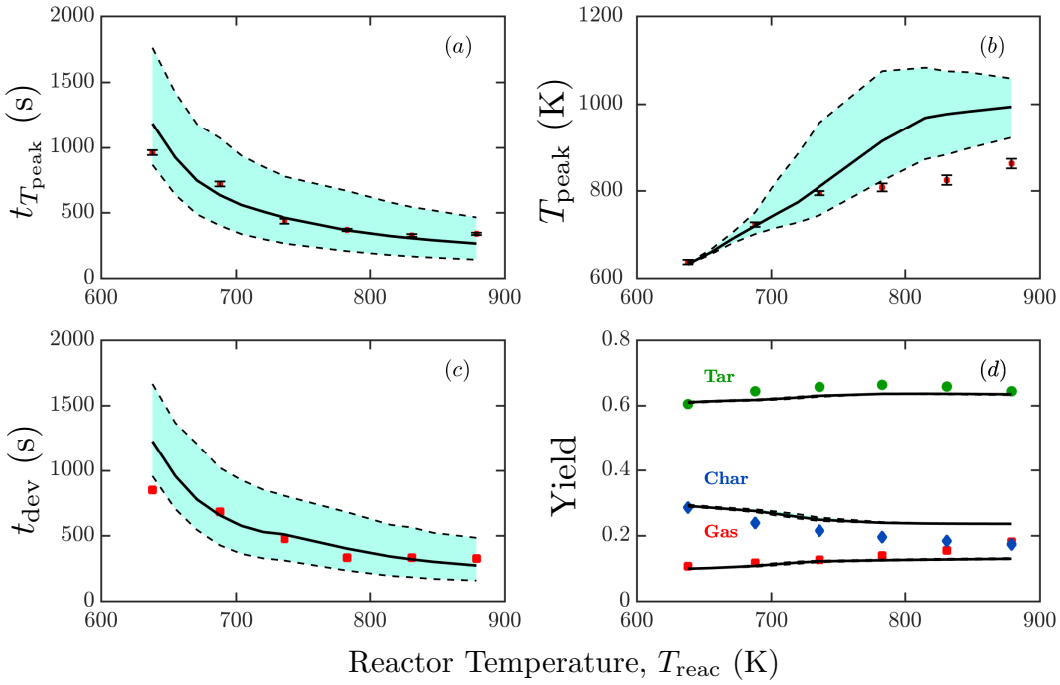

Figure 3.6: Comparison between the predictions of $\mathcal{M}_{\mathcal{P}}$ (solid lines: mean; dashed lines: 95% coverage of uncertainty) and the experimental measurements (symbols, $\mathscr{E}_{\text{I}}$).

when $T_{\text{reac}} < 783$ K. In the experiments $\mathscr{E}_{\text{I}}$, a steep temperature rise is observed at the particle center exceeding the surface temperature (Fig. 3.2(b)), which has been linked to the exothermic decomposition of the intermediate solids formed during the pyrolysis process [133]. In $\mathscr{E}_{\text{I}}$, this overshoot of the center temperature above the surface temperature is found to first increase and then decrease with T_{reac}, becoming maximum at T_{reac}=736 K, whereas $\mathcal{M}_{\mathcal{P}}$ predicts the temperature overshoot to continuously increase with T_{reac}. This observation may explain why $\mathcal{M}_{\mathcal{P}}$ fails to predict T_{peak} when $T_{\text{reac}} \geq 783$ K. Improvements in the predictions of T_{peak} for $T_{\text{reac}} \geq$783 K can be a focus area for further developments in the chemical kinetic model, as the uncertainty in the transport model parameters can not explain the discrepancy for it. Figure 6(d) shows that the negligible

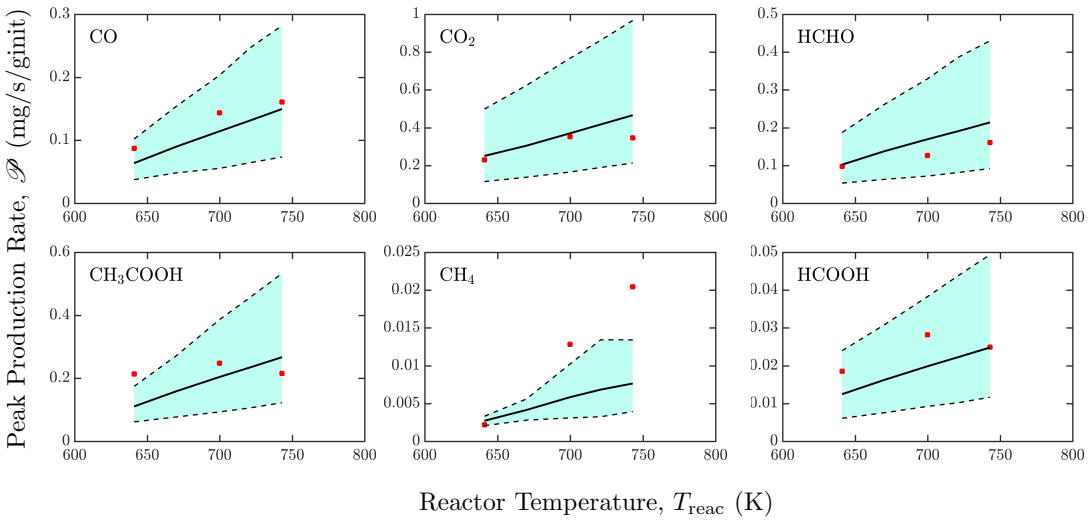

Figure 3.7: Comparison of the experimental measurements (symbols, $\mathscr{E}_{\text{II}}$) and the predictions of $\mathcal{M}_{\mathscr{P}}$ (solid lines: mean; dashed lines: 95% coverage of uncertainty) for peak production rates of different species, $\mathscr{P}$.

uncertainty in the predictions of $\mathbf{Y}^{\text{lump}}$ cannot explain the observation that $\mathcal{M}_{\mathscr{P}}$ overpredicts the yield of SR, yet underpredicts $Y_{\text{gas}}^{\text{lump}}$. The discrepancy in the product yields has been observed in the literature and to some extent, has been linked to an inadequate representation of the chemisorbed species [5, 70].

Figure 3.7 shows that $\mathcal{M}_{\mathscr{P}}$ can accurately predict $\mathscr{P}$ within the uncertainty bounds for all species except CH_4. However, significant discrepancy exists between the experiments and the model predictions of $t_{\mathscr{P}}$ for CO_2, CH_4, and HCOOH at T_{reac} $\geq$700 K as shown in Fig. 3.8. Also, the mean values of the predictions of $t_{\mathscr{P}}$ are found to be smaller than most of the experimental measurements. The results for $\mathscr{P}$ and $t_{\mathscr{P}}$ imply that even though $\mathcal{M}_{\mathscr{P}}$ is able to predict the peak production rates of most species within the uncertainty bounds, it tends to underpredict the timings of species production, especially for CO_2, CH_4, and HCOOH. Similar to the case of $\mathbf{Y}^{\text{lump}}$, the uncertainty in the predic-

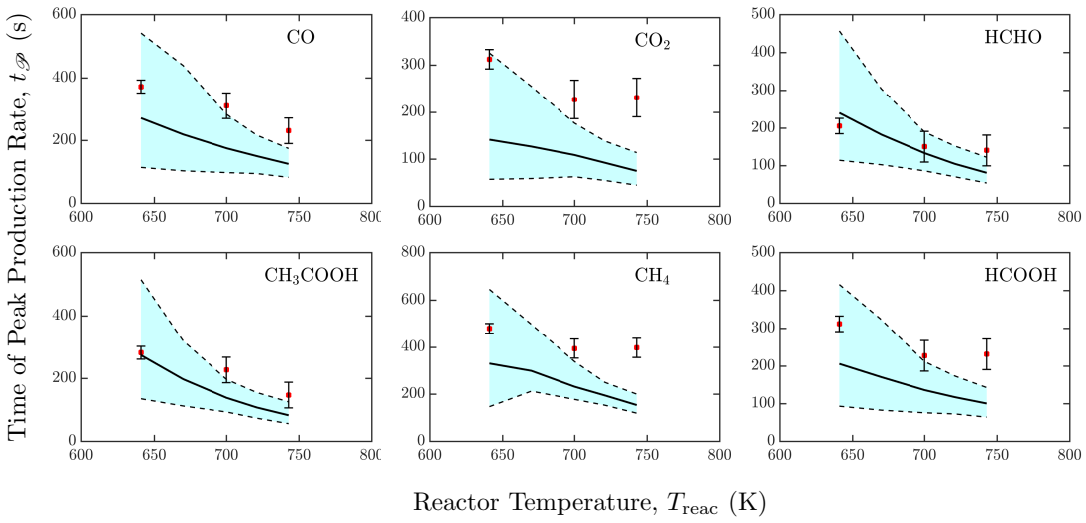

Figure 3.8: Comparison of the experimental measurements (symbols, $\mathscr{E}_{\text{II}}$) and the predictions of $\mathcal{M}_{\mathcal{P}}$ (solid lines: mean; dashed lines: 95% coverage of uncertainty) for time of peak production rate of different species, $t_{\mathscr{P}}$.

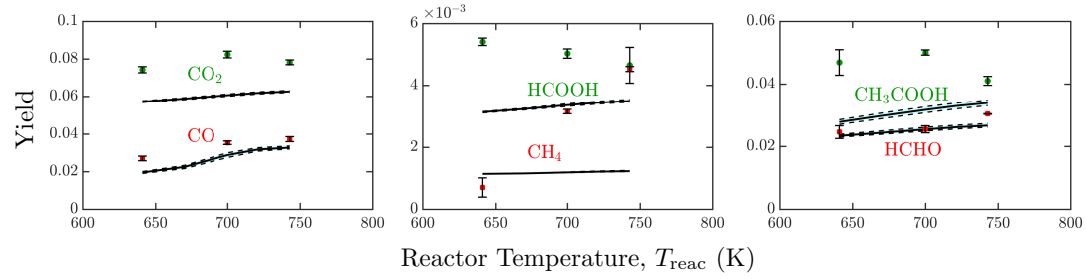

Figure 3.9: Comparison of the experimental measurements (symbols, $\mathscr{E}_{\text{II}}$) and the predictions of $\mathcal{M}_{\mathcal{P}}$ (solid lines: mean; dashed lines: 95% coverage of uncertainty) for yields of different species, $\mathbf{Y}$.

tions of $\mathbf{Y}$ is negligible as shown in Fig. 3.9. $\mathcal{M}_{\mathcal{P}}$ underpredicts the yields of all the gas species, and the deviations with the experimental measurements are up to a factor of four for CH_4, and within a factor of two for other species. The results presented in Figs 3.7–3.9 show that $\mathcal{M}_{\mathcal{P}}$ performs poorly for the predictions of all the targets related to CH_4. In the literature, other studies have also

reported the inability of the chemical kinetic model used in this work to accurately predict the evolution of CH_4 and light hydrocarbons [33, 5, 70]. In the kinetic model, CH_4, as well as other light hydrocarbons, are mainly produced in the form of chemisorbed species releasing slowly from the solid matrix. The main reason for adding these chemisorbed species in the kinetic model was to match the mass loss data observed experimentally, and their kinetic parameters remain partially adaptive [33]. The uncertainty analysis shows that the kinetics of the chemisorbed species require further development to improve the predictions of CH_4 and probably other light hydrocarbons.

The uncertainty analysis for $\mathscr{E}_{\mathrm{I}}$ shows that the model predictions related to the particle temperature profiles are, in general, in good agreement with the experiments if the uncertainty in the model predictions is included. However, a few targets such as T_{peak} for T_{reac}¿783 K and the yields of Gas and SR require further improvements in the pyrolysis model. The UQ results for $\mathscr{E}_{\mathrm{II}}$ show that $\mathcal{M}_{\mathcal{P}}$ performs poorly for all the targets related to CH_4. Also, the predictions of the species yields and $t_{\mathscr{P}}$ for CO_2, CH_4, and HCOOH need to be improved. Moreover, for both $\mathscr{E}_{\mathrm{I}}$ and $\mathscr{E}_{\mathrm{II}}$, the predictive ability of $\mathcal{M}_{\mathcal{P}}$ is observed to decrease at higher temperatures. Further improvements in the chemical kinetic model focusing on the targets described here are likely needed to improve the predictive ability of the 1D pyrolysis model.

Optimization of the uncertain model parameters

Uncertainty in the model parameters provides some flexibility in tuning them to improve the model predictions. In the biomass literature, the tuning of the

model parameters is usually done in an *ad-hoc* manner. In this work, the optimal values of the parameters included in set $\mathcal{H}$ are estimated by minimizing the objective function $\Phi(\mathbf{x})$ defined in Eq. 3.19 using the default nonlinear optimization solver in GAMS [18], a commercial software to solve optimization problems. The obtained optimal values of the parameters in $\mathcal{H}$ are provided in Table 3.4. Comparisons of the predictions of the targets obtained from $\mathcal{M}_{\mathcal{P}}^{*}$ and

Table 3.4: Optimal values of the uncertain model parameters.

Model parameters in $\mathcal{H}$	Units	Optimal values of the parameters in $\mathcal{H}$
λ_w	W/m·K	0.471
λ_c	W/m·K	0.136
C_w	J/kg·K	$412.5 + 6.57T$
C_c	J/kg·K	$1218 + 0.301T - 6.20\times10^{7}T^{-2}$

$\mathcal{M}_{\mathcal{P}}$ are shown in Fig. 3.10 for $\mathscr{E}_{\mathrm{I}}$, and Figs. 3.11 and 3.12 for $\mathscr{E}_{\mathrm{II}}$. Figures 3.10–3.12 show that the optimization of the uncertain model parameters has improved the model predictions for most of the targets. Yields are not included in the comparisons as negligible uncertainty is observed in their values and thus, the optimization of the parameters in $\mathcal{H}$ does not affect their predictions.

To evaluate the improvement in the model predictions after the optimization, the L^2 error norm $\mathcal{E}$ is calculated between the experiments and the predictions of $\mathcal{M}_{\mathcal{P}}^{*}$ and $\mathcal{M}_{\mathcal{P}}$:

$$\mathcal{E} = \sqrt{\frac{1}{n}\sum_{i=1}^{n}\left(\frac{\eta_i(\mathbf{x}) - \eta_i^{\mathrm{obs}}}{\eta_i^{\mathrm{obs}}}\right)^2}. \tag{3.24}$$

In Eq. 3.24, $\mathcal{E}$ for $\mathcal{M}_{\mathcal{P}}^{*}$ and $\mathcal{M}_{\mathcal{P}}$ is obtained by substituting $\mathbf{x}$ by $\mathbf{x}^{*}$ and $\mathbf{0}$, respectively. The values of $\mathcal{E}$ for $\mathcal{M}_{\mathcal{P}}^{*}$ and $\mathcal{M}_{\mathcal{P}}$ are found to be 0.29 and 0.34, respectively, showing that the optimization of the parameters in $\mathcal{H}$ does not provide

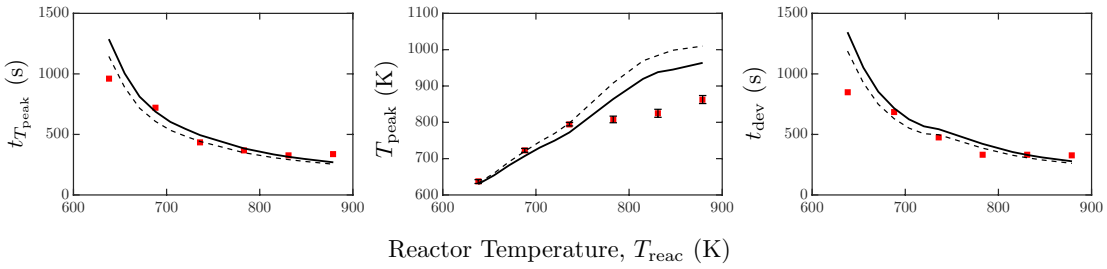

Figure 3.10: Comparison between the predictions of the optimized model (solid lines), the base model (dashed lines), and the experimental measurements (symbols) for the targets of $\mathscr{E}_{\text{I}}$.

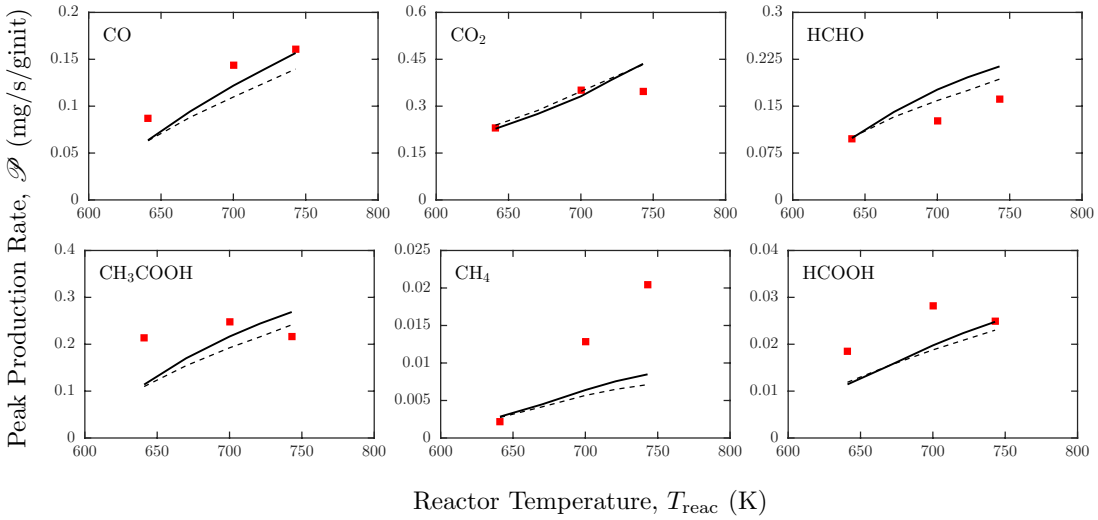

Figure 3.11: Maximum production rates of species $\mathscr{P}$ for $\mathscr{E}_{\text{II}}$. Comparison between the predictions of the optimized model (solid lines), the base model (dashed lines), and the experimental measurements (symbols).

a significant improvement (15% reduction in $\mathcal{E}$) in the model predictions even though the experimental measurements of several targets fall within the uncertainty bounds of the model predictions. This can be explained by realizing that each target can have a unique set of model parameters that minimizes the differences between the experimental measurements and the model predictions.

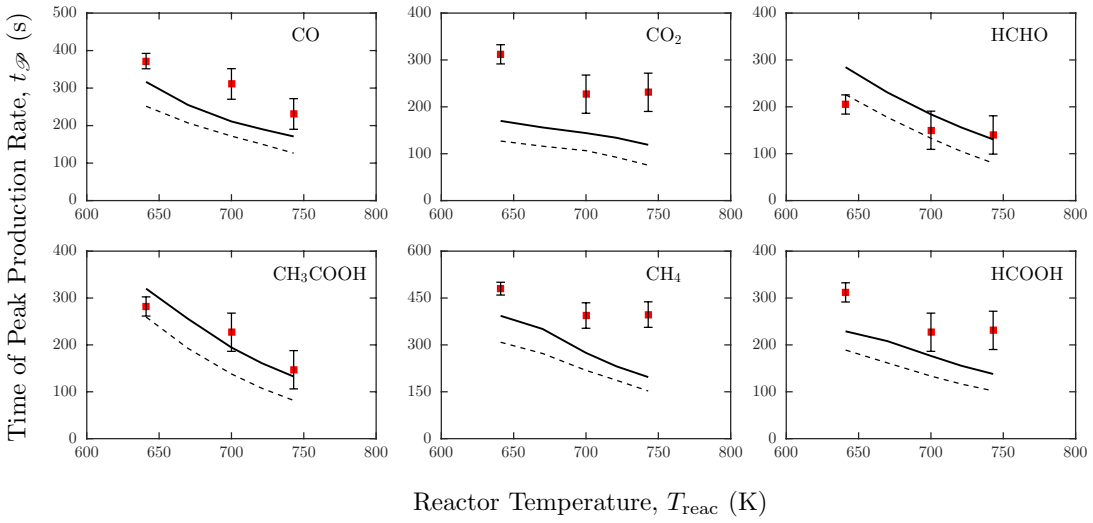

Figure 3.12: Time for maximum production rates of species $t_{\mathscr{P}}$ for $\mathscr{E}_{\text{II}}$. Comparison between the predictions of the optimized model (solid lines), the base model (dashed lines), and the experimental measurements (symbols).

For biomass pyrolysis, no single target can accurately characterize the overall pyrolysis process, and therefore biomass pyrolysis model must be able to predict multiple targets that are governed by different physical and chemical processes. To check how much the optimized model can be improved when only a single target is considered, we optimize the parameters in $\mathcal{H}$ for T_{peak}. We observe that the resulting optimized model provides a significant improvement in the predictions of T_{peak} as shown in Fig. 3.13. For this case, 75% reduction in $\mathcal{E}$ is achieved by the optimized model ($\mathcal{E}$=0.03) in comparison to the base model ($\mathcal{E}$=0.12).

The results of the optimization study have an important implication that an excellent agreement can be obtained between the model predictions and the experiments by tuning the uncertain model parameters if only a few targets are considered in the validation process. Therefore, in the presence of uncertainty in

the model parameters, consideration of a wide variety of detailed experimental measurements becomes vital for a rigorous model validation.

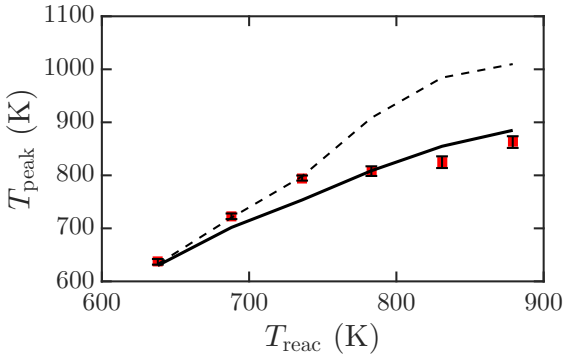

Figure 3.13: Comparison between the predictions of the optimized model (solid lines), the base model (dashed lines), and the experimental measurements (symbols) for the predictions of T_{peak} for $\mathscr{E}_{\text{I}}$.

3.6 Conclusions

In this work, a rigorous analysis of the validity of a commonly used one-dimensional particle-scale biomass pyrolysis model was performed using uncertainty quantification and the optimal values of the uncertain model parameters were evaluated. For this purpose, two detailed experimental studies of the pyrolysis of spherical wood spheres were considered from the literature. By combining sensitivity analysis and literature search, a set of sensitive transport model parameters was identified and the uncertainty in their values was characterized using uniform distribution. To perform the uncertainty propagation and the optimization of the uncertain model parameters, response surfaces were created to allow for a fast evaluation of the model predictions. The response surfaces were evaluated by sampling the PDFs of the uncertain model param-

eters to propagate the uncertainty through the pyrolysis model. The resulting model predictions containing the uncertainty were compared to the experimental measurements of several targets. We found that the uncertainty in the model predictions can account for most of the discrepancies related to the particle temperature profiles and the species production rates. However, the discrepancies related to the product yields and the timings of the peak production rates of a few species cannot be explained by the uncertainty. The results also showed that the pyrolysis model performs poorly in predicting all the targets related to CH_4. The experimental targets identified in this work, whose predictions cannot be improved by an accurate knowledge of the transport model parameters, can be a focus area for further developments in the chemical kinetic model.

The optimization study showed that the optimal values of the uncertain model parameters could achieve a minor improvement (15% reduction in the L^2 error norm) in the model predictions when all the targets were considered, whereas a significant improvement (75% reduction in the L^2 error norm) was obtained when only a single target (T_{peak}) was considered. This observation emphasizes the importance of considering a wide variety of experimental targets during the model validation process, as good agreement can be obtained between the model predictions and the experiments by tuning the model parameters if only a few targets are considered.

The present work is a first step towards developing the UQ methodology in the context of biomass pyrolysis, and we have made several simplifying assumptions, including the 1D spherically symmetric and isotropic representation of the biomass particle. The methodology used in this work is systematic and general, and provided that adequate computational resources are available, can

in theory be applied to more complex simulation configurations associated with realistic biomass feedstock.

CHAPTER 4

A COMPUTATIONAL STUDY OF THE EFFECTS OF MULTIPHASE DYNAMICS IN CATALYTIC UPGRADING OF BIOMASS PYROLYSIS VAPOR

4.1 Abstract

A recurring challenge among the variety of existing biomass-to-biofuel conversion technologies is the need to ensure optimal and homogeneous contact between the various phases involved. The formulation of robust design rules from an empirical standpoint alone remains difficult due to the wide range of granular flow regimes coexisting within a given reactor. In this work, a volume-filtered Eulerian-Lagrangian framework is employed that solves chemically reacting flows in the presence of catalytic particles. The simulation strategy is used to quantify the role of the particle clustering on catalytic upgrading of biomass pyrolysis vapor in risers. It is shown that particle clustering can reduce the catalytic conversion rate of biomass pyrolysis vapors by up to about 50%. The simulation results are also compared with an engineering model based on continuously stirred tank reactor (CSTR). A one-dimensional Reynolds-averaged transport equation is derived, and the unclosed terms that account for the heterogeneity caused by clusters are evaluated.

4.2 Introduction

In response to global climate change and society's continuously growing energy demand, there have been substantial efforts in recent years to reduce our dependence on fossil fuels and limit their associated environmental impacts. Many countries and regions have set aggressive goals for near-term deployment of second-generation biofuels derived from lignocellulosic biomass. By 2013, biofuel blend mandates were identified at the national level in 27 countries, and regulatory policies promoting the use of biofuels existed in more than 49 countries [154]. However, the high cost associated with efficient conversion of biomass to biofuel and the difficulties in developing new conversion processes make the large-scale commercialization of biofuels a significant challenge [30, 52].

Among technologies for developing liquid biofuels derived from lignocellulosic biomass, thermochemical conversion techniques (e.g., gasification and pyrolysis) show great promise for being economically competitive with conventional petroleum derived gasoline and diesel [40, 183, 55]. In particular, the fast pyrolysis process in fluidized bed reactors is an emerging technology that can potentially yield liquids of up to 75% weight on a dry-feed basis [17, 16]. The biomass volatile obtained from fast pyrolysis can be upgraded over a catalyst (e.g., zeolites or silica-alumina) prior to condensation for improving the compatibility of bio-oil with conventional processing infrastructure, yet this technology is still far from industrial application [113].

Catalytic upgrading of biomass is typically done in the riser of a circulating fluidized bed reactor (CFB), characterized by gas velocities greatly exceeding

minimum fluidization. The high flow rates encountered in CFB risers cause the flow to become unsteady with large fluctuations in catalyst concentration. Local regions of densely packed catalytic particles, referred to as clusters, develop in the flow and fall at the walls of the reactor, while dilute suspensions of particles rise in the central region [124]. Clusters have been observed to reduce mixing and interaction of particles with the transport gas [160, 27], potentially lowering operating efficiencies significantly. Meanwhile, detailed studies demonstrating the quantitative impact of particle clustering on chemical processes occurring in such flows remain elusive.

Because the solid phase is opaque and highly unsteady, experimental studies on the fluidization of biomass have proven to be an arduous task [34]. In addition, the wide range of length and time scales associated with chemically reacting multiphase turbulence poses severe challenges in developing predictive models [138]. In recent years, computational fluid dynamics (CFD) has emerged as a promising tool to study the multiphase dynamic effects in practical pyrolysis reactors. Simulating catalytic conversion in fluidized bed reactors requires a kinetic model to describe the complex chemistry and a framework for solving gas-solid flows. The gas-solid description is typically computed using Eulerian-Eulerian (EE) or Eulerian-Lagrangian (EL) methods. EE representations solve the gas phase and solid particles on a common Eulerian grid, greatly reducing the computational cost as individual particles do not need to be tracked. In the limit where the flow is highly collisional and assumed to be nearly at equilibrium, the particle density function is close to Maxwellian and a Chapman-Enskog expansion can be used to derive a two-fluid model (TFM) using ensemble or volume averaging [65, 195, 135].

Lathouwers and Bellan [90] provided a comprehensive model for describing the thermofluid dynamics of dense, reactive, gas-solid mixtures to study the influence of operating parameters on tar yields during biomass pyrolysis. The equations were derived from the kinetic theory of granular flow and take into account multiple chemical reactions in both phases. In a more recent study, Xue et al. [193] combined TFM with a lumped, multi-component, multi-stage kinetic model. The model was used to simulate for the first time steady-state conditions of fast pyrolysis in a lab-scale fluidized-bed reactor. Within the last 15 years, the application of TFM to biomass pyrolysis has primarily focused on modeling dense two-dimensional bubbling fluidized bed reactors [90, 62, 193, 191, 192, 186, 196, 136, 15]. Lee et al. [93] recently performed several Euler-Euler simulations of biomass pyrolysis in three-dimensional bubbling fluidized beds to investigate the effect of bed geometry on biomass pyrolysis.

Due to the increased flow rates in CFB risers, the particle concentration becomes highly non-uniform and the velocity distribution deviates far from equilibrium. In this regime, particle trajectory crossings play an important role and higher moments of the particle number density must be considered to yield accurate results [42]. EL strategies provide an alternative framework that typically rely on simpler closures compared to EE. With EL, individual particle trajectories are solved using Newton's laws of motion, and models are required for interphase exchange and particle collisions. Due to the added computational expense of tracking individual particles, EL methods coupled with a kinetic model have only recently been applied in three dimensions [20, 100, 27], and are generally limited to the dense granular flow regime near the inlet of the reactor. Most EL studies to date consider two-dimensional flows with a relatively small number of particles (e.g., [54, 129, 125, 149, 69, 70]). Recent work [26, 96]

has demonstrated that two-dimensional simulations are only capable of capturing qualitative features of particle clustering, and a fully three-dimensional description is required to accurately capture the quantitative flow behavior in CFB risers. Capecelatro et al. [27] performed three-dimensional EL simulations of catalytic particles in a periodic pipe flow. Those simulations showed that the presence of clusters delayed the conversion process by up to 85% compared to a corresponding homogeneous flow. However, the simulations did not account for spatial variations in the vertical direction that are known to have a large effect on biomass fast pyrolysis [173]. More details about CFD simulations of biomass pyrolysis can be found in a recent review by Xiong et al. [190].

In this study, we focus on characterizing and quantifying the effect of cluster formation on catalytic conversion in a three-dimensional CFB riser. The catalysts are representative of zeolites (e.g., HZSM-5), as they have been found to promote high yields of liquid products [16]. The EL approach is coupled with a simple kinetic model such that biomass vapors react with the catalytic particles to form light gases and cracked hydrocarbons. In section "Volume-filtered Euler-Lagrange approach", we present a volume-filtered EL approach for solving chemically reacting flows in the presence of solid particles, and provide a description of the corresponding numerical implementation. Simulation results are analyzed in section "Catalytic upgrading of volatile in a CFB riser". A comparison of simulation results with a representative engineering model is made in section "Reduced-order modeling". Finally, a reduced-order model based on Reynolds-averaging is proposed to account for the heterogeneity introduced by the multiphase dynamics in section "Reduced-order modeling". We are using SI units throughout the paper.

4.3 Volume-filtered Euler-Lagrange approach

The unsteady and multiscale nature of chemically reacting multiphase turbulence poses significant modeling challenges. In typical fluidized bed configurations for example, surface reactions and fluid instabilities taking place at the particle scale will ultimately influence the overall macroscopic behavior. Furthermore, the time scales associated with the reaction rates are often orders of magnitude smaller than the typical residence time of the gas phase. In order to formulate a system of equations that remain computationally tractable, a separation of length scales is established by introducing a local volume filter to the microscale (i.e., sub-particle scale) equations of motion [6, 25]. To capture a significant portion of the small-scale features of the flow while enabling the use of classical models for microscale processes such as particle drag and mixture viscosity, the filter length scale δ_f should satisfy $d_p \ll \delta_f \ll \mathcal{L}$, where d_p is the particle diameter and $\mathcal{L}$ is a characteristic size of the mesoscale flow features (e.g., clusters). The corresponding volume-filtered EL equations are presented below. The reader is referred to Capecelatro et al. [25] for a more detailed description and complete derivation of those equations.

4.3.1 Gas-phase description

The volume-filtered continuity equation for a variable density flow is given by

$$\frac{\partial}{\partial t}\left(\varepsilon_f \rho_f\right) + \nabla \cdot (\varepsilon_f \rho_f \boldsymbol{u}_f) = 0. \tag{4.1}$$

where ε_f, ρ_f, and $\boldsymbol{u}_f$ are the volume-filtered fluid-phase volume fraction, density, and velocity, respectively. Here, we assume that catalytic coking does not

become significant: therefore, the particle size remains constant. A comparison of the timescales for mass transfer between a particle and the surrounding gas and the gas-particle reaction shows that the mass transfer process is significantly faster than the catalytic reaction. Also, from the literature [95], for gas-porous catalyst system the mass transfer between the particle and the surrounding gas has negligible effect on the catalytic reaction. Hence, mass transfer resistance between the particle and the surrounding gas is neglected. The volume-filtered fluid-phase momentum equation is given by

$$\frac{\partial}{\partial t}\left(\varepsilon_f \rho_f \boldsymbol{u}_f\right) + \nabla \cdot \left(\varepsilon_f \rho_f \boldsymbol{u}_f \otimes \boldsymbol{u}_f\right) = \nabla \cdot (\boldsymbol{\tau} - \boldsymbol{\mathcal{R}}_u) + \varepsilon_f \rho_f \boldsymbol{g} - \boldsymbol{F}^{\text{inter}}, \tag{4.2}$$

where $\boldsymbol{\tau}$ is the volume-filtered stress tensor, $\boldsymbol{\mathcal{R}}_u$ is akin to a Reynolds stress and requires closure, $\boldsymbol{g}$ is the gravity vector, and $\boldsymbol{F}^{\text{inter}}$ represents the interphase exchange between particles and the fluid, which will be made explicit in subsection "Interphase exchange". The isotropic part of sub-filter Reynolds stress term is absorbed in the fluid pressure p, whereas the anisotropic part is closed via a turbulent viscosity model, given by

$$\boldsymbol{\mathcal{R}}_u \approx \mu_t \left[\nabla \boldsymbol{u}_f + \nabla \boldsymbol{u}_f^{\mathsf{T}}\right], \tag{4.3}$$

where μ_t, analogous to a turbulent viscosity, is computed via a dynamic Smagorinsky model [63, 99] based on Lagrangian averaging [108]. The volume-filtered fluid-phase stress tensor is expressed as

$$\boldsymbol{\tau} = -p\boldsymbol{I} + (\mu + \mu^*)\left[\nabla \boldsymbol{u}_f + \nabla \boldsymbol{u}_f^{\mathsf{T}} - \frac{2}{3}\left(\nabla \cdot \boldsymbol{u}_f\right)\boldsymbol{I}\right], \tag{4.4}$$

where $\boldsymbol{I}$ is the identity matrix, μ is the dynamic viscosity. The effective viscosity, μ^*, arises from filtering the velocity gradients in the microscale viscous stress tensor and accounts for enhanced dissipation by the particles. In this work, an effective viscosity derived by Gibilaro et al. [64] for fluidized beds is used, given

by

$$\mu^* = \mu\left(\varepsilon_f^{-2.8} - 1\right). \tag{4.5}$$

Volume-filtered transport of reactive species i is given by

$$\frac{\partial}{\partial t}\left(\varepsilon_f \rho_f Y_i\right) + \nabla \cdot \left(\varepsilon_f \rho_f \boldsymbol{u}_f Y_i\right) = \nabla \cdot \left(\varepsilon_f \rho_f D_i \nabla Y_i - \boldsymbol{\mathcal{R}}_{Y_i}\right) + \dot{\omega}_i, \tag{4.6}$$

where Y_i is its mass fraction, D_i is its mass diffusivity, $\dot{\omega}_i$ is its filtered chemical source term, described in detail in the following section, and $\boldsymbol{\mathcal{R}}_{Y_i}$ is a sub-filtered scalar flux. In turbulent combustion, closure for the sub-filter scalar flux is generally obtained by employing a gradient transport assumption and introducing a turbulent-like diffusivity D_t. Following Moin et al. [112], we introduce a dynamic formulation for D_t similar to the dynamic Smagorinsky model used in computing μ_t in Eq. 4.3.

The riser reactor is modeled as a vertical pipe with inlet and outlet boundary conditions. To account for the cylindrical geometry on a Cartesian mesh, a conservative immersed boundary (IB) method is employed. The IB method is based on a cut-cell formulation that requires rescaling of the convective and viscous fluxes in these cells [110]. At the reactor walls, no-slip and no penetration boundary conditions are used for the fluid and zero-gradient is enforced for the scalars.

4.3.2 Chemical kinetics for catalytic conversion

The kinetics of the catalytic conversion process are expected to have a significant impact on the quality and accuracy of the unsteady multiphase simulations, and therefore need to be modeled appropriately. However, the typical size of the

Table 4.1: Chemical compounds and their representative species. Elemental composition and molar mass chosen to match average conversion product distribution as listed in [1, 2].

Compound class	Name	W [g/mol]	ν [-]	Representative species
Bio-oil volatile fraction	VOL	150	-1	*ad-hoc* [1]
Light gases	GAS	28	0.175	CO
Hydrocarbons	HC	92	1.575	Toluene
Inert medium	N_2	28	0	Nitrogen

reactor, even at laboratory scale, combined with the complexity of the associated multiphase flows, warrants the use of a highly lumped kinetic scheme. In this study, we assume that biomass vapors react with catalysts to form light gases and cracked hydrocarbons, according to a simple one-step reaction

$$\mathrm{VOL} + \mathrm{CAT} \longrightarrow \nu_{\mathrm{GAS}}\mathrm{GAS} + \nu_{\mathrm{HC}}\mathrm{HC} + \mathrm{CAT}, \tag{4.7}$$

where ν_i is the stoichiometric coefficient of species i, and the gas phase representative species, used to evaluate the gas mixture properties, are defined in Table 1. The reaction assumes that the catalytic conversion process is isothermal and catalyst particles do not deactivate. [1] The reaction coefficient for the decomposition of biomass volatile is prescribed as

$$k = k_0 \frac{\varepsilon_p}{\varepsilon_{p,0}}, \tag{4.8}$$

where $\varepsilon_{p,0} = 0.634$ is the random close-packing limit for monodisperse spherical particles [158], and k_0 is chosen to obtain a specified conversion rate at the reactor exit. The consumption of biomass volatile is then obtained from the chemical

[1] Elemental composition and molar mass chosen to match average conversion product distribution as listed in [1, 2]

source term

$$\dot{\omega}_i = \nu_i W_i k[\text{VOL}], \tag{4.9}$$

where W_i is the molecular weight of species i, and the concentration of volatile is given by $[\text{VOL}] = \varepsilon_f \rho_f Y_{\text{VOL}}/W_{\text{VOL}}$.

4.3.3 Particle-phase description

As described in the previous section, solid particles aid in the decomposition rate of biomass pyrolysis vapors to produce light gases (represented by CO) and cracked hydrocarbons (represented by toluene). In this work, the solid phase is treated in a Lagrangian framework, where individual particle trajectories are solved using Newton's second law of motion. Particles are represented as spheres of diameter d_p that are much denser than the surrounding fluid ($\rho_p \gg \rho_f$). The equations of motion for the particles are given by

$$\frac{d\boldsymbol{x}_p}{dt} = \boldsymbol{u}_p, \tag{4.10}$$

$$m_p \frac{d\boldsymbol{u}_p}{dt} = \boldsymbol{f}_p^{\text{inter}} + \boldsymbol{F}_p^{\text{col}} + m_p \boldsymbol{g}, \tag{4.11}$$

$$I_p \frac{d\boldsymbol{\omega}_p}{dt} = \sum_{j \neq p} \frac{d_p}{2} \boldsymbol{n} \times \boldsymbol{f}_{t,j\to p}^{\text{col}}, \tag{4.12}$$

where $\boldsymbol{x}_p$ is the position of particle p, $\boldsymbol{u}_p$ is the particle velocity, $\boldsymbol{\omega}_p$, its angular velocity, $m_p = \pi \rho_p d_p^3/6$, its mass, and I_p, its moment of inertia given for a sphere by

$$I_p = \frac{m_p d_p^2}{10}. \tag{4.13}$$

In Eq. 4.11, $\boldsymbol{f}_p^{\text{inter}}$ is the force particle p experiences from the carrier fluid, as described in the following sub-section, and $\boldsymbol{F}_p^{\text{col}}$ is the collisional force that particle p experiences with adjacent particles and the walls. Particles rebound at

the walls with a coefficient of restitution of 0.8. Collisions are handled via a soft-sphere approach originally proposed by Cundall and Strack [35]. Particle rotation is assumed to be only a function of the tangential component of the collision force, $\boldsymbol{f}_t^{\text{col}}$, that is solved based on the Coulomb friction law. Further details can be found in ref. [25].

4.3.4 Interphase exchange

Coupling between the gas phase and solid particles arise in the form of gas volume fraction ε_f and interphase exchange term $\boldsymbol{F}^{\text{inter}}$, expressed as

$$\varepsilon_p = 1 - \varepsilon_f \approx \sum_{p=1}^{N_p} G\left(\left|\boldsymbol{x} - \boldsymbol{x}_p\right|\right) V_p, \tag{4.14}$$

and

$$\boldsymbol{F}^{\text{inter}} \approx \sum_{p=1}^{N_p} G\left(\left|\boldsymbol{x} - \boldsymbol{x}_p\right|\right) \boldsymbol{f}_p^{\text{inter}}. \tag{4.15}$$

In the equations above, G is the filtering kernel taken to be Gaussian with a characteristic size $\delta_f = 8d_p$, and $\boldsymbol{f}_p^{\text{inter}}$ is given by

$$\boldsymbol{f}_p^{\text{inter}} \approx V_p \nabla \cdot \boldsymbol{\tau} + \boldsymbol{f}_p^{\text{drag}}, \tag{4.16}$$

with $\boldsymbol{f}_p^{\text{drag}}$ the drag force acting on the particle. The first term on the right-hand side of Eq. 4.16 represents contributions from the resolved fluid stresses that each particle experiences, and the last term accounts for the sub-filtered stresses in the form of drag that depends on the gas-phase velocity and volume fraction. The gas-phase variables are interpolated to the location of the particle via second-order trilinear interpolation and are used in the computation of the drag force given by

$$\frac{\boldsymbol{f}_p^{\text{drag}}}{m_p} = \frac{\varepsilon_f}{\tau_p}(\boldsymbol{u}_f - \boldsymbol{u}_p) F(\varepsilon_f, \text{Re}_p), \tag{4.17}$$

where $\tau_p = \rho_p d_p^2/(18\mu)$ is the particle response time derived from a Stokes flow assumption, and the particle Reynolds number is given by

$$\mathrm{Re}_p = \frac{\varepsilon_f \rho_f \left|\boldsymbol{u}_f - \boldsymbol{u}_p\right| d_p}{\mu}. \tag{4.18}$$

F is the dimensionless drag force coefficient of Tenneti et al. [171], which depends on the particle Reynolds number and fluid volume fraction experienced by the particle. An exhaustive description of the formulation can be found in ref. [25].

4.3.5 Numerical Implementation

The volume-filtered variable density equations are implemented in the framework of NGA [41], a fully conservative CFD code tailored for turbulent flow computations. The Navier-Stokes equations are solved on a staggered grid with second-order spatial accuracy for both the convective and viscous terms, and the second-order accurate semi-implicit Crank-Nicolson scheme of ref [144] is implemented for time advancement. The details on the mass, momentum, and energy conserving finite difference scheme are available in ref. [41].

The particles are distributed among the processors based on the underlying domain decomposition of the gas phase. For each particle, its position, velocity, and angular velocity are solved using a second-order Runge-Kutta scheme. To properly resolve the collisions without requiring an excessively small timestep, particles are restricted to move no more than one tenth of their diameter per timestep.

4.4 Catalytic upgrading of volatile in a CFB riser

4.4.1 Simulation configuration

Three-dimensional simulations are conducted to study catalytic upgrading of biomass in the CFB riser shown in Fig. 4.1. The catalysts are assumed to be spherical, with diameter $d_p = 100\mu$m, density $\rho_p = 875\,\mathrm{kg/m^3}$, both coefficient of restitution $e = 0.8$, and coefficient of friction $\mu_f = 0.1$ for particles and walls. The particles are initially uniformly distributed on a Cartesian lattice with a mean concentration $\overline{\varepsilon}_p = 0.05$, where $\bar{(\cdot)}$ denotes an average in space and time. The three-dimensional domain consists of $1024 \times 72 \times 72$ grid points and 1.16×10^6 particles. As catalytic particles leave the riser at the top, new particles are injected at the bottom cells such that the mean particle volume fraction in the reactor remains constant. We vary the reaction rate constant and the inlet gas-phase velocity, and consider three simulation cases, $\mathcal{S}1$, $\mathcal{S}2$, and $\mathcal{S}3$, with different combinations of reaction rate constant and inlet gas-phase velocity. The parameters are listed in Table 2. Simulations were carried out on 288 cores of the SDSC supercomputer Comet with Intel Xeon E5-2680v3 2.5 GHz cores. It required 55,000, 76,000, and 100,000 CPU hours for simulation cases $\mathcal{S}1$, $\mathcal{S}2$, and $\mathcal{S}3$, respectively to obtain converged statistics.

4.4.2 A note on dimensional analysis

We anticipate reduced mixing between the volatile and catalyst particles due to clustering, and the impact of this reduced mixing on the volatile conversion is linked to the Damköhler number, Da, defined as the ratio of reaction rate to

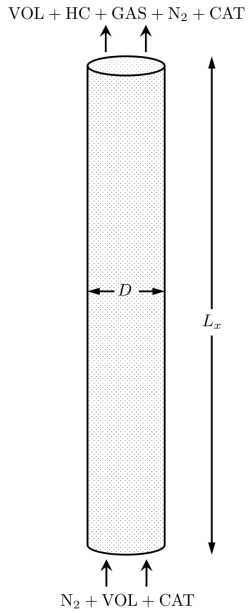

Figure 4.1: Three-dimensional riser configuration.

mass transport rate occurring in the system. The base case reactor configuration, $\mathcal{S}1$, is calibrated such that a 90% conversion is achieved at the exit of the riser by fixing the reaction rate coefficient, k, under the assumption of flow homogeneity. Therefore, for a convection-dominated riser with an homogeneous particle distribution, the Damköhler number is

$$\mathrm{Da} = \frac{k}{U/H} \sim 1, \tag{4.19}$$

where H is the reactor height and U is the inflow velocity at the bottom of the riser. However, inhomogeneities are expected to develop within the reactor in the form of clusters. These clusters hinder mixing between the volatile and the particles. As we only consider the catalytic reaction between volatile and particles, the time scale associated with the transport of volatile into the clusters is expected to increase. Therefore, mesoscale processes in the reactor are characterized by a larger Damköhler number. As a result, the chemical kinetics are

Table 4.2: Parameters for three-dimensional riser simulations.

Name	Units	Value	
Mesh $n_x \times n_y \times n_z$	-	$1024 \times 72 \times 72$	
Number of catalysts N_p	-	1.16×10^6	
Reactor diameter D	m	0.0102	
Height of the reactor L_x	m	0.1536	
Mean catalyst volume fraction	-	0.05	
Pressure	bar	21.7	
Temperature	°C	480	
Catalyst diameter d_p	μm	100	
Catalyst density ρ_p	kg/m^3	875	
Inflow composition Y_i	-	$0.5N_2$ 0.5VOL	
Simulation cases:		$\mathcal{S}1$(Base case)	$\mathcal{S}2$	$\mathcal{S}3$
Inlet velocity U	m/s	0.2	0.2	0.4
Rate constant k_0	s^{-1}	40	80	40

expected to be fast in comparison to the species transport within the reactor, suggesting that clusters will play an important role in the conversion process.

Another important dimensionless number is the axial Péclet number, Pe, that quantifies the extent of backmixing of the gas caused by the clusters falling near the riser walls. Pe is defined as the ratio of the advective flow to dispersive flow in the axial direction [37], given by

$$\mathrm{Pe} = \frac{HU}{\mathcal{D}}, \tag{4.20}$$

where $\mathcal{D}$ is the axial-dispersion coefficient. A large value of $\mathcal{D}$ corresponds to large backmixing of the gas, which is expected to negatively impact the volatile

conversion. For the riser simulations considered in this work, we approximate $\mathcal{D}/\mathrm{H}$ as the downward moving gas velocity averaged over the entire riser, U_{downward}.

4.4.3 Results and discussion

Simulation results are gathered after the initial transient is complete and the flow reaches a statistically stationary state. From Fig. 4.2, the instantaneous flow is observed to be highly unsteady with large spatial inhomogeneity in particle concentration. A snapshot of particle position colored by the vertical component of particle velocity is given in Fig. 4.2(a). Particles tend to fall at the reactor wall and rise in the center, and the lateral distribution of volatile and hydrocarbons is observed to be strongly correlated with particle concentration. As seen in Figs. 4.2(c) and 4.2(d), the volatile is almost entirely depleted at the reactor wall resulting in a high concentration of hydrocarbons. Away from the wall, reduced contact of the volatile with catalytic particles results in a low yield of hydrocarbons.

Figure 4.3 shows the mean particle concentration and mean species mass fractions along the reactor height for simulation cases $\mathcal{S}1$, $\mathcal{S}2$, and $\mathcal{S}3$. We can make the following comments:

- For $\mathcal{S}1$ and $\mathcal{S}2$, the particle concentration is maximum near the inlet, and reduces by more than an order of magnitude at the outlet. In $\mathcal{S}3$, however, the increased inflow velocity leads to significantly different bed hydrodynamics, with a more uniform axial distribution of particle concentration.
- Within five diameters of the inlet, most of the biomass volatile is converted

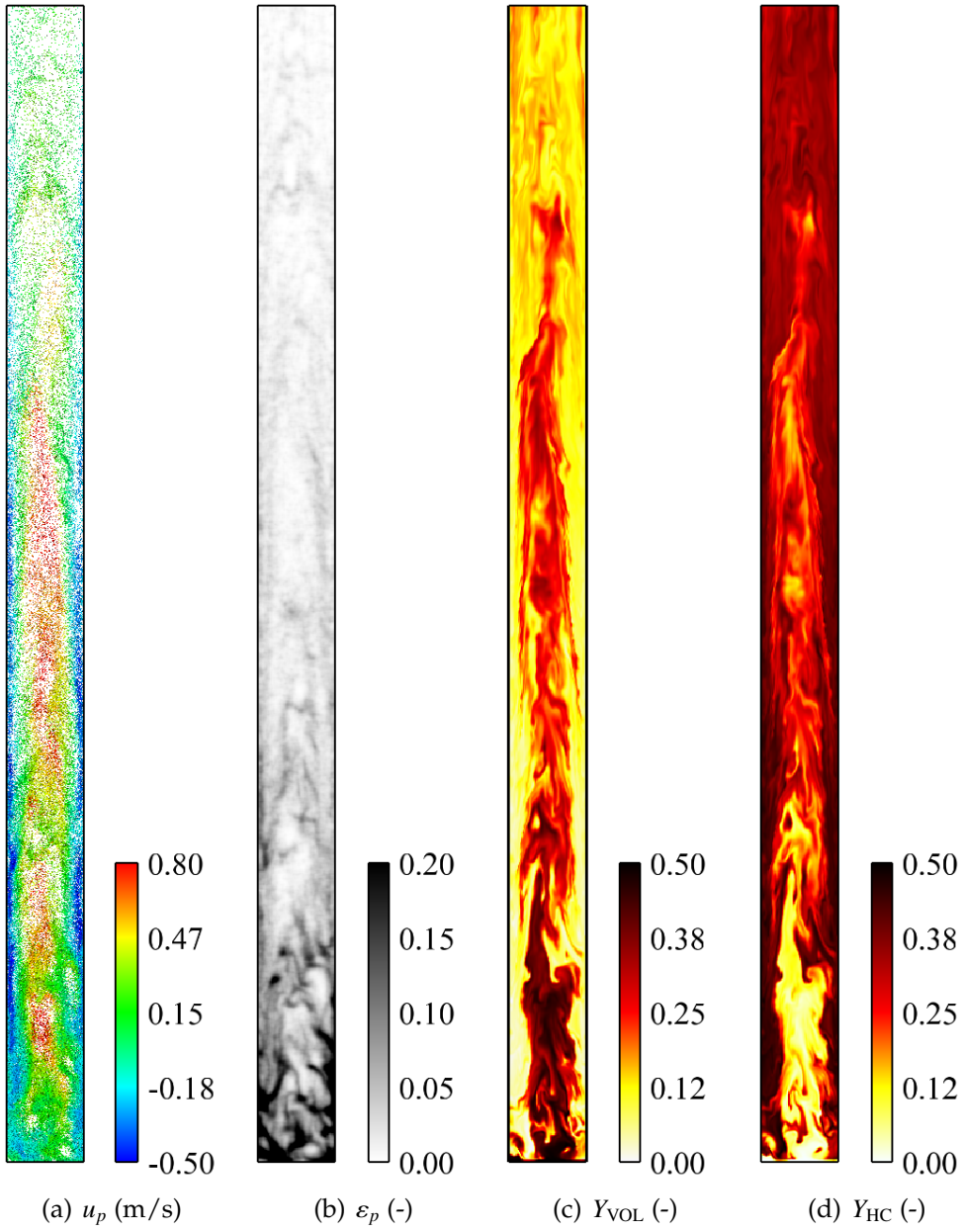

(a) u_p (m/s) (b) ε_p (-) (c) Y_{VOL} (-) (d) Y_{HC} (-)

Figure 4.2: Instantaneous snapshot showing centerline planes of the three-dimensional reactor for $\mathcal{S}1$.

into products for $\mathcal{S}1$ and $\mathcal{S}2$. Above this height, the conversion rate decreases and the species mass fractions remain approximately constant. In contrast, $\mathcal{S}3$ shows a continuous decrease in the biomass volatile up to the reactor outlet. Each riser is also modeled as an homogeneous reactor with

reaction rate constant, k_0 and gas residence time, based on the riser height and the inlet gas velocity, same as that of the riser. In all cases, the volatile mass fractions at the outlet of the riser ($\mathcal{Y}^*_{\text{out}}$ = 0.131 for $\mathcal{S}1$, 0.054 for $\mathcal{S}2$, and 0.185 for $\mathcal{S}3$) are observed to be higher than in the corresponding homogenous cases ($\mathcal{Y}_{\text{out}}$ = 0.05 for $\mathcal{S}1$, 0.005 for $\mathcal{S}2$, and 0.158 for $\mathcal{S}3$). This discrepancy is attributed to the heterogeneity in the particle phase caused by the two-phase flow dynamics.

A more detailed picture of the riser dynamics can be obtained from the radial profiles at various locations of the riser. Figure 4.4 shows the radial profiles of the particle concentration normalized by its average over the cross-sectional area, and the volatile mass fraction at various reactor heights. Following observations can be made:

- A similar level of particle concentration inhomogeneity in the radial direction is observed for all simulation cases, with the particle concentration near the wall approximately twice the particle concentration at the center of the riser.
- For $\mathcal{S}1$ and $\mathcal{S}2$, the volatile is quickly depleted and reaches constant value near the riser wall. However, in the $\mathcal{S}3$ case, a continuous depletion of the volatile is observed near the riser wall along the reactor height despite the radial distribution of the particle concentration being similar to $\mathcal{S}1$ and $\mathcal{S}2$. This suggests an enhanced mixing of the volatile between the riser core and the particle clusters due to higher inlet velocity in $\mathcal{S}3$.

In summary, a higher inlet velocity (in case $\mathcal{S}3$) significantly modifies the axial distribution of the particle phase, yet does not significantly impact its radial

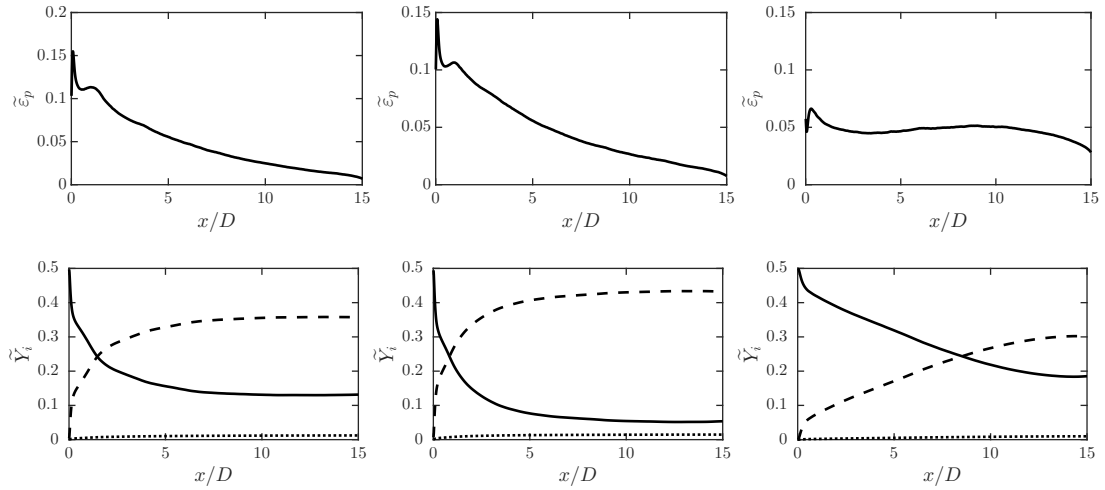

(a) Simulation $\mathcal{S}1$ (b) Simulation $\mathcal{S}2$ (c) Simulation $\mathcal{S}3$

Figure 4.3: Top row: Particle concentration profiles along the reactor height. Bottom row: Species mass fraction profiles along the reactor height: VOL (solid line) HC (dashed line) GAS (dotted line).

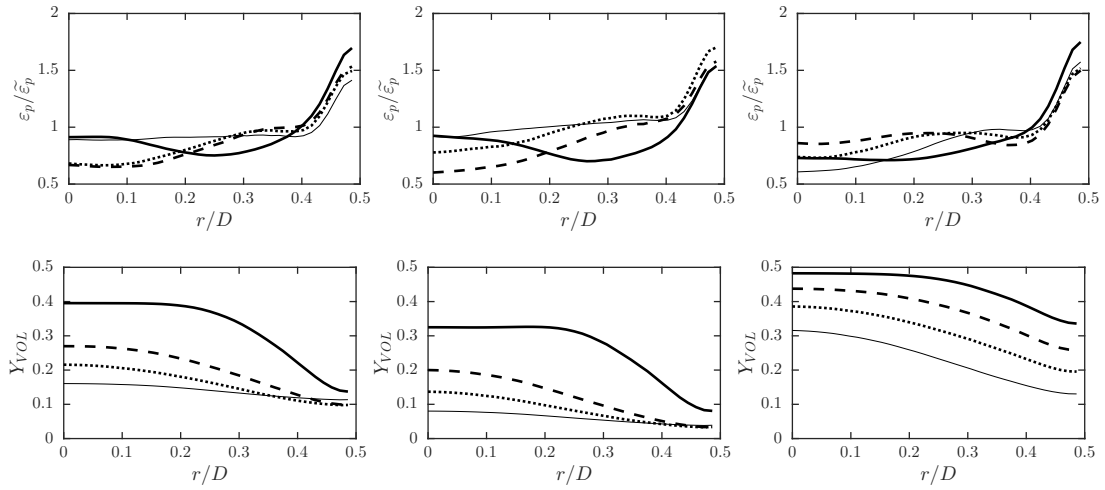

(a) Simulation $\mathcal{S}1$ (b) Simulation $\mathcal{S}2$ (c) Simulation $\mathcal{S}3$

Figure 4.4: Top row: Radial profiles of the particle volume fraction normalized by the cross-sectional average at various reactor heights. Bottom row: Radial profiles of the volatile mass fractions at various reactor heights. x/D = 1 (thick line), 4 (thick dashed line), 7 (thick dotted line), and 12 (thin line).

distribution. However, both the axial and radial profiles of the volatile mass fraction are significantly different for $\mathcal{S}3$ in comparison to $\mathcal{S}1$ and $\mathcal{S}2$. Another important effect of inlet velocity is observed on the backmixing of the gas. To quantify the backmixing, we calculate the average velocity of the downward moving gas, U_{downward}, which is found to be 0.12 m/s, 0.11 m/s, and 0.04 m/s for $\mathcal{S}1$, $\mathcal{S}2$, and $\mathcal{S}3$, respectively. It shows that higher inlet velocity significantly reduces the backmixing of the gas.

To further explore the role of the riser hydrodynamics on the catalytic conversion of the volatile, we introduce an effective reaction rate constant, k_0^*, corresponding to an homogeneous distribution of the particles with the same inlet and outlet volatile mass fractions as the risers simulated in cases $\mathcal{S}1$ to $\mathcal{S}3$.By integrating the rate equations for first order chemical kinetics in an homogeneous system and comparing the reaction rate constants:

$$k_0^* = k_0 \frac{\ln\left(\mathcal{Y}_{\text{out}}^*/\mathcal{Y}_{\text{in}}\right)}{\ln\left(\mathcal{Y}_{\text{out}}/\mathcal{Y}_{\text{in}}\right)}. \tag{4.21}$$

where $\mathcal{Y}_{\text{in}}$=0.5 is the inlet volatile mass fraction, $\mathcal{Y}_{\text{out}}$ is the outlet volatile mass fractions obtained from an homogeneous reactor using a reaction rate constant of k_0 as described above, and $\mathcal{Y}_{\text{out}}^*$ is the outlet volatile mass fraction of the riser observed in the simulation. The relevant parameters for calculating k_0^* are provided in Table 4.3. In each case, we find that $k_0^* < k_0$, demonstrating that the reduced mixing between the volatile and catalyst particles and backmixing of the gas due to clustering negatively impacts the catalytic conversion. This impact is quantified by a percentage reduction in reaction rate constant, $\mathcal{R}_{k_0} = (k_0 - k_0^*)/k_0^*$ shown in Table 4.3. For different simulation cases, the magnitude of $\mathcal{R}_{k_0}$ follows:

$$\mathcal{R}_{k_0,\mathcal{S}2} > \mathcal{R}_{k_0,\mathcal{S}1} > \mathcal{R}_{k_0,\mathcal{S}3}. \tag{4.22}$$

As shown in Table 4.3, $\mathcal{R}_{k_0}$ for $\mathcal{S}1$ and $\mathcal{S}2$ are close and much higher than $\mathcal{R}_{k_0}$ for

$\mathcal{S}3$. The trend of $\mathcal{R}_{k_0}$ can be explained by the following observations:

- The calculated values of bulk Da are provided in Table 4.4 and follow

$$\mathrm{Da}_{\mathcal{S}2} > \mathrm{Da}_{\mathcal{S}1} > \mathrm{Da}_{\mathcal{S}3}. \tag{4.23}$$

  We expect the negative impact of clustering through the reduction of mixing between volatiles and particles to follow the same trend as Da.

- The calculated values of Pe are provided in Table 4.4 and follow

$$\mathrm{Pe}_{\mathcal{S}3} \gg \mathrm{Pe}_{\mathcal{S}1} \sim \mathrm{Pe}_{\mathcal{S}2}. \tag{4.24}$$

  This trend of Pe shows that backmixing of gas is much more prominent in $\mathcal{S}1$ and $\mathcal{S}2$ compared to $\mathcal{S}3$. Therefore, reduction in the volatile conversion should be much higher in $\mathcal{S}1$ and $\mathcal{S}2$ compared to $\mathcal{S}3$.

- As pointed out earlier, the axial distribution of particles is much more uniform in $\mathcal{S}3$ compared to $\mathcal{S}1$ and $\mathcal{S}2$, providing a better contact efficiency between the volatile and particles and higher volatile conversion in $\mathcal{S}3$.

These observations imply that an increase in velocity leads to a more homogeneous distribution of particles along the riser height and reduces the backmixing of the gas, leading to an improved volatile conversion.

4.5 Reduced-order modeling

Due to the excessive computational expense and time associated with simulating three-dimensional fluidized bed reactors, reduced-order models, often

Table 4.3: Parameter to calculate the effective reaction rate constant.

	Units	$\mathcal{S}1$	$\mathcal{S}2$	$\mathcal{S}3$
$\mathcal{Y}_{\text{out}}$	-	0.050	0.005	0.158
$\mathcal{Y}^*_{\text{out}}$	-	0.131	0.054	0.185
k_0	s^{-1}	40	80	40
k_0^*	s^{-1}	23	39	35
$\mathcal{R}_{k_0}$	%	-43	-51	-13

Table 4.4: Da and Pe for different simulation cases.

	$\mathcal{S}1$	$\mathcal{S}2$	$\mathcal{S}3$
Da	2.4	4.8	1.2
Pe	1.7	1.8	9.2

called engineering models, remain a key design tool for predicting the performance of multiphase reactors in a computationally affordable manner. These models represent a simplified picture of the complex processes that happen in a multiphase reactor to reduce the computational expense. In literature, several papers [155, 122, 173, 194] employ various engineering models to study biomass thermochemical conversion in fluidized bed reactors. In general, these models divide the fluidized bed reactor into several parts, such as bubble or emulsion phases, and use empirical models to represent each part. Another commonly employed strategy is to use one-dimensional conservation equations neglecting the unclosed terms. It remains a challenge to rigorously derive reduced-order models based on first principles. In the following subsections, we first compare the results of the three-dimensional riser simulations with a representative

engineering model and show that the commonly used engineering models do not provide an adequate prediction of the three-dimensional simulation results. To remedy this, we rigorously derive a one-dimensional model by Reynolds-averaging the volume-filtered species conservation equation and validate it by comparing it with the predictions of our three-dimensional simulations.

4.5.1 Comparison with a representative engineering model

Engineering models typically employ a combination of plug flow reactors (PRFs) and/or continuously stirred reactors (CSTRs) to represent large-scale reactors at minimal cost. For example, Yan et al. [194] recently developed a one-dimensional model for biomass steam gasification in dual fluidized bed gasifiers using the commercial Aspen Plus software [146], where the riser was modeled as a series of CSTRs and the bubbling fluidized bed was modeled using a series of interacting PFRs and CSTRs. We want to assess the performance and predictive capabilities of such an engineering model for the riser considered in this work. We, therefore, model the riser as a series of n CSTRs, with n large enough to ensure smooth volatile mass fraction profiles. In the model, each CSTR is referred to as a stage in the riser. Following Yan et al. [194], neglecting axial and radial dispersion, the integral form of the molar balance equation for the riser model can be written as

$$M_{(i-1)} - A_{(i)}\varepsilon_{f,(i)} \int_{Z_{i-1}}^{Z_i} \Omega^j_{(i)} dZ - M_{(i)} = 0, \tag{4.25}$$

where the subscripts i and $i-1$ denote the outlet and inlet of stage i. $M_{(i)}$, $A_{(i)}$, and $\varepsilon_{f,(i)}$ denote the molar flow rate, the cross-sectional area, and the volume fraction of the gas phase in stage i, respectively. Z is the vertical coordinate and

n is set to 20 in this case. $\Omega^{j}_{(i)}$ represents the consumption rate of species j in stage i. In this work, we take advantage of the detailed simulations performed in the previous section and use the $\varepsilon_{f,(i)}$ obtained from the detailed simulations directly. $\varepsilon_{f,(i)}$ being fully specified, Eq. 4.25 can be readily solved. The resulting volatile mass fraction profiles are compared with the three-dimensional simulations in Fig. 4.5. The percentage error in the prediction of the three-dimensional riser outlet volatile mass fraction using the engineering model is $\mathcal{E}_{\mathrm{VOL}}$ = 53% for $\mathcal{S}1$, 83% for $\mathcal{S}2$, and 12% for $\mathcal{S}3$, even though the gas volume fraction is set to the correct value. In practice, however, this information is not available, and various empirical relations are typically used to evaluate $\varepsilon_{f,(i)}$ instead, whose lack of accuracy can further increase the deviation between the predictions of the riser simulations and the engineering model. The engineering model, therefore, appears not capable of satisfactorily predicting the three-dimensional simulation results, highlighting a need for more predictive, yet still computationally cheap models.

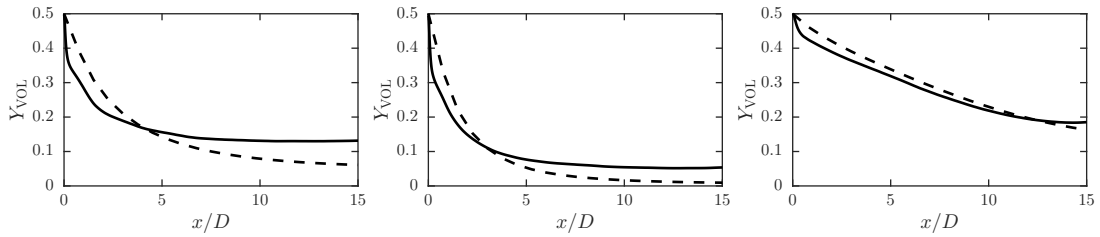

(a) Simulation $\mathcal{S}1$ (b) Simulation $\mathcal{S}2$ (c) Simulation $\mathcal{S}3$

Figure 4.5: Comparison of axial volatile mass fraction profiles obtained from the three-dimensional simulations (solid line) and the CSTR-based engineering model (dashed line) with $\varepsilon_{f,(i)}$ obtained from the three-dimensional simulations for the configurations in Table 2.

To move forward to improving on the CSTR-based engineering model, a one-dimensional model rigorously based on Reynolds-averaging the volume-

filtered species conservation equations is presented in the following sub-section along with the closures for the resulting unclosed terms.

4.5.2 Reduced-order model development

Reynolds-averaged scalar transport equation

In order to develop a computationally inexpensive model for the catalytic conversion process in a riser, we Reynolds-average Eq. 4.6 in the angular direction and take cross-sectional average in the radial direction, which leads to a one-dimensional species transport equation in the axial direction given by

$$\begin{aligned}\frac{\partial}{\partial t}\left(\langle\varepsilon_f\rho_f\rangle\widetilde{Y}_i\right)+\frac{\partial}{\partial x}\left(\langle\varepsilon_f\rho_f\rangle\widetilde{u}_f\widetilde{Y}_i\right)=\\ -\frac{\partial}{\partial x}\left(\langle\varepsilon_f\rho_f\rangle\widetilde{u_f'Y_i'}\right)+\frac{\partial}{\partial x}\left(\langle\varepsilon_f\rho_f\rangle D_i\widetilde{\frac{\partial Y_i}{\partial x}}\right)+\langle\dot{\omega}_i\rangle,\end{aligned} \tag{4.26}$$

with the chemical source term given by

$$\langle\dot{\omega}_i\rangle=\frac{\nu_i W_i k_0}{\varepsilon_{p,\max}W_{\mathrm{VOL}}}\langle\varepsilon_f\rho_f\rangle\left(\widetilde{\varepsilon}_p\widetilde{Y}_{\mathrm{VOL}}+\widetilde{\varepsilon_p'Y_{\mathrm{VOL}}'}\right). \tag{4.27}$$

In those equations, $\langle\cdot\rangle$ denotes a quantity averaged over the cross-sectional area and $\widetilde{(\cdot)}$ represents the density-weighted cross-sectional average known as Favre-average, i.e., $\widetilde{(\cdot)} = \langle(\cdot)\varepsilon_f\rho_f\rangle/\langle\varepsilon_f\rho_f\rangle$. $(\cdot)'$ denotes a fluctuation about a Favre-average quantity such that any variable can be decomposed into its density-weighted mean and fluctuation components, i.e., $(\cdot) = \widetilde{(\cdot)} + (\cdot)'$.

In Eq. 4.26, solving for $\widetilde{Y}_i$ requires closures for the unclosed terms, $\widetilde{u_f'Y_i'}$ and $\widetilde{\varepsilon_p'Y_{\mathrm{VOL}}'}$, on the right-hand side. The scalar flux term $\widetilde{u_f'Y_i'}$ arises from averaging the non-linear convective term in Eq. 4.6, and is expected to have a significant

contribution due to strong lateral agitation created by the multiphase dynamics. Because the flow is convectively dominated, fluctuations about the Favre-average diffusion term $\widetilde{D_i \frac{\partial Y_i}{\partial x}}$ are expected to be small, and are therefore dropped from Eq. 4.26. The catalyst-volatile covariance term $\varepsilon_p' \widetilde{Y_{\mathrm{VOL}}'}$ in Eq. 4.27 accounts for lateral segregation in particle concentration as a result of clustering. A discussion of both the unclosed terms is provided in the next sub-section.

Analysis of the unclosed terms

Profiles of the unclosed terms appearing in Eqs. 4.26 and 4.27, $\widetilde{u_f' Y_i'}$ and $\varepsilon_p' \widetilde{Y_{\mathrm{VOL}}'}$, are shown in Fig. 4.6. Top row of Fig. 4.6 shows that $u_f' \widetilde{Y_{\mathrm{VOL}}'}$ is positive for all simulation cases, implying that the vertical component of the fluid velocity is positively correlated to volatile mass fraction. This can be explained by the fact that near the reactor inlet, the flow resembles that of a bubbling fluidized bed reactor, with strong recirculation and high level of mixing. A downward flow in this region is indicative of increased interphase mixing and thus depletion of biomass volatile. Above the fluidized bed region, clusters fall at the walls and entrain the gas downward. Sustained contact between the phases within the clusters results in a low volatile mass fraction. The inverse is true for the products: gas and hydrocarbon. The covariances between the fluctuations of catalyst volume fraction and volatile mass fraction, $\varepsilon_p' \widetilde{Y_{\mathrm{VOL}}'}$, are found to be negative as shown in the bottom row of Fig. 4.6. It implies that an increase in local particle concentration corresponds to a depletion in the volatile mass fraction, with the greatest effect found near the reactor inlet. Near the exit, the volatile mass fraction and particle volume fraction are significantly lower, with their fluctuations nearly uncorrelated.

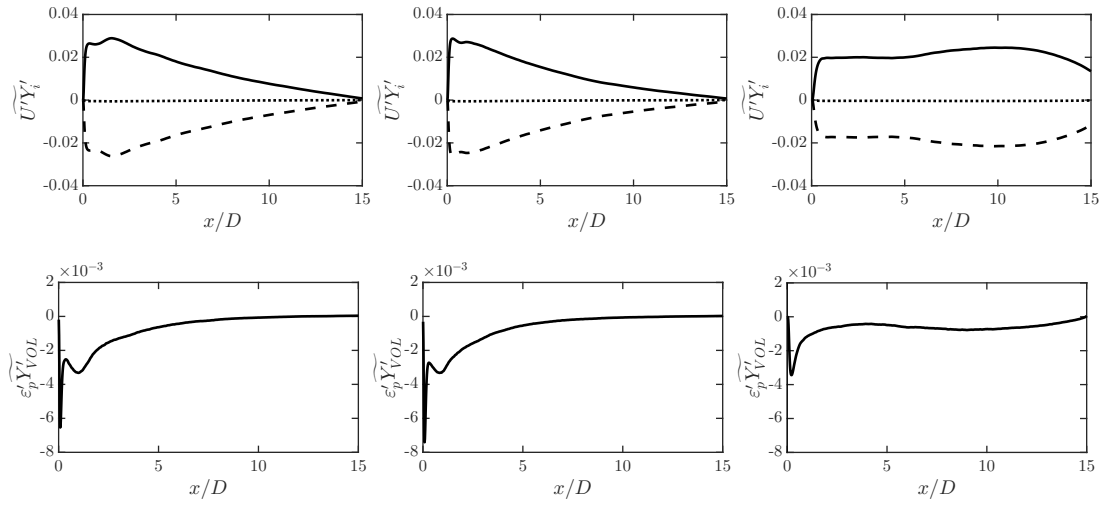

(a) Simulation $\mathcal{S}1$ (b) Simulation $\mathcal{S}2$ (c) Simulation $\mathcal{S}3$

Figure 4.6: Unclosed terms appearing in Eq. 4.26. Top row: $u'_f\widetilde{Y'_{\text{VOL}}}$ (solid line), $u'_f\widetilde{Y'_{\text{HC}}}$ (dashed line), and $u'_f\widetilde{Y'_{\text{GAS}}}$ (thin solid line). Bottom row: $\varepsilon'_p\widetilde{Y'_{\text{VOL}}}$.

To correctly capture the two-phase dynamic effects on the conversion rate, the unclosed flux terms in Eqs. 4.26 and 4.27 need to be closed, that is, we need to develop models for them. Classical gradient diffusion models can be employed to model the scalar flux term ($u'_f\widetilde{Y'_{\text{VOL}}}$). However, these models were designed for single-phase turbulence and are known to provide poor predictions in highly anisotropic flows [32]. We found that the mean scalar gradient is unable to reproduce the unclosed scalar flux profiles shown in Fig. 4.6, and thus more sophisticated models are needed. In Capecelatro et al. [27], an equation for $\varepsilon'_p\widetilde{Y'_{\text{VOL}}}$ was derived for a zero-dimensional system. However, it was ultimately found that obtaining closures for the unclosed terms that appear in this equation for $\varepsilon'_p\widetilde{Y'_{\text{VOL}}}$ is challenging.

The first step in deriving appropriate closures for $\widetilde{u'_f Y'_i}$ and $\varepsilon'_p\widetilde{Y'_{\text{VOL}}}$, is to quantify their role in the dynamics of the system. For this purpose, the volatile mass

fraction profiles obtained from the three-dimensional simulations $\mathcal{S}1$, $\mathcal{S}2$, and $\mathcal{S}3$, are compared with the profiles computed by solving Eq. 4.26 with

1. both unclosed terms neglected and $\widetilde{\varepsilon}_p$ taken to be constant (equal to $\overline{\varepsilon}_p$), and
2. both unclosed terms neglected and $\widetilde{\varepsilon}_p$ taken directly from the three-dimensional simulation.

The resulting volatile mass fraction profiles, displayed in Fig. 4.7, show that neglecting the unclosed terms ($\widetilde{u_f' Y_i'}$ and $\widetilde{\varepsilon_p' Y_{\mathrm{VOL}}'}$) results in an over-prediction of the conversion efficiency. The resulting errors in the prediction of the outlet volatile mass fractions for $\mathcal{S}1$, $\mathcal{S}2$, and $\mathcal{S}3$ are $\mathcal{E}_{\mathrm{VOL}}$ = 62%, 91%, and 15% for the constant $\widetilde{\varepsilon}_p$ case, and $\mathcal{E}_{\mathrm{VOL}}$ = 56%, 88%, and 9% for the case where $\widetilde{\varepsilon}_p$ is obtained from the three-dimensional simulations. This demonstrates that Eq. 4.26 without the unclosed terms can not accurately predict the three-dimensional simulation results, even with the knowledge of particle concentration profile. This observation implies that those engineering models that do not accurately include the impact of heterogeneities in the riser will perform poorly even with an accurate knowledge of axial profiles of particle concentration and fluid velocity.

Next step in analyzing the role of the unclosed terms in the riser dynamics is to compare the impact of the individual unclosed terms on the one-dimensional model. For that, we compute the volatile mass fraction profiles by solving Eq. 4.26 with:

1. $\widetilde{u_f' Y_{\mathrm{VOL}}'}$ obtained from the three-dimensional simulations while neglecting $\widetilde{\varepsilon_p' Y_{\mathrm{VOL}}'}$, and

2. $\varepsilon_p' \widetilde{Y_{\mathrm{VOL}}'}$ obtained from the three-dimensional simulations while neglecting $u_f' \widetilde{Y_{\mathrm{VOL}}'}$

and compare them with the profiles obtained from the three-dimensional simulations in Fig. 4.8. Incorporating the scalar flux $\widetilde{u_f' Y_i'}$ obtained from the three-dimensional simulation significantly improves the prediction of the one-dimensional equation, whereas including $\varepsilon_p' \widetilde{Y_{\mathrm{VOL}}'}$ has a negligible effect on the prediction of the volatile mass fraction. This implies that lateral inhomogeneities due to clustering are impacting the catalytic conversion of volatile primarily through $\widetilde{u_f' Y_i'}$, and thus an accurate prediction of only $\widetilde{u_f' Y_i'}$ is sufficient to correctly capture the catalytic conversion process. This is done in the following sub-section.

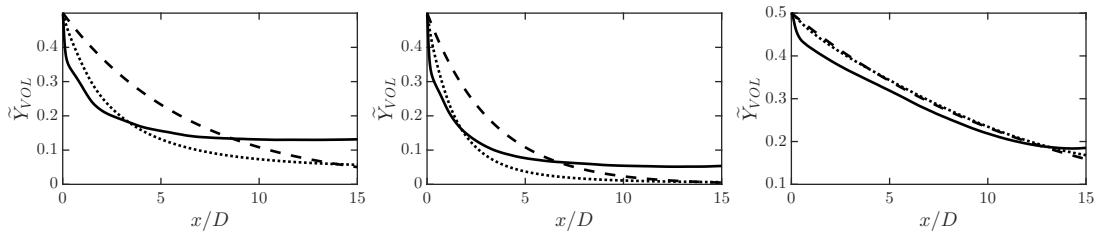

(a) Simulation $\mathcal{S}1$ (b) Simulation $\mathcal{S}2$ (c) Simulation $\mathcal{S}3$

Figure 4.7: Volatile mass fraction profiles computed from the one-dimensional transport equations using the unclosed terms and volume fraction profile obtained from the three-dimensional simulation (solid line), neglecting the residual fluxes with $\widetilde{\varepsilon}_p = \overline{\varepsilon}_p$ (dashed line), and neglecting the residual fluxes with $\widetilde{\varepsilon}_p$ taken from the three-dimensional simulation (dotted line).

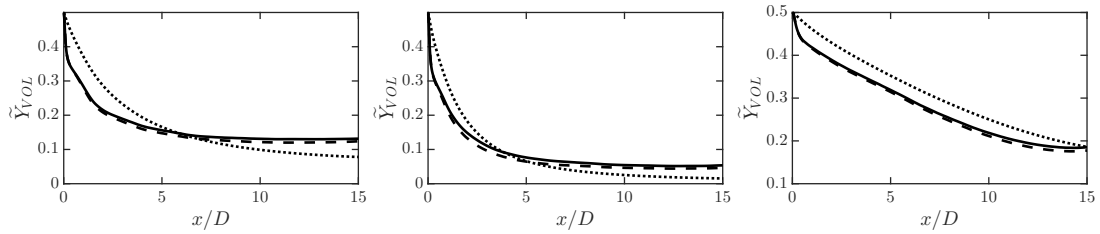

(a) Simulation $\mathcal{S}1$ (b) Simulation $\mathcal{S}2$ (c) Simulation $\mathcal{S}3$

Figure 4.8: Volatile mass fraction profiles obtained from the three-dimensional simulations (solid line) and computed by solving Eq. 4.26 by 1) neglecting $\varepsilon_p'\widetilde{Y_{\text{VOL}}'}$ while using $u_f'\widetilde{Y_{\text{VOL}}'}$ obtained from the three-dimensional simulations (dashed line) and 2) neglecting $u_f'\widetilde{Y_{\text{VOL}}'}$ while using $\varepsilon_p'\widetilde{Y_{\text{VOL}}'}$ obtained from the three-dimensional simulations (dotted line).

Closure for the scalar flux $u_f'\widetilde{Y_{\text{VOL}}'}$

We first quantify the strength of the correlation between u_f and Y_{VOL} by introducing the correlation coefficient $\rho_{X,Y}$ between two random variables X and Y:

$$\rho_{X,Y} = \frac{\widetilde{X'Y'}}{X_{\text{RMS}}Y_{\text{RMS}}}, \tag{4.28}$$

where $\widetilde{X'Y'}$ is the covariance of X and Y, and X_{RMS} and Y_{RMS} are the root-mean-square (RMS) of X' and Y', respectively. $\rho_{X,Y}$ being close to 1 implies that X and Y are strongly correlated and $\widetilde{X'Y'} \sim X_{\text{RMS}}Y_{\text{RMS}}$. Figure 4.9 shows that $\rho_{u_f,Y_{\text{VOL}}}$ is close to 0.8 up to the riser height of x/D=11 in the $\mathcal{S}1$ and $\mathcal{S}2$ cases, whereas in the $\mathcal{S}3$ case, it is close to 0.9 for the entire length of the riser. Using $\rho_{u_f,Y_{\text{VOL}}}$ equal to 1 in Eq. 4.28 for all simulation cases, we can model $u_f'\widetilde{Y_{\text{VOL}}'}$ as

$$\left[u_f'\widetilde{Y_{\text{VOL}}'}\right]_M = u_{f,\text{RMS}}Y_{\text{VOL,RMS}}, \tag{4.29}$$

where $\left[u_f'\widetilde{Y_{\text{VOL}}'}\right]_M$ is the modeled value for $u_f'\widetilde{Y_{\text{VOL}}'}$, and $u_{f,\text{RMS}}$ and $Y_{\text{VOL,RMS}}$ are the RMS values of u_f' and Y_{VOL}', respectively. Figures 4.10(a), 4.11(a), and 4.12(a) compare $\left[u_f'\widetilde{Y_{\text{VOL}}'}\right]_M$ with $u_f'\widetilde{Y_{\text{VOL}}'}$ obtained from each of the three-dimensional simulations $\mathcal{S}1$, $\mathcal{S}2$, and $\mathcal{S}3$, indeed showing good agreement between the two.

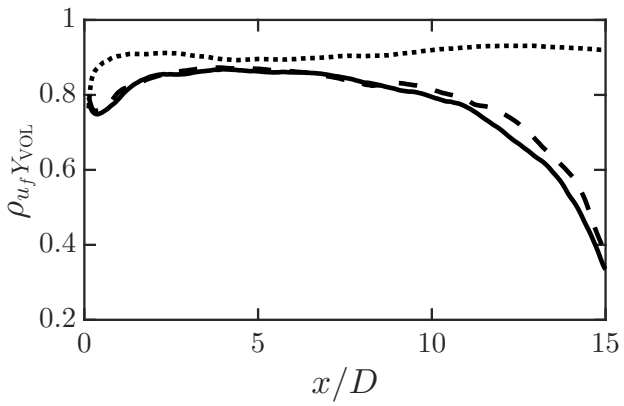

Figure 4.9: Correlation coefficient $\rho_{u_f,Y_{\mathrm{VOL}}}$ along the riser height for $\mathcal{S}1$ (solid line), $\mathcal{S}2$ (dashed line), and $\mathcal{S}3$ (dotted line).

To fully close this model, RMS variables now need to be defined in terms of the average variables $\widetilde{(\cdot)}$. $Y_{\mathrm{VOL,RMS}}$ is found to strongly follow the particle concentration profile, i.e., $Y_{\mathrm{VOL,RMS}} \approx \widetilde{\varepsilon}_p$, for $\mathcal{S}1$, $\mathcal{S}2$, and $\mathcal{S}3$, as shown in Figs. 4.10(b), 4.11(b), and 4.12(b). $u_{f,\mathrm{RMS}}$ strongly depends on the deviation of the axial fluid velocity across the riser cross-section from the mean axial fluid velocity, $\widetilde{u}_f$. Near the riser walls, gas gets trapped in the clusters and moves downward with falling clusters, significantly altering the gas velocity profile from the corresponding homogeneous case. It was found that $u_{f,\mathrm{RMS}}$ can be accurately computed if the cluster fall velocity, U_{cl}, is known. In the literature, models exist for U_{cl}, for example, that of Noymer and Glicksman [124]. Capecelatro et al. [26] performed simulations of a wall-bounded riser for a range of Archimedes numbers and showed that the cluster fall velocity follows the model developed by Noymer and Glicksman [124]. However, those simulations were periodic in the vertical direction and thus represented the fully developed region of a riser. In this work, the riser has strong heterogeneities in the vertical direction, thus the cluster fall velocity model of Noymer and Glicksman [124] can not be used here. In our knowledge, no analytical model exists that can accurately predict U_{cl} for

a strongly heterogenous riser. Therefore, we make the additional assumption that the magnitude of $u_{f,RMS}$ is proportional to $\widetilde{u}_f$. Comparisons of $u_{f,RMS}$ and $\widetilde{u}_f$ for $\mathcal{S}1$, $\mathcal{S}2$, and $\mathcal{S}3$ are shown in Figs. 4.10(c), 4.11(c), and 4.12(c). Replacing $u_{f,RMS}$ with $\widetilde{u}_f$ and $Y_{\mathrm{VOL,RMS}}$ with $\widetilde{\varepsilon}_p$ in Eq. 4.29, $u'_f\widetilde{Y'_{\mathrm{VOL}}}$ is modeled as

$$\left[u'_f\widetilde{Y'_{\mathrm{VOL}}}\right]_M \approx \widetilde{u}_f\widetilde{\varepsilon}_p. \tag{4.30}$$

Figures 4.10(d), 4.11(d), and 4.12(d) compare $u'_f\widetilde{Y'_{\mathrm{VOL}}}$ with $\widetilde{u}_f\widetilde{\varepsilon}_p$ for $\mathcal{S}1$, $\mathcal{S}2$, and $\mathcal{S}3$ and show a good agreement between the two quantities. We therefore use $\widetilde{u}_f\widetilde{\varepsilon}_p$ as the model for $u'_f\widetilde{Y'_{\mathrm{VOL}}}$ in Eq.(4.26) and compare the computed volatile mass fraction profiles with the profiles obtained from the three-dimensional simulations shown in Fig. 4.13. An error $\mathcal{E}_{\mathrm{VOL}}$ of 7%, 21%, and 9% is obtained for the outlet volatile mass fractions for $\mathcal{S}1$, $\mathcal{S}2$, and $\mathcal{S}3$, respectively. It shows significant improvement in the predictions for $\mathcal{S}1$ and $\mathcal{S}2$, and preserves good performance for $\mathcal{S}3$.

4.6 Conclusions

In this work, three-dimensional simulations were conducted to assess the influence of multiphase dynamics on biomass pyrolysis vapor catalytic upgrading in risers. The catalytic bio-vapor conversion is represented by a single step reaction in a volume-filtered Euler-Lagrange framework. The riser reactor was operated with inlet velocities much higher than minimum fluidization velocity. Three simulation cases were considered with different combinations of reaction rate constant and inlet velocity, resulting in different Damköhler numbers. In each case, catalytic particles were observed to form clusters near the walls, resulting in strong heterogeneity in species concentration. This non-

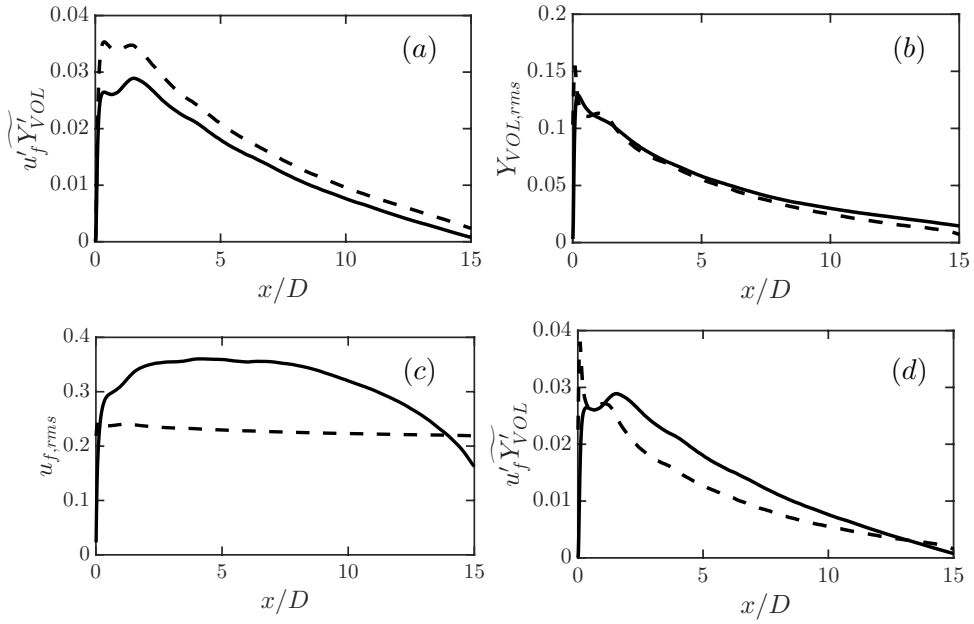

Figure 4.10: For simulation $\mathcal{S}1$, comparison of (a): $\widetilde{u'_f Y'_{\text{VOL}}}$ (solid line) and $u_{\text{f,RMS}} Y_{\text{VOL,RMS}}$ (dashed line), (b): $Y_{\text{VOL,RMS}}$ (solid line) and $\widetilde{\varepsilon}_p$ (dashed line), (c): $u_{\text{f,RMS}}$ (solid line) and $\widetilde{u}_f$ (dashed line), (d): $\widetilde{u'_f Y'_{\text{VOL}}}$ (solid line) and $\widetilde{u}_f \widetilde{\varepsilon}_p$ (dashed line).

homogeneity was found to reduce the catalytic conversion rate of biomass pyrolysis vapors to hydrocarbons by up to 50%. Here, large Damköhler numbers were considered, such that the catalytic conversion process is limited by the mass transport process. Higher inlet gas velocity improved the catalytic conversion efficiency by enhancing the transport rate and reducing the backmixing of the gas. An engineering model was employed representing the riser as a series of continuously stirred tank reactors (CSTRs), and it was unable to reproduce the trends observed in the three-dimensional simulation. Instead, a one-dimensional Reynolds-averaged transport equation was derived, and results were obtained by enforcing a uniform catalyst distribution (to model a homogeneous system) in addition to a mean catalyst distribution obtained from

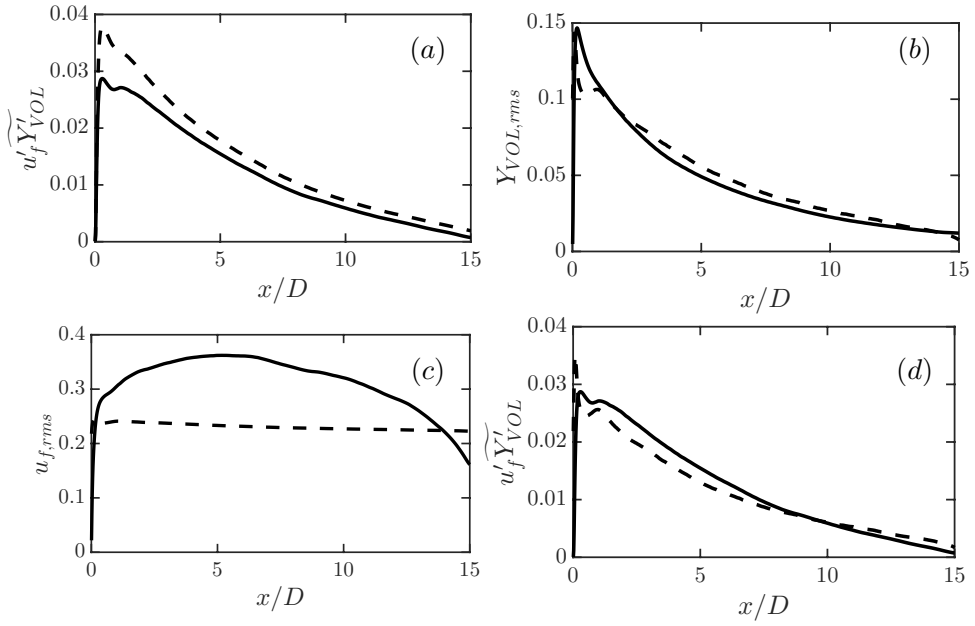

Figure 4.11: For simulation $\mathcal{S}2$, comparison of (a): $\widetilde{u'_f Y'_{\text{VOL}}}$ (solid line) and $u_{\text{f,RMS}} Y_{\text{VOL,RMS}}$ (dashed line), (b): $Y_{\text{VOL,RMS}}$ (solid line) and $\widetilde{\varepsilon}_p$ (dashed line), (c): $u_{\text{f,RMS}}$ (solid line) and $\widetilde{u}_f$ (dashed line), (d): $\widetilde{u'_f Y'_{\text{VOL}}}$ (solid line) and $\widetilde{u}_f \widetilde{\varepsilon}_p$ (dashed line).

the three-dimensional simulations. In both cases, the model predictions of reactor outlet volatile mass fraction resulted in more than 50% error for lower inlet velocity simulations. The non-homogeneity causing this discrepancy was found to be completely captured in the turbulent scalar flux. By including this term, the one-dimensional model was able to reproduce the trends observed in the three-dimensional simulation.

The current conversion model does not account for catalyst deactivation, although this phenomenon is known to be of great importance when operating catalytic reactors. Looking forward, it would be necessary to account for deactivation for catalytic particles that have been exposed to volatile for a sufficiently long period of time. Accounting for this effect is likely to further reduce the con-

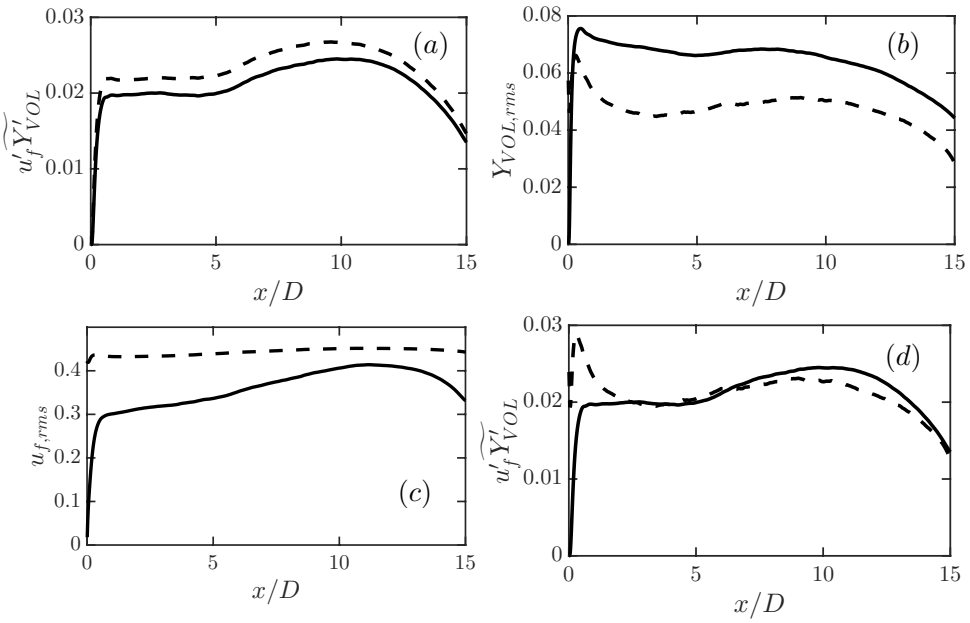

Figure 4.12: For simulation $\mathcal{S}3$, comparison of (a): $\widetilde{u'_f Y'_{\text{VOL}}}$ (solid line) and $u_{\text{f,RMS}} Y_{\text{VOL,RMS}}$ (dashed line), (b): $Y_{\text{VOL,RMS}}$ (solid line) and $\widetilde{\varepsilon}_p$ (dashed line), (c): $u_{\text{f,RMS}}$ (solid line) and $\widetilde{u}_f$ (dashed line), (d): $\widetilde{u'_f Y'_{\text{VOL}}}$ (solid line) and $\widetilde{u}_f \widetilde{\varepsilon}_p$ (dashed line).

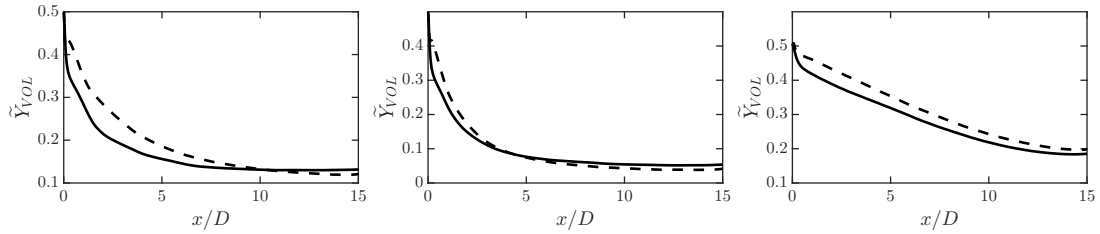

(a) Simulation $\mathcal{S}1$ (b) Simulation $\mathcal{S}2$ (c) Simulation $\mathcal{S}3$

Figure 4.13: Comparison of volatile mass fraction profiles obtained from the three-dimensional simulations (solid line) and using the one-dimensional transport equation with the modeled $\widetilde{u'_f Y'_{\text{VOL}}}$ (dotted line). (a) $\mathcal{S}1$, (b) $\mathcal{S}2$, and (c) $\mathcal{S}3$.

version efficiency of the reactor, and further amplify the role played by clusters.

CHAPTER 5

CONCLUSION AND PERSPECTIVES

This work advances the existing detailed modeling and simulation tools for biomass thermochemical conversion. The key contributions include the development of models for processes at different scales and exploring the coupling between them. A summary of the major results of this work is presented in the next subsection followed by a discussion of the future directions.

5.1 Summary of major results

In Chapter 2, a compact kinetic model (39 species, 5 quasi-steady state species, and a total of 118 reactions) is developed from a detailed kinetic model (396 species, 3210 reactions) using automated strategies for the gas-phase reactions of biomass gasification in the absence of oxygen. The reduced model shows very good reproducibility of the statistical yields of various species of interest at a fraction of computational cost compared to the detailed model. The computational affordability of the reduced model is demonstrated by using it with an in-house CFD code to simulate laboratory-scale Drop Tube Reactor (DTR) experiments of biomass fast pyrolysis and a pseudo two-dimensional FBR for biomass gasification. The reduced model developed in this work has the potential to replace the global kinetic models used in CFD simulations to study the impact of reactor operating conditions, such as temperature and inlet gas velocity, on the formation of different gaseous and tar species.

In Chapter 3, the uncertainty in the values of the thermal properties of biomass and char is propagated to the predictions of a one-dimensional particle-

scale biomass pyrolysis model. A comparison of the model predictions with the experiments showed that the uncertainty in the model predictions can account for most of the discrepancies related to the particle temperature profiles and the species production rates. However, the discrepancies related to the product yields and the timings of the peak production rates of a few species cannot be explained by the uncertainty. The results also showed that the pyrolysis model performs poorly in predicting all the targets related to CH_4. The experimental measurements identified in this work, whose predictions cannot be improved by an accurate knowledge of the transport model parameters, can be a focus area for further developments in the chemical kinetic model. Another part of this work focused on determining the optimal values of the uncertain model parameters by minimizing the L^2 error norm between the model predictions and experimental measurements. The optimization study demonstrated the importance of considering a wide variety of experimental targets during the model validation process, as good agreement can be obtained between the model predictions and the experiments by tuning the model parameters if only a few experimental measurements are considered.

In Chapter 4, three-dimensional CFD-DEM simulations of a CFB riser are performed to quantify the influence of multiphase dynamics on biomass pyrolysis vapor catalytic upgrading. Catalytic particles are observed to form clusters near the walls, resulting in strong heterogeneity in species concentration. This non-homogeneity is found to reduce the catalytic conversion rate of biomass pyrolysis vapors to hydrocarbons by up to 50%. Higher inlet gas velocity is observed to improve the catalytic conversion efficiency by enhancing the transport rate and reducing the backmixing of the gas. An engineering model, representing the riser as a series of continuously stirred tank reactors (CSTRs), is found

to be unable to reproduce the trends observed in the three-dimensional simulation. To reduce the computational cost associated with detailed CFD simulations, a reduced-order model is developed in the form of on a one-dimensional Reynolds-averaged transport equation. In this equation, the unclosed term representing the turbulent scalar flux is found to account for the reduction in the catalytic conversion of volatiles due to the formation of clusters. By developing a closure for this term, the one-dimensional model is shown to reproduce the trends observed in the three-dimensional simulation.

5.2 Future directions

In this work, several achievements were made in the development of modeling and simulations tools for biomass thermochemical conversion, though future work is required before these tools can be utilized to their full potential in the deployment of the conversion process. In this regard, four focus areas have been identified: 1) Models for particle-scale processes; 2) Coupling of models for various scales; 3) Model validation; 4) Development of reduced-order models, which are discussed below.

Models for particle-scale processes: One of the major challenges to further develop the computational tools for biomass thermochemical conversion is the accurate modeling of particle-scale processes, such as devolatilization of biomass particle, for industrially-relevant feedstock. Knowledge of these particle-scale processes is imperative to control the yield and composition of products, such as tar or syngas. In this work, a one-dimensional spherically symmetric model is developed for biomass pyrolysis and it needs to incorporate additional com-

plexities, such as arbitrary shape of particles, internal morphology, and intra-particle gas phase reactions. A detailed three-dimensional biomass pyrolysis model can provide an excellent platform to study biomass pyrolysis process in great detail and also help in the development of chemical kinetics [61].

Coupling of models for various scales: Simulations of the conversion reactors for biomass thermochemical require coupling of the adequate representation of chemical reactions and particle-scale processes with a CFD code. The associated computational cost for performing these simulations is prohibitive because of the large separation of length and time scales and therefore novel techniques are required to couple the models at different scales keeping the computational cost in check. For chemical kinetics, one such approach is to reduce a detailed kinetic model *a priori* to a compact kinetic model, which is used in this dissertation. However, several other approaches exist, such as tabulation techniques [147, 184, 169], which need to be explored in the context of biomass thermochemical conversion.

Model validation: Another area that requires significant improvement is the rigorous validation of the models developed for various processes. Collaboration between experimentalists and modelers to design controlled experiments that can be used for model validation can impel the modeling efforts in biomass thermochemical conversion. One important aspect related to the model validation is the quantitative inclusion of the uncertainty that exists in model parameters, modeling assumptions, etc. The work presented in Chapter 3 is the first to use uncertainty quantification (UQ) in the validation process of a particle-scale biomass pyrolysis model. In this work only uncertainty in the transport model parameters in a spherically symmetric configuration is considered. A variety

of different uncertainty sources still need to be explored for realistic biomass feedstock. A major difficulty in employing UQ in biomass conversion lies in the characterization of various sources of uncertainty and the propagation of uncertainty through the model in a computationally affordable manner.

Development of reduced-order models: The ultimate goal of modeling and simulation tools is to help in the optimal design and scale-up of the conversion reactors. As detailed simulations are too expensive to be performed for industrial-scale reactors, reduced-order models are required to predict their performance in a computationally affordable manner. The work presented in Chapter 4 is a step in this direction, and further progress can be made by performing detailed simulations of small configurations and using the knowledge gained from these simulations to build reduced-order models that can be used for larger systems or to verify and improve the existing engineering models.

BIBLIOGRAPHY

[1] J D Adjaye and N N Bakhshi. Catalytic conversion of a biomass-derived oil to fuels and chemicals 1: model compound studies and reaction pathways. *Biomass and Bioenergy*, 8(3):131–149, 1995.

[2] J D Adjaye and N N Bakhshi. Catalytic conversion of a biomass-derived oil to fuels and chemicals 2: Chemical kinetics, parameter estimation and model predictions. *Biomass and Bioenergy*, 8(4):265–277, 1995.

[3] Andrés Anca-Couce. Reaction mechanisms and multi-scale modelling of lignocellulosic biomass pyrolysis. *Progress in Energy and Combustion Science*, 53:41–79, 2016.

[4] Andrés Anca-Couce and Robert Scharler. Modelling heat of reaction in biomass pyrolysis with detailed reaction schemes. *Fuel*, 206:572–579, 2017.

[5] Andrés Anca-Couce, Peter Sommersacher, and Robert Scharler. Online experiments and modelling with a detailed reaction scheme of single particle biomass pyrolysis. *Journal of Analytical and Applied Pyrolysis*, 2017.

[6] T. B. Anderson and R. Jackson. Fluid mechanical description of fluidized beds. equations of motion. *Industrial & Engineering Chemistry Fundamentals*, 6(4):527–539, 1967.

[7] Renewable Fuels Association. Analysis of public and private data sources. http://www.ethanolrfa.org, 2017.

[8] BV Babu and AS Chaurasia. Pyrolysis of biomass: improved models for simultaneous kinetics and transport of heat, mass and momentum. *Energy conversion and Management*, 45(9-10):1297–1327, 2004.

[9] Akhilesh Bakshi. *Multiscale continuum simulations of fluidization: bubbles, mixing dynamics and reactor scaling*. PhD thesis, Massachusetts Institute of Technology, 2017.

[10] Hayat Bennadji, Krystle Smith, Michelle J Serapiglia, and Elizabeth M Fisher. Effect of particle size on low-temperature pyrolysis of woody biomass. *Energy & Fuels*, 28(12):7527–7537, 2014.

[11] Theodore L Bergman, Frank P Incropera, David P DeWitt, and Adrienne S Lavine. *Fundamentals of heat and mass transfer*. John Wiley & Sons, 2011.

[12] G Blanquart, P Pepiot-Desjardins, and H Pitsch. Chemical mechanism for high temperature combustion of engine relevant fuels with emphasis on soot precursors. *Combustion and Flame*, 156(3):588–607, 2009.

[13] Julien Blondeau and Hervé Jeanmart. Biomass pyrolysis at high temperatures: Prediction of gaseous species yields from an anisotropic particle. *Biomass and bioenergy*, 41:107–121, 2012.

[14] George EP Box. *Statistics for experiments: An introduction to design, data analysis, and model building*. John Wiley & Sons, 1978.

[15] Filipe L Brandão, Gabriel Lisbôa Verissimo, Marco Antonio Haikal Leite, Albino JK Leiroz, and Manuel E Cruz. Computational study of sugarcane bagasse pyrolysis modeling in a bubbling fluidized bed reactor. *Energy & Fuels*, 2018.

[16] AV Bridgwater. Review of fast pyrolysis of biomass and product upgrading. *Biomass and Bioenergy*, 38:68–94, 2012.

[17] AV Bridgwater, S Czernik, and J Piskorz. An overview of fast pyrolysis. *Progress in thermochemical biomass conversion*, pages 977–997, 2001.

[18] Anthony Brook, David Kendrick, and Alexander Meeraus. Gams, a user's guide. *ACM Signum Newsletter*, 23(3-4):10–11, 1988.

[19] J. Bruchmüller, K. H. Luo, and B. G. M. Van Wachem. Tar formation variations during fluidised bed pyrolytic biomass conversion. *Proceedings of the Combustion Institute*, 34(2):2373–2381, 2013.

[20] J Bruchmüller, BGM van Wachem, S Gu, KH Luo, and RC Brown. Modeling the thermochemical degradation of biomass inside a fast pyrolysis fluidized bed reactor. *AIChE Journal*, 58(10):3030–3042, 2012.

[21] Jorn Bruchmuller. *Modelling the degradation of particles in fluidised beds*. PhD thesis, University of Southampton, 2011.

[22] J Brunchmuller, BGM van Wachem, S Gu, KH Luo, and RC Brown. Modelling the thermochemical degradation of biomass inside a fast pyrolysis fluidised bed reactor. *AIChE Journal*, 58(10):3030–3042, 2012.

[23] Matteo Calonaci, Roberto Grana, Emma Barker Hemings, Giulia Bozzano, Mario Dente, and Eliseo Ranzi. Comprehensive kinetic modeling

study of bio-oil formation from fast pyrolysis of biomass. *Energy & Fuels*, 24(10):5727–5734, 2010.

[24] Charles S Campbell and Christopher E Brennen. Computer simulation of granular shear flows. *Journal of Fluid Mechanics*, 151:167–188, 1985.

[25] J. Capecelatro and O. Desjardins. An euler–lagrange strategy for simulating particle-laden flows. *Journal of Computational Physics*, 238:1–31, 2013.

[26] J. Capecelatro, P. Pepiot, and O. Desjardins. Numerical characterization and modeling of particle clustering in wall-bounded vertical risers. *Chemical Engineering Journal*, 245:295–310, 2014.

[27] J. Capecelatro, P. Pepiot, and O. Desjardins. Numerical investigation and modeling of reacting gas-solid flows in the presence of clusters. *Chemical Engineering Science*, 122:403–415, 2015.

[28] Li Chen. *Fast pyrolysis of millimetric wood particles between 800°C and 1000°C*. PhD thesis, Lyon I, 2009.

[29] Li Chen, Capucine Dupont, Sylvain Salvador, Maguelone Grateau, Guillaume Boissonnet, and Daniel Schweich. Experimental study on fast pyrolysis of free-falling millimetric biomass particles between 800 c and 1000 c. *Fuel*, 106:61–66, 2013.

[30] Helena Chum, APC Faaij, JR Moreira, HM Junginger, and MK Patel. *IPCC special report on renewable energy sources and climate change mitigation*. Cambridge University Press, 2011.

[31] Peter N Ciesielski, Michael F Crowley, Mark R Nimlos, Aric W Sanders, Gavin M Wiggins, Dave Robichaud, Bryon S Donohoe, and Thomas D Foust. Biomass particle models with realistic morphology and resolved microstructure for simulations of intraparticle transport phenomena. *Energy & Fuels*, 29(1):242–254, 2014.

[32] Daniel P Combest, Palghat A Ramachandran, and Milorad P Dudukovic. On the gradient diffusion hypothesis and passive scalar transport in turbulent flows. *Industrial & Engineering Chemistry Research*, 50(15):8817–8823, 2011.

[33] M. Corbetta, H. Frassoldati, A.and Bennadji, M. J. Smith, K.and Serapiglia, G. Gauthier, T. Melkior, E. Ranzi, and E. M. Fisher. Pyrolysis of centimeter-

scale woody biomass particles: kinetic modeling and experimental validation. *Energy & Fuels*, 28(6):3884–3898, 2014.

[34] Heping Cui and John R Grace. Fluidization of biomass particles: A review of experimental multiphase flow aspects. *Chemical Engineering Science*, 62(1):45–55, 2007.

[35] Peter A Cundall and Otto DL Strack. A discrete numerical model for granular assemblies. *Geotechnique*, 29(1):47–65, 1979.

[36] Lee J Curtis and Dennis J Miller. Transport model with radiative heat transfer for rapid cellulose pyrolysis. *Industrial & engineering chemistry research*, 27(10):1775–1783, 1988.

[37] Mark E Davis and Robert J Davis. *Fundamentals of chemical reaction engineering*. Courier Corporation, 2012.

[38] Paulo Eduardo Amaral Debiagi, Giancarlo Gentile, Matteo Pelucchi, Alessio Frassoldati, Alberto Cuoci, Tiziano Faravelli, and Eliseo Ranzi. Detailed kinetic mechanism of gas-phase reactions of volatiles released from biomass pyrolysis. *Biomass and Bioenergy*, 93:60–71, 2016.

[39] N. G. Deen, M. Van Sint Annaland, M. A. Van der Hoef, and J. A. M. Kuipers. Review of discrete particle modeling of fluidized beds. *Chemical Engineering Science*, 62(1):28–44, 2007.

[40] A. Demirbas. Progress and recent trends in biofuels. *Progress in energy and combustion science*, 33(1):1–18, 2007.

[41] O. Desjardins, G. Blanquart, G. Balarac, and H. Pitsch. High order conservative finite difference scheme for variable density low Mach number turbulent flows. *Journal of Computational Physics*, 227(15):7125–7159, 2008.

[42] O Desjardins, RO Fox, and P Villedieu. A quadrature-based moment method for dilute fluid-particle flows. *Journal of Computational Physics*, 227(4):2514–2539, 2008.

[43] O. Desjardins, V. Moureau, and H. Pitsch. An accurate conservative level set/ghost fluid method for simulating turbulent atomization. *Journal of Computational Physics*, 227(18):8395–8416, 2008.

[44] O Desjardins and H Pitsch. Modeling effect of spray evaporation on turbulent combustion. *Number paper ICLASS06-084, Kyoto, Japan*, 2006.

[45] O. Desjardins and H. Pitsch. A spectrally refined interface approach for simulating multiphase flows. *Journal of computational physics*, 228(5):1658–1677, 2009.

[46] Olivier Desjardins, Guillaume Blanquart, Guillaume Balarac, and Heinz Pitsch. High order conservative finite difference scheme for variable density low mach number turbulent flows. *Journal of Computational Physics*, 227(15):7125–7159, 2008.

[47] C. Di Blasi. Heat, momentum and mass transport through a shrinking biomass particle exposed to thermal radiation. *Chemical engineering science*, 51(7):1121–1132, 1996.

[48] C. Di Blasi. Modeling chemical and physical processes of wood and biomass pyrolysis. *Progress in Energy and Combustion Science*, 34(1):47–90, 2008.

[49] Colomba Di Blasi. Influences of physical properties on biomass devolatilization characteristics. *Fuel*, 76(10):957–964, 1997.

[50] J Eitelberger and K Hofstetter. Prediction of transport properties of wood below the fiber saturation point–a multiscale homogenization approach and its experimental validation: Part i: Thermal conductivity. *Composites science and technology*, 71(2):134–144, 2011.

[51] HF Feldmann, MA Paisley, HR Appelbaum, and DR Taylor. Conversion of forest residues to a methane-rich gas in a high-throughput gasifier. Technical report, Battelle Columbus Div., OH (USA), 1988.

[52] Giulia Fiorese, Michela Catenacci, Elena Verdolini, and Valentina Bosetti. Advanced biofuels: Future perspectives from an expert elicitation survey. *Energy Policy*, 56:293–311, 2013.

[53] DF Fletcher, BS Haynes, FC Christo, and SD Joseph. A cfd based combustion model of an entrained flow biomass gasifier. *Applied mathematical modelling*, 24(3):165–182, 2000.

[54] DF Fletcher, BS Haynes, FC Christo, and SD Joseph. A CFD based com-

bustion model of an entrained flow biomass gasifier. *Applied mathematical modelling*, 24(3):165–182, 2000.

[55] T.D. Foust, R. Wallace, R. Wooley, J. Sheehan, K. Ibsen, and D. Dayton. A national laboratory market and technology assessment of the 30x30 scenario. Technical Report TP-510-40942, NREL, 2007.

[56] Carlos Franco, Filomena Pinto, I Gulyurtlu, and I Cabrita. The study of reactions influencing the biomass steam gasification process? *Fuel*, 82(7):835–842, 2003.

[57] Bertil Fredlund. *A model for heat and mass transfer in timber structures during fire: a theoretical, numerical and experimental study*. PhD thesis, Lund University, Department of Fire Safety Engineering, 1988.

[58] Michael Frenklach. Systematic optimization of a detailed kinetic model using a methane ignition example. *Combustion and flame*, 58(1):69–72, 1984.

[59] Michael Frenklach, Hai Wang, and Martin J Rabinowitz. Optimization and analysis of large chemical kinetic mechanisms using the solution mapping method-combustion of methane. *Progress in Energy and Combustion Science*, 18(1):47–73, 1992.

[60] A Gel, R Garg, C Tong, M Shahnam, and C Guenther. Applying uncertainty quantification to multiphase flow computational fluid dynamics. *Powder technology*, 242:27–39, 2013.

[61] Giancarlo Gentile, Paulo Eduardo Amaral Debiagi, Alberto Cuoci, Alessio Frassoldati, Eliseo Ranzi, and Tiziano Faravelli. A computational framework for the pyrolysis of anisotropic biomass particles. *Chemical Engineering Journal*, 321:458–473, 2017.

[62] H Gerhauser, SC Generalis, RA Hague, and AV Bridgwater. CFD for the modelling of entrainment in fluidised bed fast pyrolysis of biomass. *Progress in Thermochemical Biomass Conversion*, pages 1281–1295, 2001.

[63] Massimo Germano, Ugo Piomelli, Parviz Moin, and William H Cabot. A dynamic subgrid-scale eddy viscosity model. *Physics of Fluids A: Fluid Dynamics (1989-1993)*, 3(7):1760–1765, 1991.

[64] LG Gibilaro, K Gallucci, R Di Felice, and P Pagliai. On the apparent viscosity of a fluidized bed. *Chemical engineering science*, 62(1):294–300, 2007.

[65] D. Gidaspow. *Multiphase flow and fluidization: continuum and kinetic theory descriptions*. Academic Pr, 1994.

[66] Samuel V Glass and Samuel L Zelinka. Moisture relations and physical properties of wood. *Wood handbook: wood as an engineering material: chapter 4. Centennial ed. General technical report FPL; GTR-190. Madison, WI: US Dept. of Agriculture, Forest Service, Forest Products Laboratory, 2010: p. 4.1-4.19.*, 190:4–1, 2010.

[67] Alberto Gómez-Barea and Bo Leckner. Modeling of biomass gasification in fluidized bed. *Progress in Energy and Combustion Science*, 36(4):444–509, 2010.

[68] Himanshu Goyal, Olivier Desjardins, Perrine Pepiot, and Jesse Capecelatro. A computational study of the effects of multiphase dynamics in catalytic upgrading of biomass pyrolysis vapor. *AIChE Journal*, 2018.

[69] Himanshu Goyal and Perrine Pepiot. Integrating intra-particle processes in large scale simulation of biomass thermochemical conversion. In *9th US Combustion Meeting, Cincinnati, Ohio*, 2015.

[70] Himanshu Goyal and Perrine Pepiot. A compact kinetic model for biomass pyrolysis at gasification conditions. *Energy & Fuels*, 31(11):12120–12132, 2017.

[71] MG. Gronli. *A theoretical and experimental study of the thermal degradation of biomass*. PhD thesis, The Norwegian University on Science and Technology, 1996.

[72] DJ Gunn. Transfer of heat or mass to particles in fixed and fluidised beds. *International Journal of Heat and Mass Transfer*, 21(4):467–476, 1978.

[73] Murlidhar Gupta, Jin Yang, and Christian Roy. Specific heat and thermal conductivity of softwood bark and softwood char particles. *Fuel*, 82(8):919–927, 2003.

[74] VILLE Hankalin, TUUKKA Ahonen, and RISTO Raiko. On thermal properties of a pyrolysing wood particle. *Finnish-Swedish Flame Days*, 16, 2009.

[75] Toshiro Harada, Toshimitsu Hata, and Shigehisa Ishihara. Thermal constants of wood during the heating process measured with the laser flash method. *Journal of Wood Science*, 44(6):425–431, 1998.

[76] Nils Erland L Haugen, Jonas Krüger, Dhrubaditya Mitra, and Terese Løvs. The effect of turbulence on mass transfer rates of small inertial particles with surface reactions. *Journal of Fluid Mechanics*, 836:932–951, 2018.

[77] Javier Herguido, Jose Corella, and Jose Gonzalez-Saiz. Steam gasification of lignocellulosic residues in a fluidized bed at a small pilot scale. effect of the type of feedstock. *Industrial & engineering chemistry research*, 31(5):1274–1282, 1992.

[78] Hermann Hofbauer and Reinhard Rauch. *Stoichiometric water consumption of steam gasification by the FICFB-gasification process*. na, 2000.

[79] COMSOL Inc. Comsol multiphysics, user's guide, version 4,, 2007.

[80] Liangyuan Jia, Yann Le-Brech, Binod Shrestha, Matthias Bente-von Frowein, Sven Ehlert, Guillain Mauviel, Ralf Zimmermann, and Anthony Dufour. Fast pyrolysis in a microfluidized bed reactor: effect of biomass properties and operating conditions on volatiles composition as analyzed by online single photoionization mass spectrometry. *Energy & Fuels*, 29(11):7364–7374, 2015.

[81] E Knudsen and H Pitsch. A dynamic model for the turbulent burning velocity for large eddy simulation of premixed combustion. *Combustion and Flame*, 154(4):740–760, 2008.

[82] E Knudsen and H Pitsch. A general flamelet transformation useful for distinguishing between premixed and non-premixed modes of combustion. *Combustion and flame*, 156(3):678–696, 2009.

[83] Peter Koch. Specific heat of ovendry spruce pine wood and bark. *Wood Science Vol. 1 (4): 203-214*, 1968.

[84] CA Koufopanos, G Maschio, and A Lucchesi. Pyrolysis kinetics of wood and wood components. *Can J Chem Eng*, 7:67–75, 1989.

[85] Jonas Krüger, Nils EL Haugen, Dhrubaditya Mitra, and Terese Løvs. The effect of turbulent clustering on particle reactivity. *Proceedings of the Combustion Institute*, 36(2):2333–2340, 2017.

[86] Xiaoke Ku, Tian Li, and Terese Løvs. Cfd–dem simulation of biomass gasification with steam in a fluidized bed reactor. *Chemical Engineering Science*, 122:270–283, 2015.

[87] Xiaoke Ku, Tian Li, and Terese Løvs. Effects of particle shrinkage and devolatilization models on high-temperature biomass pyrolysis and gasification. *Energy & Fuels*, 29(8):5127–5135, 2015.

[88] R Renu Kumar, Ajit Kumar Kolar, and Bo Leckner. Shrinkage characteristics of casuarina wood during devolatilization in a fluidized bed combustor. *Biomass and Bioenergy*, 30(2):153–165, 2006.

[89] Jenny Larfeldt, Bo Leckner, and Morten Chr Melaaen. Modelling and measurements of heat transfer in charcoal from pyrolysis of large wood particles. *Biomass and Bioenergy*, 18(6):507–514, 2000.

[90] D. Lathouwers and J. Bellan. Modeling of dense gas–solid reactive mixtures applied to biomass pyrolysis in a fluidized bed. *International Journal of Multiphase Flow*, 27(12):2155–2187, 2001.

[91] D Lathouwers and J Bellan. Yield optimization and scaling of fluidized beds for tar production from biomass. *Energy & Fuels*, 15(5):1247–1262, 2001.

[92] Calvin K Lee, Robert F Chaiken, and Joseph M Singer. Charring pyrolysis of wood in fires by laser simulation. In *Symposium (International) on Combustion*, volume 16, pages 1459–1470. Elsevier, 1977.

[93] Ji Eun Lee, Hoon Chae Park, and Hang Seok Choi. Numerical study on fast pyrolysis of lignocellulosic biomass with varying column size of bubbling fluidized bed. *ACS Sustainable Chemistry & Engineering*, 5(3):2196–2204, 2017.

[94] G Leon, J Cruz-de Leon, and L Villasenor. Thermal characterization of pine wood by photoacoustic and photothermal techniques. *Holz als Roh- und Werkstoff*, 58(4):241–246, 2000.

[95] Octave Levenspiel. Chemical reaction engineering. *Industrial & engineering chemistry research*, 38(11):4140–4143, 1999.

[96] Tingwen Li, Sreekanth Pannala, and Mehrdad Shahnam. CFD simulations of circulating fluidized bed risers, part ii, evaluation of differences between 2D and 3D simulations. *Powder Technology*, 254:115–124, 2014.

[97] XT Li, JR Grace, CJ Lim, AP Watkinson, HP Chen, and JR Kim.

Biomass gasification in a circulating fluidized bed. *Biomass and Bioenergy*, 26(2):171–193, 2004.

[98] Y. Liang, S. B. Pope, and P. Pepiot. An adaptive methodology for the efficient implementation of combustion chemistry in particle PDF methods. *Combust. Flame*, 162:3236–3253, 2015.

[99] Douglas K Lilly. A proposed modification of the germano subgrid-scale closure method. *Physics of Fluids A: Fluid Dynamics (1989-1993)*, 4(3):633–635, 1992.

[100] Chanchal Loha, Himadri Chattopadhyay, and Pradip K Chatterjee. Three dimensional kinetic modeling of fluidized bed biomass gasification. *Chemical Engineering Science*, 109:53–64, 2014.

[101] Terese Løvs, Ehsan Houshfar, Mette Bugge, and Øyvind Skreiberg. Automatic generation of kinetic skeletal mechanisms for biomass combustion. *Energy & fuels*, 27(11):6979–6991, 2013.

[102] Hong Lu, Elvin Ip, Justin Scott, Paul Foster, Mark Vickers, and Larry L Baxter. Effects of particle shape and size on devolatilization of biomass particle. *Fuel*, 89(5):1156–1168, 2010.

[103] K Maniatis, G Guiu, and J Riesgo. The european commission perspective in biomass and waste thermochemical conversion. *ChemInform*, 35(20), 2004.

[104] S Mathur, PK Tondon, and SC Saxena. Thermal conductivity of binary, ternary and quaternary mixtures of rare gases. *Molecular physics*, 12(6):569–579, 1967.

[105] Koichi Matsuoka, Koji Kuramoto, Takahiro Murakami, and Yoshizo Suzuki. Steam gasification of woody biomass in a circulating dual bubbling fluidized bed system. *Energy & Fuels*, 22(3):1980–1985, 2008.

[106] Maulik Mehta, Rodney O Fox, and Perrine Pepiot. Reduced chemical kinetics for the modeling of tio2 nanoparticle synthesis in flame reactors. *Industrial & Engineering Chemistry Research*, 54(20):5407–5415, 2015.

[107] Pelle Mellin, Efthymios Kantarelis, and Weihong Yang. Computational fluid dynamics modeling of biomass fast pyrolysis in a fluidized bed reactor, using a comprehensive chemistry scheme. *Fuel*, 117:704–715, 2014.

[108] Charles Meneveau, Thomas S Lund, and William H Cabot. A lagrangian dynamic subgrid-scale model of turbulence. *Journal of Fluid Mechanics*, 319:353–385, 1996.

[109] Matthew S Mettler, Dionisios G Vlachos, and Paul J Dauenhauer. Top ten fundamental challenges of biomass pyrolysis for biofuels. *Energy & Environmental Science*, 5(7):7797–7809, 2012.

[110] Marcel Meyer, A Devesa, S Hickel, XY Hu, and NA Adams. A conservative immersed interface method for large-eddy simulation of incompressible flows. *Journal of Computational Physics*, 229(18):6300–6317, 2010.

[111] RS Miller and J Bellan. A generalized biomass pyrolysis model based on superimposed cellulose, hemicelluloseand liqnin kinetics. *Combustion Science and Technology*, 126(1-6):97–137, 1997.

[112] Pet al Moin, K Squires, W Cabot, and Sangsan Lee. A dynamic subgrid-scale model for compressible turbulence and scalar transport. *Physics of Fluids A: Fluid Dynamics*, 3(11):2746–2757, 1991.

[113] P. M. Mortensen, J.D. Grunwaldt, P.A. Jensen, KG.. Knudsen, and A.D. Jensen. A review of catalytic upgrading of bio-oil to engine fuels. *Applied Catalysis A: General*, 407(1):1–19, 2011.

[114] Michael E Mueller and Heinz Pitsch. Large eddy simulation subfilter modeling of soot-turbulence interactions. *Physics of Fluids (1994-present)*, 23(11):115104, 2011.

[115] Habib N Najm. Uncertainty quantification and polynomial chaos techniques in computational fluid dynamics. *Annual review of fluid mechanics*, 41:35–52, 2009.

[116] K Narayanaswamy, G Blanquart, and H Pitsch. A consistent chemical mechanism for oxidation of substituted aromatic species. *Combustion and Flame*, 157(10):1879–1898, 2010.

[117] K. Narayanaswamy, H. Pitsch, and P. Pepiot. A component library framework for deriving kinetic mechanisms for multi-component fuel surrogates: Application for jet fuel surrogates. *Combust. Flame*, 165:288–309, 2016.

[118] Krithika Narayanaswamy, Perrine Pepiot, and Heinz Pitsch. Jet fuels and

fischer-tropsch fuels: surrogate definition and chemical kinetic modeling. In *US National Combustion Meeting*, 2013.

[119] Krithika Narayanaswamy, Perrine Pepiot, and Heinz Pitsch. A chemical mechanism for low to high temperature oxidation of n-dodecane as a component of transportation fuel surrogates. *Combustion and Flame*, 161(4):866–884, 2014.

[120] Krithika Narayanaswamy, Heinz Pitsch, and Perrine Pepiot. A chemical mechanism for low to high temperature oxidation of methylcyclohexane as a component of transportation fuel surrogates. *Combustion and Flame*, 162(4):1193–1213, 2015.

[121] Kyle E Niemeyer, Chih-Jen Sung, and Mandhapati P Raju. Skeletal mechanism generation for surrogate fuels using directed relation graph with error propagation and sensitivity analysis. *Combustion and flame*, 157(9):1760–1770, 2010.

[122] Mehrdokht B Nikoo and Nader Mahinpey. Simulation of biomass gasification in fluidized bed reactor using aspen plus. *Biomass and Bioenergy*, 32(12):1245–1254, 2008.

[123] Koyo Norinaga, Tetsuya Shoji, Shinji Kudo, and Jun-ichiro Hayashi. Detailed chemical kinetic modelling of vapour-phase cracking of multicomponent molecular mixtures derived from the fast pyrolysis of cellulose. *Fuel*, 103:141–150, 2013.

[124] Peter D Noymer and Leon R Glicksman. Descent velocities of particle clusters at the wall of a circulating fluidized bed. *Chemical Engineering Science*, 55(22):5283–5289, 2000.

[125] M. Oevermann, S. Gerber, and F. Behrendt. Euler–lagrange/dem simulation of wood gasification in a bubbling fluidized bed reactor. *Particuology*, 7(4):307–316, 2009.

[126] Michael Oevermann, Stephan Gerber, and Frank Behrendt. Euler–euler and euler–lagrange modeling of wood gasification in fluidized beds. In *Proceedings of the 9th International Conference on Circulating Fluidized Beds*, pages 733–738, 2008.

[127] Carolina Font Palma. Modelling of tar formation and evolution for biomass gasification: a review. *Applied energy*, 111:129–141, 2013.

[128] Sreekanth Pannala, Srdjan Simunovic, and George Frantziskonis. Multiscale/multiphysics modeling of biomass thermochemical processes. In *Computational Modeling in lignocellulosic biofuel production*, pages 245–271. ACS Publications, 2010.

[129] K Papadikis, S Gu, Anthony V Bridgwater, and H Gerhauser. Application of CFD to model fast pyrolysis of biomass. *Fuel Processing Technology*, 90(4):504–512, 2009.

[130] K Papadikis, S Gu, and AV Bridgwater. Cfd modelling of the fast pyrolysis of biomass in fluidised bed reactors. part b: heat, momentum and mass transport in bubbling fluidised beds. *Chemical Engineering Science*, 64(5):1036–1045, 2009.

[131] Konstantinos Papadikis, S Gu, and Anthony V Bridgwater. Cfd modelling of the fast pyrolysis of biomass in fluidised bed reactors: modelling the impact of biomass shrinkage. *Chemical Engineering Journal*, 149(1):417–427, 2009.

[132] Konstantinos Papadikis, S Gu, and Anthony V Bridgwater. CFD modelling of the fast pyrolysis of biomass in fluidised bed reactors: modelling the impact of biomass shrinkage. *Chemical Engineering Journal*, 149(1):417–427, 2009.

[133] W. C. Park, A. Atreya, and H. R. Baum. Experimental and theoretical investigation of heat and mass transfer processes during wood pyrolysis. *Combustion and Flame*, 157(3):481–494, 2010.

[134] M Brennan Pecha, Manuel Garcia-Perez, Thomas D Foust, and Peter N Ciesielski. Estimation of heat transfer coefficients for biomass particles by direct numerical simulation using microstructured particle models in the laminar regime. *ACS Sustainable Chemistry & Engineering*, 5(1):1046–1053, 2016.

[135] E. Peirano and B. Leckner. Fundamentals of turbulent gas-solid flows applied to circulating fluidized bed combustion. *Progress in Energy and Combustion Science*, 24(4):259–296, 1998.

[136] Jing Peng, Qitai Eri, and Xinjun Zhao. Detailed simulations of fast pyrolysis of biomass in a fluidized bed reactor. *Journal of Renewable and Sustainable Energy*, 10(1):013104, 2018.

[137] P. Pepiot. *Automatic strategies to model transportation fuel surrogates*. PhD thesis, Department of Mechanical Engineering, Stanford University, USA, 2008.

[138] P Pepiot, CJ Dibble, and TD Foust. Computational fluid dynamics modeling of biomass gasification and pyrolysis. In *Computational modeling in lignocellulosic biofuel production. ACS symposium series*, volume 1052, pages 273–98, 2010.

[139] P Pepiot, MW Jarvis, MR Nimlos, and G Blanquart. Chemical kinetic modeling of tar formation during biomass gasification. In *2010 Spring Meeting of the Western States Section of the Combustion Institute, Boulder, Colorado*, 2010.

[140] Perrine Pepiot-Desjardins and Heinz Pitsch. An automatic chemical lumping method for the reduction of large chemical kinetic mechanisms. *Combustion Theory and Modelling*, 12(6):1089–1108, 2008.

[141] Perrine Pepiot-Desjardins and Heinz Pitsch. An efficient error-propagation-based reduction method for large chemical kinetic mechanisms. *Combustion and Flame*, 154(1):67–81, 2008.

[142] Greg Perkins, Thallada Bhaskar, and Muxina Konarova. Process development status of fast pyrolysis technologies for the manufacture of renewable transport fuels from biomass. *Renewable and Sustainable Energy Reviews*, 90:292–315, 2018.

[143] Christoph Pfeifer and Hermann Hofbauer. Development of catalytic tar decomposition downstream from a dual fluidized bed biomass steam gasifier. *Powder Technology*, 180(1-2):9–16, 2008.

[144] C.D. Pierce. *Progress-variable approach for large-eddy simulation of turbulent combustion*. PhD thesis, Stanford University, 2001.

[145] Aspen Plus. Aspen plus user guide. *Aspen Technology Limited, Cambridge, Massachusetts, United States*, 2003.

[146] Aspen Plus. Aspen technology inc. *Cambridge, MA, USA*, 2006.

[147] Stephen B Pope. Computationally efficient implementation of combustion chemistry using in situ adaptive tabulation. *Combustion theory and modelling*, pages 41–63, 1997.

[148] DL Pyle and CA Zaror. Heat transfer and kinetics in the low temperature pyrolysis of solids. *Chemical engineering science*, 39(1):147–158, 1984.

[149] OS Rabinovich, VA Borodulya, LM Vinogradov, and VV Korban. Fast pyrolysis of an ensemble of biomass particles in a fluidized bed. *Journal of Engineering Physics and Thermophysics*, 83(4):742–752, 2010.

[150] KW Ragland, DJ Aerts, and AJ Baker. Properties of wood for combustion analysis. *Bioresource Technology*, 37(2):161–168, 1991.

[151] E. Ranzi, M. Corbetta, F. Manenti, and S. Pierucci. Kinetic modeling of the thermal degradation and combustion of biomass. *Chemical Engineering Science*, 110:2–12, 2014.

[152] Eliseo Ranzi, Alberto Cuoci, Tiziano Faravelli, Alessio Frassoldati, Gabriele Migliavacca, Sauro Pierucci, and Samuele Sommariva. Chemical kinetics of biomass pyrolysis. *Energy & Fuels*, 22(6):4292–4300, 2008.

[153] Eliseo Ranzi, Paulo Eduardo Amaral Debiagi, and Alessio Frassoldati. Mathematical modeling of fast biomass pyrolysis and bio-oil formation. note i: Kinetic mechanism of biomass pyrolysis. *ACS Sustainable Chemistry & Engineering*, 5(4):2867–2881, 2017.

[154] REN21. Renewables 2013 global status report. *Paris: REN21 Secretariat*, 2013.

[155] Samy S Sadaka, AE Ghaly, and MA Sabbah. Two phase biomass air-steam gasification model for fluidized bed reactors: Part imodel development. *Biomass and bioenergy*, 22(6):439–462, 2002.

[156] M Hossein Sahraei, Marc A Duchesne, Robin W Hughes, and Luis A Ricardez-Sandoval. Experimental assessment, model validation, and uncertainty quantification of a pilot-scale gasifier. *Industrial & Engineering Chemistry Research*, 55(25):6961–6970, 2016.

[157] David Sandalow. *Freedom from oil: how the next president can end the United States' oil addiction*. McGraw-Hill Professional, 2008.

[158] GD Scott and DM Kilgour. The density of random close packing of spheres. *Journal of Physics D: Applied Physics*, 2:863, 1969.

[159] Timothy D Searchinger, Steven P Hamburg, Jerry Melillo, William

Chameides, Petr Havlik, Daniel M Kammen, Gene E Likens, Ruben N Lubowski, Michael Obersteiner, Michael Oppenheimer, et al. Fixing a critical climate accounting error. *Science*, 326(5952):527–528, 2009.

[160] Frank Shaffer, Balaji Gopalan, Ronald W Breault, Ray Cocco, SB Karri, Roy Hays, and Ted Knowlton. High speed imaging of particle flow fields in CFB risers. *Powder Technology*, 2013.

[161] Fred Shafizadeh and Peter PS Chin. Thermal deterioration of wood. In *Wood Technology: Chemical Aspects*. ACS Publications, 1977.

[162] David A Sheen and Hai Wang. The method of uncertainty quantification and minimization using polynomial chaos expansions. *Combustion and Flame*, 158(12):2358–2374, 2011.

[163] Eun-Jae Shin, Mark R Nimlos, and Robert J Evans. Kinetic analysis of the gas-phase pyrolysis of carbohydrates. *Fuel*, 80(12):1697–1709, 2001.

[164] William Simpson and Anton TenWolde. Physical properties and moisture relations of wood. In *The Encyclopedia of Wood*. Skyhorse Publishing, 1999.

[165] Krystle Smith. *A numerical study of the slow pyrolysis of thermally thick wood spheres*. PhD thesis, Cornell University, 2013.

[166] Addison K Stark, Richard B Bates, Zhenlong Zhao, and Ahmed F Ghoniem. Prediction and validation of major gas and tar species from a reactor network model of air-blown fluidized bed biomass gasification. *Energy & Fuels*, 29(4):2437–2452, 2015.

[167] Daniel Richard Stull and Harold Prophet. *JANAF thermochemical tables*. National Bureau of Standards U.S., 1971.

[168] BM Suleiman, J Larfeldt, B Leckner, and M Gustavsson. Thermal conductivity and diffusivity of wood. *Wood science and Technology*, 33(6):465–473, 1999.

[169] Jonathan E Sutton, Juan M Lorenzi, Jaron T Krogel, Qingang Xiong, Sreekanth Pannala, Sebastian Matera, and Aditya Savara. Electrons to reactors multiscale modeling: Catalytic co oxidation over ruo2. *ACS Catalysis*, 8(6):5002–5016, 2018.

[170] Kazuhiko Tasaka, Takeshi Furusawa, and Atsushi Tsutsumi. Biomass

gasification in fluidized bed reactor with co catalyst. *Chemical Engineering Science*, 62(18-20):5558–5563, 2007.

[171] S Tenneti, R Garg, and S Subramaniam. Drag law for monodisperse gas–solid systems using particle-resolved direct numerical simulation of flow past fixed assemblies of spheres. *International journal of multiphase flow*, 37(9):1072–1092, 2011.

[172] Henrik Thunman and Bo Leckner. Thermal conductivity of wood models for different stages of combustion. *Biomass and Bioenergy*, 23(1):47–54, 2002.

[173] Anna Trendewicz, Robert Braun, Abhijit Dutta, and Jack Ziegler. One dimensional steady-state circulating fluidized-bed reactor model for biomass fast pyrolysis. *Fuel*, 133:253–262, 2014.

[174] Esa Vakkilainen, Katja Kuparinen, and Jussi Heinimö. Large industrial users of energy biomass. In *IEA Bioenergy Task*, volume 40, page 2013, 2013.

[175] M. A. Van der Hoef, M. van Sint Annaland, N. G. Deen, and J. A. M. Kuipers. Numerical simulation of dense gas-solid fluidized beds: A multiscale modeling strategy. *Annu. Rev. Fluid Mech.*, 40:47–70, 2008.

[176] SVB Van Paasen, JHA Kiel, and HJ Veringa. Tar formation in a fluidised bed gasifier. Technical report, ECN, 2004.

[177] B. P. Van Poppel, O. Desjardins, and J. W. Daily. A ghost fluid, level set methodology for simulating multiphase electrohydrodynamic flows with application to liquid fuel injection. *Journal of Computational Physics*, 229(20):7977–7996, 2010.

[178] R Vinu and Linda J Broadbelt. A mechanistic model of fast pyrolysis of glucose-based carbohydrates to predict bio-oil composition. *Energy & Environmental Science*, 5(12):9808–9826, 2012.

[179] Hai Wang and David A Sheen. Combustion kinetic model uncertainty quantification, propagation and minimization. *Progress in Energy and Combustion Science*, 47:1–31, 2015.

[180] Liangyu Wang and Heinz Pitsch. Prediction of pollutant emissions from

industrial furnaces using large eddy simulation. In *5th US Combustion Meeting, San Diego, CA*, 2007.

[181] Ligang Wei, Shaoping Xu, Jingang Liu, Chunlan Lu, Shuqin Liu, and Changhou Liu. A novel process of biomass gasification for hydrogen-rich gas with solid heat carrier: preliminary experimental results. *Energy & fuels*, 20(5):2266–2273, 2006.

[182] Gavin M Wiggins, Peter N Ciesielski, and C Stuart Daw. Low-order modeling of internal heat transfer in biomass particle pyrolysis. *Energy & Fuels*, 30(6):4960–4969, 2016.

[183] Mark M Wright and Robert C Brown. Comparative economics of biorefineries based on the biochemical and thermochemical platforms. *Biofuels, Bioproducts and Biorefining*, 1(1):49–56, 2007.

[184] Nan Xie, Francine Battaglia, and Rodney O Fox. Simulations of multiphase reactive flows in fluidized beds using in situ adaptive tabulation. *Combustion Theory and Modelling*, 8(2):195–209, 2004.

[185] Qingang Xiong, Soroush Aramideh, and Song-Charng Kong. Modeling effects of operating conditions on biomass fast pyrolysis in bubbling fluidized bed reactors. *Energy & Fuels*, 27(10):5948–5956, 2013.

[186] Qingang Xiong and Song-Charng Kong. Modeling effects of interphase transport coefficients on biomass pyrolysis in fluidized beds. *Powder Technology*, 262:96–105, 2014.

[187] Qingang Xiong and Song-Charng Kong. High-resolution particle-scale simulation of biomass pyrolysis. *ACS Sustainable Chemistry & Engineering*, 4(10):5456–5461, 2016.

[188] Qingang Xiong, Song-Charng Kong, and Alberto Passalacqua. Development of a generalized numerical framework for simulating biomass fast pyrolysis in fluidized-bed reactors. *Chemical Engineering Science*, 99:305–313, 2013.

[189] Qingang Xiong, Fei Xu, Yaoyu Pan, Yang Yang, Zhiming Gao, Shuli Shu, Kun Hong, Francois Bertrand, and Jamal Chaouki. Major trends and roadblocks in cfd-aided process intensification of biomass pyrolysis. *Chemical Engineering and Processing-Process Intensification*, 2018.

[190] Qingang Xiong, Yang Yang, Fei Xu, Yaoyu Pan, Jingchao Zhang, Kun Hong, Giulio Lorenzini, and Shurong Wang. Overview of computational fluid dynamics simulation of reactor-scale biomass pyrolysis. *ACS Sustainable Chemistry & Engineering*, 5(4):2783–2798, 2017.

[191] Q Xue, D Dalluge, TJ Heindel, RO Fox, and RC Brown. Experimental validation and cfd modeling study of biomass fast pyrolysis in fluidized-bed reactors. *Fuel*, 97:757–769, 2012.

[192] Q Xue and RO Fox. Reprint of: Multi-fluid CFD modeling of biomass gasification in polydisperse fluidized-bed gasifiers. *Powder Technology*, 265:23–34, 2014.

[193] Q. Xue, T. J. Heindel, and R. O. Fox. A cfd model for biomass fast pyrolysis in fluidized-bed reactors. *Chemical Engineering Science*, 66(11):2440–2452, 2011.

[194] Linbo Yan, C Jim Lim, Guangxi Yue, Boshu He, and John R Grace. One-dimensional modeling of a dual fluidized bed for biomass steam gasification. *Energy Conversion and Management*, 127:612–622, 2016.

[195] DZ Zhang and A. Prosperetti. Averaged equations for inviscid disperse two-phase flow. *Journal of Fluid Mechanics*, 267:185–220, 1994.

[196] Hanbin Zhong, Juntao Zhang, Yuqin Zhu, and Shengrong Liang. Multi-fluid modeling biomass fast pyrolysis in the fluidized-bed reactor including particle shrinkage effects. *Energy and Fuels*, 30(8):6440–6447, 2016.

[197] Xiaowei Zhou, Michael W Nolte, Heather B Mayes, Brent H Shanks, and Linda J Broadbelt. Experimental and mechanistic modeling of fast pyrolysis of neat glucose-based carbohydrates. 1. experiments and development of a detailed mechanistic model. *Industrial & Engineering Chemistry Research*, 53(34):13274–13289, 2014.

[198] RWR Zwart, A Van der Drift, A Bos, HJM Visser, MK Cieplik, and HWJ Könemann. Oil-based gas washing-flexible tar removal for high-efficient production of clean heat and power as well as sustainable fuels and chemicals. *Environmental Progress & Sustainable Energy*, 28(3):324–335, 2009.